



---

## Multifunctional Shear Pressed CNT Sheets for Strain Sensing and Composite Joint Toughening

Alexander Bogdanovich  
North Carolina State University at Raleigh

---

09/30/2015  
Final Report

DISTRIBUTION A: Distribution approved for public release.

Air Force Research Laboratory  
AF Office Of Scientific Research (AFOSR)/ RTB2  
Arlington, Virginia 22203  
Air Force Materiel Command

REPORT DOCUMENTATION PAGE					Form Approved OMB No. 0704-0188	
<p>The public reporting burden for this collection of information is estimated to average 1 hour per response, including the time for reviewing instructions, searching existing data sources, gathering and maintaining the data needed, and completing and reviewing the collection of information. Send comments regarding this burden estimate or any other aspect of this collection of information, including suggestions for reducing the burden, to the Department of Defense, Executive Service Directorate (0704-0188). Respondents should be aware that notwithstanding any other provision of law, no person shall be subject to any penalty for failing to comply with a collection of information if it does not display a currently valid OMB control number.</p> <p><b>PLEASE DO NOT RETURN YOUR FORM TO THE ABOVE ORGANIZATION.</b></p>						
1. REPORT DATE (DD-MM-YYYY) 25-09-2015		2. REPORT TYPE Final			3. DATES COVERED (From - To) 04/01/2012-06/30/2015	
4. TITLE AND SUBTITLE Multifunctional Shear Pressed CNT Sheets for Strain Sensing and Composite Joint Toughening				5a. CONTRACT NUMBER FA9550-12-1-0170		
				5b. GRANT NUMBER		
				5c. PROGRAM ELEMENT NUMBER		
6. AUTHOR(S) Bogdanovich, Alexander E. Bradford Philip D. Stahl, James J. Li, Ang				5d. PROJECT NUMBER		
				5e. TASK NUMBER		
				5f. WORK UNIT NUMBER		
7. PERFORMING ORGANIZATION NAME(S) AND ADDRESS(ES) North Carolina State University, College of Textiles, Department of Textile Engineering, Chemistry and Science 2401 Research Dr., Raleigh, NC 27695-8301					8. PERFORMING ORGANIZATION REPORT NUMBER	
9. SPONSORING/MONITORING AGENCY NAME(S) AND ADDRESS(ES) AFOSR 875 N. Randolph Street Arlington, VA 22203					10. SPONSOR/MONITOR'S ACRONYM(S)	
					11. SPONSOR/MONITOR'S REPORT NUMBER(S)	
12. DISTRIBUTION/AVAILABILITY STATEMENT Unlimited						
13. SUPPLEMENTARY NOTES None						
14. ABSTRACT This research program investigated critical fabrication aspects, mechanical and electrical properties, and potential applications of a novel carbon nanotube material, named shear-pressed sheet. This material is fabricated from the chemical vapor deposition grown, tall aligned carbon nanotube arrays, with the use of automated shear-pressing device. It was shown that such sheets, having typically 50-200 micron thickness, are self-sustained and sufficiently stiff to be removed from the substrate, handled without its shape distortion and then used either in a dry form or as a resin-infused prepreg for interleaving laminated composites and their bonded joints. Extensive set of double-cantilever beam tests of composite laminates with integrated shear-pressed sheets showed substantial, up to two times, improvement in the Mode I interlaminar fracture toughness. Experimental single-lap and double-lap joints of composites with integrated shear-pressed sheet interleaves were manufactured and experimentally evaluated. Embedded carbon nanotube shear-pressed sheets and drawn sheets showed excellent electrical resistance sensitivity and thus a potential for being used as in-situ strain monitoring devices which are practically non-intrusive and may simultaneously provide fracture toughness enhancement.						
15. SUBJECT TERMS Carbon Nanotubes, Composite Laminates, Composite Joints, Strain Sensors, Fracture Toughness, Strain Monitoring						
16. SECURITY CLASSIFICATION OF:			17. LIMITATION OF ABSTRACT	18. NUMBER OF PAGES	19a. NAME OF RESPONSIBLE PERSON	
a. REPORT	b. ABSTRACT	c. THIS PAGE			Alexander Bogdanovich	
U	U	U	UU	83	19b. TELEPHONE NUMBER (Include area code) 919-515-6566	

## INSTRUCTIONS FOR COMPLETING SF 298

**1. REPORT DATE.** Full publication date, including day, month, if available. Must cite at least the year and be Year 2000 compliant, e.g. 30-06-1998; xx-06-1998; xx-xx-1998.

**2. REPORT TYPE.** State the type of report, such as final, technical, interim, memorandum, master's thesis, progress, quarterly, research, special, group study, etc.

**3. DATES COVERED.** Indicate the time during which the work was performed and the report was written, e.g., Jun 1997 - Jun 1998; 1-10 Jun 1996; May - Nov 1998; Nov 1998.

**4. TITLE.** Enter title and subtitle with volume number and part number, if applicable. On classified documents, enter the title classification in parentheses.

**5a. CONTRACT NUMBER.** Enter all contract numbers as they appear in the report, e.g. F33615-86-C-5169.

**5b. GRANT NUMBER.** Enter all grant numbers as they appear in the report, e.g. AFOSR-82-1234.

**5c. PROGRAM ELEMENT NUMBER.** Enter all program element numbers as they appear in the report, e.g. 61101A.

**5d. PROJECT NUMBER.** Enter all project numbers as they appear in the report, e.g. 1F665702D1257; ILIR.

**5e. TASK NUMBER.** Enter all task numbers as they appear in the report, e.g. 05; RF0330201; T4112.

**5f. WORK UNIT NUMBER.** Enter all work unit numbers as they appear in the report, e.g. 001; AFAPL30480105.

**6. AUTHOR(S).** Enter name(s) of person(s) responsible for writing the report, performing the research, or credited with the content of the report. The form of entry is the last name, first name, middle initial, and additional qualifiers separated by commas, e.g. Smith, Richard, J, Jr.

**7. PERFORMING ORGANIZATION NAME(S) AND ADDRESS(ES).** Self-explanatory.

**8. PERFORMING ORGANIZATION REPORT NUMBER.** Enter all unique alphanumeric report numbers assigned by the performing organization, e.g. BRL-1234; AFWL-TR-85-4017-Vol-21-PT-2.

**9. SPONSORING/MONITORING AGENCY NAME(S) AND ADDRESS(ES).** Enter the name and address of the organization(s) financially responsible for and monitoring the work.

**10. SPONSOR/MONITOR'S ACRONYM(S).** Enter, if available, e.g. BRL, ARDEC, NADC.

**11. SPONSOR/MONITOR'S REPORT NUMBER(S).** Enter report number as assigned by the sponsoring/monitoring agency, if available, e.g. BRL-TR-829; -215.

**12. DISTRIBUTION/AVAILABILITY STATEMENT.** Use agency-mandated availability statements to indicate the public availability or distribution limitations of the report. If additional limitations/ restrictions or special markings are indicated, follow agency authorization procedures, e.g. RD/FRD, PROPIN, ITAR, etc. Include copyright information.

**13. SUPPLEMENTARY NOTES.** Enter information not included elsewhere such as: prepared in cooperation with; translation of; report supersedes; old edition number, etc.

**14. ABSTRACT.** A brief (approximately 200 words) factual summary of the most significant information.

**15. SUBJECT TERMS.** Key words or phrases identifying major concepts in the report.

**16. SECURITY CLASSIFICATION.** Enter security classification in accordance with security classification regulations, e.g. U, C, S, etc. If this form contains classified information, stamp classification level on the top and bottom of this page.

**17. LIMITATION OF ABSTRACT.** This block must be completed to assign a distribution limitation to the abstract. Enter UU (Unclassified Unlimited) or SAR (Same as Report). An entry in this block is necessary if the abstract is to be limited.

**NORTH CAROLINA STATE UNIVERSITY  
COLLEGE OF TEXTILES  
DEPARTMENT OF TEXTILE ENGINEERING, CHEMISTRY AND SCIENCE**

**FINAL PERFORMANCE REPORT**

**Reporting Period: 4/01/2012-6/30/2015**

**“Multifunctional Shear Pressed CNT Sheets for Strain Sensing and  
Composite Joint Toughening”**

**PI: Dr. Alexander Bogdanovich**

Phone: 919-515-6566, Fax: 919-515-6532, E-mail: aebogdan@ncsu.edu

**Co-Pi: Dr. Philip Bradford**

Phone: 919-515-1866, Fax: 919-515-6532, E-mail: philip\_bradford@ncsu.edu

NC State University, College of Textiles, Dept. of Textile Engineering, Chemistry and Science  
2401 Research Drive, Raleigh, NC 27695-8301

**AFOSR GRANT # FA9550-12-1-0170**

**Program Manager: Dr. Byung-Lip Lee**

SEPTEMBER 2015

REPORT DOCUMENTATION PAGE				Form Approved OMB No. 0704-0188	
<p>The public reporting burden for this collection of information is estimated to average 1 hour per response, including the time for reviewing instructions, searching existing data sources, gathering and maintaining the data needed, and completing and reviewing the collection of information. Send comments regarding this burden estimate or any other aspect of this collection of information, including suggestions for reducing the burden, to the Department of Defense, Executive Service Directorate (0704-0188). Respondents should be aware that notwithstanding any other provision of law, no person shall be subject to any penalty for failing to comply with a collection of information if it does not display a currently valid OMB control number.</p> <p><b>PLEASE DO NOT RETURN YOUR FORM TO THE ABOVE ORGANIZATION.</b></p>					
1. REPORT DATE (DD-MM-YYYY) 25-09-2015		2. REPORT TYPE Final		3. DATES COVERED (From - To) 04/01/2012-06/30/2015	
4. TITLE AND SUBTITLE Multifunctional Shear Pressed CNT Sheets for Strain Sensing and Composite Joint Toughening			5a. CONTRACT NUMBER FA9550-12-1-0170		
			5b. GRANT NUMBER		
			5c. PROGRAM ELEMENT NUMBER		
6. AUTHOR(S) Bogdanovich, Alexander E. Bradford Philip D. Stahl, James J. Li, Ang			5d. PROJECT NUMBER		
			5e. TASK NUMBER		
			5f. WORK UNIT NUMBER		
7. PERFORMING ORGANIZATION NAME(S) AND ADDRESS(ES) North Carolina State University, College of Textiles, Department of Textile Engineering, Chemistry and Science 2401 Research Dr., Raleigh, NC 27695-8301			8. PERFORMING ORGANIZATION REPORT NUMBER		
9. SPONSORING/MONITORING AGENCY NAME(S) AND ADDRESS(ES) AFOSR 875 N. Randolph Street Arlington, VA 22203			10. SPONSOR/MONITOR'S ACRONYM(S)		
			11. SPONSOR/MONITOR'S REPORT NUMBER(S)		
12. DISTRIBUTION/AVAILABILITY STATEMENT Unlimited					
13. SUPPLEMENTARY NOTES None					
14. ABSTRACT This research program investigated critical fabrication aspects, mechanical and electrical properties, and potential applications of a novel carbon nanotube material, named shear-pressed sheet. This material is fabricated from the chemical vapor deposition grown, tall aligned carbon nanotube arrays, with the use of automated shear-pressing device. It was shown that such sheets, having typically 50-200 micron thickness, are self-sustained and sufficiently stiff to be removed from the substrate, handled without its shape distortion and then used either in a dry form or as a resin-infused prepreg for interleaving laminated composites and their bonded joints. Extensive set of double-cantilever beam tests of composite laminates with integrated shear-pressed sheets showed substantial, up to two times, improvement in the Mode I interlaminar fracture toughness. Experimental single-lap and double-lap joints of composites with integrated shear-pressed sheet interleaves were manufactured and experimentally evaluated. Embedded carbon nanotube shear-pressed sheets and drawn sheets showed excellent electrical resistance sensitivity and thus a potential for being used as in-situ strain monitoring devices which are practically non-intrusive and may simultaneously provide fracture toughness enhancement.					
15. SUBJECT TERMS Carbon Nanotubes, Composite Laminates, Composite Joints, Strain Sensors, Fracture Toughness, Strain Monitoring					
16. SECURITY CLASSIFICATION OF:			17. LIMITATION OF ABSTRACT  UU	18. NUMBER OF PAGES  83	19a. NAME OF RESPONSIBLE PERSON Alexander Bogdanovich
a. REPORT U	b. ABSTRACT U	c. THIS PAGE U			19b. TELEPHONE NUMBER (Include area code) 919-515-6566

Reset

Standard Form 298 (Rev. 8/98)  
Prescribed by ANSI Std. Z39.18  
Adobe Professional 7.0

## GOALS AND OBJECTIVES

The main goal of this work is to obtain scientific understanding of the possibilities provided by, and the behavioral features of, a novel type high performance carbon nanotube (CNT) reinforced composite material incorporated in the interfaces of composite laminates and bonded joints with the following two purposes: (a) providing enhancement of the interlaminar fracture toughness and strength and (b) serving as a continuous strain monitoring sensor. The material being in the focus of this investigation is a relatively thin (in the range of several hundred microns), high CNT volume fraction, shear-pressed sheet (SPS) fabricated from the vertically grown aligned CNT array (a.k.a. “CNT forest”). The intrinsic high fracture toughness of composites reinforced with such CNT SPS should provide significant increase in the interlaminar fracture toughness of composite laminates and bonded joints. Simultaneously, the piezoresistive nature of the aligned CNTs and their interconnected networks opens new opportunities for monitoring both the strain and progressive failure in the composite joints. The stated principal outcome of this research was to establish a starting point for the future development of field deployable multifunctional CNT SPS interface-enhancing materials enabling, at the same time, for strain sensing of composite laminates and bonded joints of aerospace structures. To achieve this, the following principal technical objectives have been stated for the project:

**1. Shear pressing of large-area CNT arrays for joint interleave reinforcement** – CNT arrays will be grown with dimensions much larger than previously obtained in the Co-PI's lab. Vertical arrays of CNTs with dimensions of approximately 100x50x2 mm will be grown using low pressure chemical vapor deposition (CVD) method.

**2. Integration of the CNT SPS interleaves into composite laminates and bonded joints** – The CNT sheets will be used in co-cured composite joints and secondary bonded joints. Resin/adhesive selection will be optimized to maximize the reinforced adhesive interleaf performance.

**3. CNT sheet strain sensing in composite joints** – The CNT sheet joint interleaves will be integrated in the joint structure and interfaced with electronic equipment to measure the electrical properties changes during mechanical testing. The detected change of electrical properties will be collected for the dominant in-plane strain. Attempt will be made to diagnose progressive failure of the joint using same kind integrated sensors.

**4. Quantification of composite laminate and bonded joint toughness enhancement** – Selected mechanical tests will be performed in order to determine the change in the interlaminar fracture toughness of composite laminates and ultimate failure loads of composite bonded joints enhanced with CNT SPS vs. the benchmark values. Particularly, double cantilever beam (DCB) tests will be used to determine the effect on mode I fracture toughness, and in-plane tensile tests will be used to determine the effect on ultimate strength of composite bonded joints.

**5. 3-D stress-strain, progressive failure and crack propagation analysis** – A full 3-D analysis using 3D Mosaic analysis approach and computer code will be conducted to predict the stress/strain fields and progressive failure developing in the laminates and joints with integrated CNT SPS interleaves under loading. Specifically, the DCB test will be simulated by the 3-D computational model.

**6. Investigating CNT SPS sensor data acquisition possibilities** - The possibility of developing different connection techniques and data acquisition methods from CNT SPS sensors integrated within composite laminates and bonded joints will be explored.

## SUMMARY OF ACCOMPLISHMENTS

This report summarizes our efforts to elucidate some principal effects of a novel CNT-reinforced interleaf concept. The interleaf material is fabricated from CVD vertically grown CNT arrays by the shear pressing method. The shear pressing is realized here on a specialty automated device which allows one to delicately control the CNT array alignment, CNT volume fraction and the shear pressed sheet (SPS) thickness. The produced thin dry SPS can be strategically placed within some region between composite plies and, after conventional laminate fabrication it becomes its integral part. Under this scenario, the SPS can be partly or fully impregnated during the cure process with the resin which is already contained in the prepreg plies. An alternative manufacturing approach could be to first impregnate the SPS preform with some other, desirably lower viscosity, resin and partially cure it, then embed the “SPS prepreg” between the plies of composite and complete the manufacturing cycle.

Extensive experimental results presented in this report show how the Double Cantilever Beam (DCB) testing methodology can be used to evaluate the effect of different CNT SPS interleaves on Mode I interlaminar fracture toughness of conventional carbon/epoxy laminated composites. The experimental studies reported here also included traditional optical microscopy and SEM imaging of the fractured DCB samples. They showed that the delamination propagation path is dramatically altered in the presence of CNT SPS interleaves. It changes from a nearly straight one to a highly tortuous; the latter one typically consists of a sequence of jagged or saw-tooth type microcracks often combined with even more subtle sub-micro scale cracks developing within the interleaf, and with microcracks propagating between the interleaf and adjacent composite ply. The overall delamination fracture mechanism shows highly variable from sample to sample and very sensitive to such factors as CNT functionalization, epoxy resin viscosity, cure cycle, the resin infusion technique into the SPS, to the presence of residual voids, and other fine manufacturing peculiarities.

Overall, results of this research in the part of enhancing fracture toughness of traditional laminates by embedding CNT SPS interleaves are very encouraging. They showed that both dry and pre-infused CNT SPS interleaves significantly, up to two times, increase the critical strain energy release rate of the baseline non-interleaved laminate. The non-functionalized, plasma treated and acid treated SPSs were used. Both functionalization methods maintained the high alignment and aspect ratio of the CNTs. Although adding the CNT functionalization step does not result in further significant toughening versus the non-functionalized interleave case, the characteristics of the fracture surfaces appear to be dramatically different. As evidenced by the much “smoother” load vs. displacement curves, the pre-infused SPS interleaves show better ability than the non-interleaved and dry SPS interleaved laminates to resist catastrophic failure. It is possible that this will also manifest in improved fatigue resistance, which may be another important subject of future studies. Apart from the Mode I fracture toughness performance (which was in the focus of this study), the CNT SPS reinforcements provide high dimensional stability to the interleaves and structural joining elements. This feature may be especially beneficial for interfaces and joints in high-precision devices and structures (particularly, miniature ones) which require very thin preforms with well-defined dimensions - the requirement that may be difficult to satisfy with traditional adhesives and bonding methods.

Results of the performed experimental studies of the CNT SPS effect on the strength of two different composite lap joint configurations allow us to conclude that significant improvement in Mode I fracture toughness observed in respective DCB tests does not translate directly into the lap joint strength. Due to the peel stress at the ends of the tested single lap joint seems to fully control its failure initiation, and because of the joint experiences instantaneous failure, the obtained increase in the “propagation”  $G_{IC}$  values by the CNT SPS interleave embedment does not considerably affect the joint failure load. In the case of a double strap joint, the shear stress rather than the peel stress, dominates in the joint failure. This makes no correlation between the double strap joint strength and the DCB mode I fracture toughness data. Mode II interlaminar fracture toughness tests are required to establish such a correlation. On the other side, the joint test data revealed that infused CNT SPS interleave incorporated within a double-strap joint takes significant portion of the load and thus increases the failure load and failure strain values. All these effects deserve further comprehensive studies.

The aligned sheet of interconnected CNTs was drawn from a CVD grown CNT array and then bonded to the surface of glass fiber/epoxy laminates. Various types of mechanical tests were conducted with that drawn sheet (DS), accompanied by real-time electrical data acquisition, in order to evaluate its electro-mechanical behavior. Specimens were loaded in the longitudinal and transverse DS orientations to investigate the anisotropy of the piezoresistive effect. The DS exhibited good sensing stability, linearity, sensitivity and repeatability within a practical strain range; these are crucial sensor features for health monitoring. It was also demonstrated that the CNT orientation in the DS had a dramatic effect on the sensitivity, thus validating the usefulness of this sensing material for directional strain/damage monitoring. Also, pre-straining of the CNT DS sensors was conducted to further enhance the linearity of electro-mechanical response and long-term stability of the sensing response under cyclic loading.

Two methods of sensing adhesive joints and monitoring of the strains generated within adhesive layer were explored with the use of embedded CNT SPS and CNT DS and measuring their electrical resistance change under loading. These CNT materials showed sufficiently sensitive to the change of high internal strains generated within adhesive layer of the joint which is not easy to accomplish with other known sensor types. Besides, both CNT SPS and CNT DS integrate well within the joint and do not affect negatively its strength, contrary to what is commonly observed with many other sensors.

Finally, a unique novel combination of an essentially two-dimensional CNT DS and an essentially three-dimensional CNT SPS was used for the strain sensing in composite adhesively bonded joints. The SPS was integrated near the overlap ends only in the form of narrow strips and it showed many times higher electrical resistance change than the DS under equivalent nominal strain level. This is attributed to the added capability of sensing the transverse peel strain, which has much higher values compared to the longitudinal in-plane strain near the overlap ends. The transverse peel strain is especially difficult to monitor in composite bonded joints, so this novel sensing method opens new opportunities in this direction. Overall, the studied novel CNT sheet sensor materials possess excellent strain sensing capabilities, are easy to handle and embed. In order to complete their practicality studies, a calibration has to be performed in the next step, and their gauge factors have to be determined accordingly.



## **CHAPTER 1. MICRO- AND NANO-REINFORCED INTERLEAVES FOR LAMINATED COMPOSITES**

This chapter presents a brief review of major historic works and modern trends in the field of laminated composites enhanced with various type fiber reinforced interleaves. The primary practical purpose of such interleaves is to either prevent delamination onset or arrest catastrophic delamination propagating through weak interfaces in composite laminates. A general categorization of interleaves introduced here helps to identify the place of novel carbon nanotube reinforced interleaves used throughout this project.

### **1.1. Interface Enhancements in Demand for Laminated Composites**

It has been known for several decades that overall strength of composite laminates and their joints critically depend on their ability to resist the initiation and propagation of delamination caused by interlaminar stresses/strains which may reach very high values in the vicinities of free edges, corners, open holes, joint bondlines, junctures with stiffeners and other structural features where sharp geometry change and/or step-wise material property variation take place. If the composite laminate's resistance to interlaminar stresses is insufficient, delamination can propagate deep into the structure and ultimately result in a catastrophic structural failure. Comprehensive analyses and reviews of the origins of delamination initiation, growth and structural consequences can be found in numerous publications, such as extensive bibliography compendium [1] and review papers dedicated to free edge effect [2, 3], composite bonded joints [4, 5, 6], bolted and mechanically fastened joints [7, 8, 9, 10].

The other well-known concern is so-called “barely visible damage” which may be initiated by an incidental drop weight impact, bird strike, ice, hail, stone hits, etc. Typically this kind of localized damage starts with matrix cracks which then advance to composite interfaces and initiate delamination; reviews of this problem can be found in [11, 12]. The subsequent unrestricted delamination growth under in-service loads (e.g. quasi-static tensile, compressive and flexural ones with often superposed vibrational forces) may result in a catastrophic structural failure if the interface does not possess sufficiently high inherent fracture toughness and/or if there are no additional delamination arresting “barriers” embedded between adjacent composite plies.

Among most popular means used in the early works for arresting delamination were thin toughened interleaves placed between composite plies. Those were either covering large areas or were localized in the form of narrow strips; a comprehensive review of those works can be found in [13]. Various materials have been attempted, including toughened specialty thermoset adhesive films (those usually showed highest success), thermoplastic films (with widely varying success), and various fiber-reinforced (e.g. glass, aramid, carbon) interleaves. The latter category of interleaves often showed unpredictable results – in many cases even negative effects on the laminate fracture toughness – which made it difficult to assess any general trends.

Among more recent interleave reinforcement types were electrospun nanofiber random mats, carbon nanotube random buckypapers, and chemical vapor deposition (CVD) assisted vertically

grown carbon nanotube “arrays” (a.k.a. “forests”), which have preferential alignment in their growth direction. A brief review of the latter category, which is the closest to the subject of this report, is presented in the next section. It is believed that new technological developments of nano-scale reinforced interleaves will open new avenues for the interface enhancements of laminated composite structures.

## 1.2. Categorization of Interleaves

The concept of interleaving adopted here is illustrated in Figure 1.1, where “interlayer” is depicted as three-layer structure with an interleaf “sandwiched” between two resin-rich layers. The interleaf is defined as distinct material entity placed between the host composite plies. Figure 1.1 further illustrates most popular categories of interleaves known from the literature.

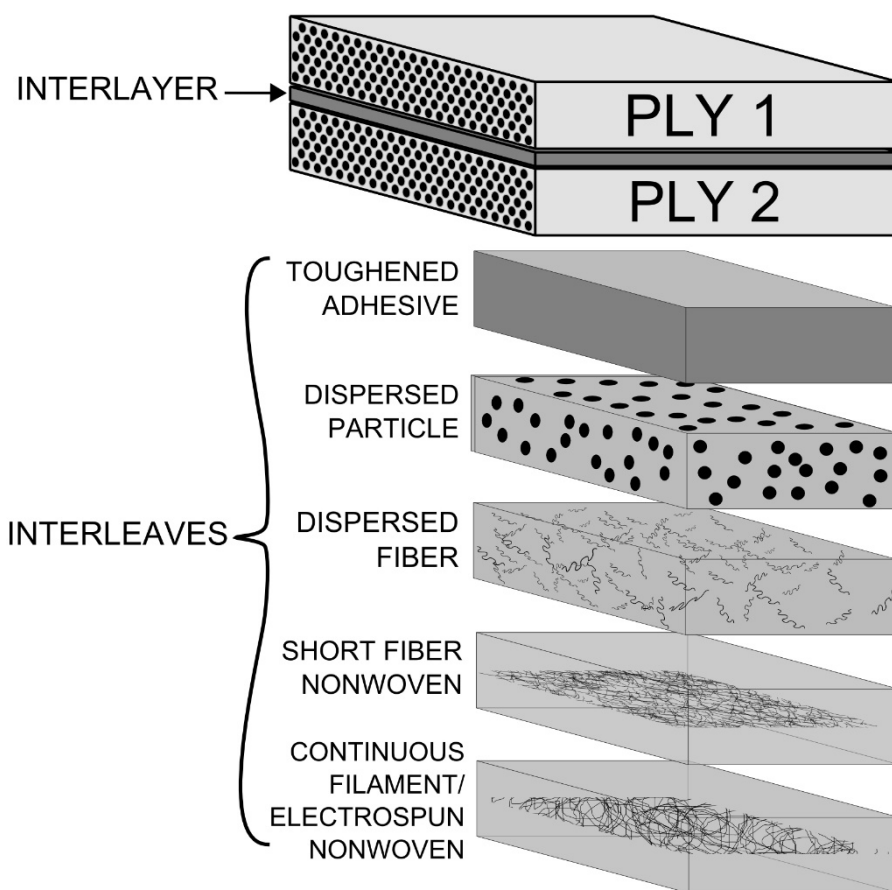


Figure 1.1. Illustration of the interlayer concept and classification of the known interleaves comprised within interlayer.

The earliest, and most popular category of interleaves, is toughened films made of thermoset or thermoplastic polymers which have much higher fracture toughness and, typically, lower stiffness than the host resin material. That category naturally evolves into dispersed particle reinforced interleaves and short fiber reinforced interleaves which are usually prepared by

mixing low volume content particles/fibers with some thermoset or thermoplastic resin material. A more recent and more complex category is textile reinforced interleaves, which can be subdivided into short fiber nonwovens, continuous fiber/electrospun nonwovens and various woven fabrics. Short fiber nonwovens are comprised of randomly oriented fibers, which can be thermoplastic, carbon, or glass ones. Continuous fiber nonwovens typically encompass electrospun fiber mats, but could also include textile materials processed by other means. Representative examples of this category can be found in [16, 17, 18]. Specifically, interleaves made of electrospun fiber mats have been reported in [19, 20, 21, 22, 23, 24] amongst many other works. Both fibrous and particulate reinforcements are classically in the micron range for diameters (i.e. those are termed “micro-reinforcements”).

Recently more research has been done with nanofibers and nanoparticles, and those can be termed “nano-reinforcements”. In the case of electrospun nanofibers, their diameter is typically in the range of hundreds of nanometers.

CNT materials have been used in several different ways as interleave reinforcements; interesting examples can be found in [25, 26, 27, 28, 29]. In [25] short ( $<100\text{ }\mu\text{m}$ ) CNTs were mixed at  $<5\%$  wt with epoxy; the resulting modified resin was then infused into a dry fabric or used directly as an interleaf between prepreg plies prior to cure. In [26] short CNTs were made into solvent slurry and then formed into a buckypaper through solvent evaporation. In [27] the buckypaper was used as an interleaf, either dry or infused with resin. In [28, 29] a short CNT array was placed onto a prepreg ply surface with some nanotube alignment and then cured.

One principal effect anticipated from embedding high volume fraction carbon nanotube (CNT) reinforced interleaves is, that the localized interlaminar strain gradients can be substantially reduced at the micro-scale, i.e. at the scale of individual fibers within composite plies. This interface micro-reinforcement concept is similar to what is observed in a variety of nature materials and their joints (excellent reviews on this topic can be found in [14]). Nature optimizes hard-to-soft tissue joints and attachments by generating complex transitional composite interphase materials with gradual transition of elastic properties from “hard” to “soft”. That is achieved by many simultaneous means, for example by gradual variation of the reinforcing nanoscale elements’ orientation and volume fraction combined with their varying stiffness, strength and ductility. Learning from the nature’s approach and attempting to mimic it with specific three-dimensional (3-D) architectures of carbon nanotube engineered composites was one of the principal motivations for this research project.

The other anticipated effect of embedded CNT-reinforced interleaves is that their own fracture toughness should be far beyond that of a regular prepreg resin matrix due to a (i) huge surface area of CNTs within a unit volume and (ii) exceptional combination of high stress and strain to failure values of individual CNTs. Conceptually, when an initial delamination tip faces a CNT-reinforced interleaf, it can either pass through (which would inevitably result in a branching into numerous “nanocracks” with much higher than usual energy release rate) or to deviate from its initial path and propagate outside the interleaf, e.g. within much thinner than the original matrix interphase. In either case the CNT interleaf would serve its purpose by forcing the delamination to propagate along a more torturous path and, accordingly, increasing the energy release rate vs. the reference case of pure matrix interphase. Although the above outlined concept looks

attractive and realistic, the existing literature shows very little work devoted to its experimental validation and, particularly, to the quantification of the effect of thin CNT-reinforced interleaves on interlaminar fracture toughness characteristics of laminated composites. The effects of morphology of CNT reinforcement within the interleaf, their volume fraction, the bonding strength between CNTs and polymer matrix, the interleaf thickness and other structural parameters have not been assessed in the previous literature.

This report summarizes our attempts to elucidate some principal effects of the above described CNT-reinforced interleaf concept. The interleaf material is fabricated from CVD vertically grown CNT arrays by the shear-pressing method originally introduced in [15]. The shear pressing is realized here on a specialty automated device which allows one to delicately control the CNT array alignment, CNT volume fraction and the resulting shear pressed sheet (SPS) thickness. The produced thin dry SPS can be strategically placed (prior to the prepreg lamination step) within some region between composite plies and during the course of conventional laminate fabrication it would become its integral part. Under this scenario, the SPS can be partly or fully impregnated during final cure process with the resin which is already contained in the prepreg plies. An alternative manufacturing approach could be to first impregnate the SPS preform with some other, desirably lower viscosity, resin and partially cure it, then embed the “SPS prepreg” between the plies of composite and complete the manufacturing cycle.

Extensive experimental results presented in this report show how conventional double cantilever beam (DCB) testing methodology can be used to evaluate the effect of different CNT SPS interleaves on Mode I interlaminar fracture toughness (e.g., the critical energy release rate, CERR) of carbon/epoxy laminated composites. The experimental studies reported here also include traditional optical microscopy and SEM imaging of the fractured DCB samples. They show (as anticipated) that the delamination propagation path is dramatically altered in the presence of CNT SPS interleaves. It changes from a nearly straight one to a highly tortuous; the latter one typically consists of a sequence of jagged or saw-tooth type microcracks often combined with sub-micro scale cracks developing within the interleaf, and more extended microcracks propagating between the interleaf and adjacent composite ply (sometimes even penetrating into the ply and approaching the nearest carbon fibers). The overall delamination fracture mechanism becomes highly variable from sample to sample and very sensitive to the effects of CNT functionalization, to the epoxy resin viscosity, cure cycle and other characteristics, to the resin infusion technique into the SPS, the presence of residual voids, and other manufacturing peculiarities. Overall, results of this research in the part of enhancing fracture toughness of traditional laminates by embedded CNT SPS interleaves are far from being conclusive, raise many new questions, and show that this field of science and technology needs further comprehensive studies.

### 1.3. References

1. Bogdanovich, A. E.; Sierakowski, R. L. “Composite Materials and Structures: Science, Technology and Applications. A Compendium of Books, Review Papers, and Other Sources of Information.” *Applied Mechanics Reviews*, 1999, **52**, No. 12, Pt 1, 351-366.
2. Mittelstedt, C.; Becker, W. “Free-edge Effects in Composite Laminates.” *Applied Mechanics Reviews*, 2007, **60**, No. 9, 217-245.

3. Kant, T.; Swaminathan, K. "Estimation of Transverse Interlaminar Stresses in Laminated Composites – A Selective Review and Survey of Current Developments." *Composite Structures*, 2000, **49**, 65-75.
4. Matthews, F. L.; Kilty, P. F.; Godwin, E. W. "A Review of the Strength of Joints in Fibre-Reinforced Plastics. Part 2. Adhesively Bonded Joints." *Composites*, 1982, **13**, 29-37.
5. Banea, M. D.; da Silva, L. F. M. "Adhesively Bonded joints in Composite Materials: An Overview." *Journal of Materials Design and Applications*, 2009, **223**, 1-18.
6. Abdel Wahab, M. M. "Fatigue in Adhesively Bonded Joints: A Review." *International Scholarly Research Network, ISRN Materials Science*, 2012, *Article ID 746308*, 25 pp.
7. Godwin, E. W.; Matthews, F. L. "A Review of the Strength of Joints in Fibre-Reinforced Plastics. Part 1. Mechanically Fastened Joints." *Composites*, 1980, **11**, 155-160.
8. Ireman, T.; Nyman, T.; Hellbom, K. "On Design Methods for Bolted Joints in Composite Aircraft Structures." *Composite Structures*, 1993, **25**, 567-578.
9. Camanho, P. P.; Matthews, F. L. "Stress Analysis and Strength Prediction of Mechanically Fastened Joints in FRP: A Review." *Composites Part A*, 1997, **28A**, 529-547.
10. Thoppul, S. D.; Finegan, J.; Gibson, R. F. "Mechanics of Mechanically Fastened Joints in Polymer-Matrix Composite Structures – A Review." *Composites Science and Technology*, 2009, **69**, 301-329.
11. Abrate, S. "Impact on Laminated Composite Materials." *Applied Mechanics Reviews*, 1991, **44**, No. 4, 155-190.
12. Abrate, S. "Impact on Laminated Composites. Recent Advances." *Applied Mechanics Reviews*, 1994, **47**, No. 11, 517-544.
13. Sela, N.; Ishai, O. "Interlaminar Fracture Toughness and Toughening of Laminated Composite Materials: A Review." *Composites*, 1989, **20**, 423-435.
14. Thomopoulos S.; Birman, V.; Genin G. M. (eds). "Structural Interfaces and Attachments in Biology." Springer, New York, 2013.
15. Bradford, P. D.; Wang, X.; Zhao, H.; Maria, J.-P.; Jia, Q.; Zhu, Y. T. "A Novel Approach to Fabricate High Volume Fraction Nanocomposites with Long Aligned Carbon Nanotubes." *Compos. Sci. Technol.*, 2010, **70**, 1980-1985.
16. Lee, S.; Noguchi, H.; Kim, Y.; Cheong, S. "Effect of Interleaved Non-woven Carbon Tissue on Interlaminar Fracture Toughness of Laminated Composites: Part I - Mode II." *J. Compos. Mater.*, 2002.
17. Yadav, S. N.; Kumar, V.; Verma, S. K. "Fracture Toughness Behaviour of Carbon Fibre Epoxy Composite with Kevlar Reinforced Interleave." *Mater. Sci. Eng. B*, 2006, **132**, 108-112.
18. Kuwata, M.; Hogg, P. J. "Interlaminar Toughness of Interleaved CFRP Using Non-woven Veils: Part 2. Mode-II Testing." *Compos. Part A Appl. Sci. Manuf.*, 2011, **42**, 1560-1570.
19. Li, G.; Li, P.; Zhang, C.; Yu, Y.; Liu, H.; Zhang, S.; Jia, X.; Yang, X.; Xue, Z.; Ryu, S. "Inhomogeneous Toughening of Carbon Fiber/Epoxy Composite Using Electrospun Polysulfone Nanofibrous Membranes by In Situ Phase Separation." *Compos. Sci. Technol.*, 2008, **68**, 987-994.
20. Sihn, S.; Kim, R. Y.; Huh, W.; Lee, K.-H.; Roy, A. K. "Improvement of Damage Resistance in Laminated Composites with Electrospun Nano-Interlayers." *Compos. Sci. Technol.*, 2008, **68**, 673-683.

21. Zhang, J.; Lin, T.; Wang, X. "Electrospun Nanofibre Toughened Carbon/Epoxy Composites: Effects of Polyetherketone Cardo (PEK-C) Nanofibre Diameter and Interlayer Thickness." *Compos. Sci. Technol.*, 2010, **70**, 1660–1666.
22. Cuui, J. K. I. M.; Reneker, D. H. "Mechanical Properties of Composites Using Ultrafine Electrospun Fibers." *Polymer Composites*, 1999, **20**, 124-131.
23. Arai, M.; Noro, Y.; Sugimoto, K.; Endo, M. "Mode I and Mode II Interlaminar Fracture Toughness of CFRP Laminates Toughened by Carbon Nanofiber Interlayer." *Compos. Sci. Technol.*, 2008, **68**, 516–525.
24. Palazzetti, R.; Zucchelli, A.; Gualandi, C.; Focarete, M. L.; Donati, L.; Minak, G.; Ramakrishna, S. "Influence of Electrospun Nylon 6,6 Nanofibrous Mats on the Interlaminar Properties of Gr-Epoxy Composite Laminates." *Compos. Struct.*, 2012, **94**, 571–579.
25. Sager, R. J.; Klein, P. J.; Davis, D. C.; Lagoudas, D. C.; Warren, G. L.; Sue, H. "Interlaminar Fracture Toughness of Woven Fabric Composite Laminates with Carbon Nanotube/Epoxy Interleaf Films." *J. Appl. Polym. Sci.*, 2011, **121**.
26. Wang, Z.; Liang, Z.; Wang, B.; Zhang, C.; Kramer, L. "Processing and Property Investigation of Single-Walled Carbon Nanotube (SWNT) Buckypaper/Epoxy Resin Matrix Nanocomposites." *Compos. Part A Appl. Sci. Manuf.*, 2004, **35**, 1225–1232.
27. Wang, X.; Liu, W.; Jiang, Q.; Harb, M. S.; Li, Q.; Zhu, Y. "Multifunctional Nanoprepregs Based on Aligned Carbon Nanotube Sheets." *MRS Proc.*, 2012, **1407**, mrsf11-1407-aa13-03.
28. Garcia, E. J.; Wardle, B. L.; Hart, J. A. "Joining Prepreg Composite Interfaces with Aligned Carbon Nanotubes." *Compos. Part A Appl. Sci. Manuf.*, 2008, **39**, 1065–1070.
29. Abot, J. L.; Song, Y.; Schulz, M. J.; Shanov, V. N. "Novel Carbon Nanotube Array-Reinforced Laminated Composite Materials with Higher Interlaminar Elastic Properties." *Compos. Sci. Technol.*, 2008, **68**, 2755–2760.

## CHAPTER 2. CARBON NANOTUBE ARRAYS AND SHEAR-PRESSED SHEETS

This chapter presents the manufacturing approaches used for producing CVD-grown CNT arrays, then shear pressing them to self-sustained flat sheets, which can be further used in a dry or resin-infused form for interleaving laminated composites.

### 2.1. Carbon Nanotube Arrays and Their Use for Nanocomposites

CNT arrays are formed when a flat substrate is covered with catalyst nanoparticles. The catalyst nanoparticles break down hydrocarbon gases at high temperatures to nucleate and grow CNTs. If the density of the particles is high enough, the CNTs grow vertically and become self-supporting. Then they continue to grow, pushing the whole array upwards until the catalyst is deactivated. It is common for CNT arrays to reach several millimeters height. Representative images of CNT arrays grown at Co-Pi's lab are shown in Figure 2.1.

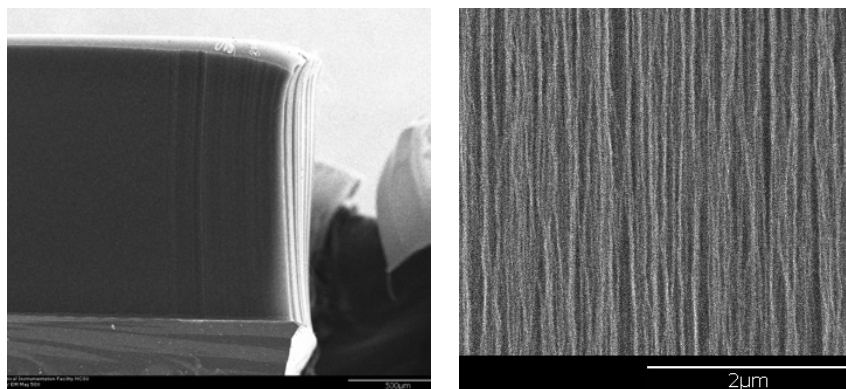


Figure 2.1. Example of CNT arrays grown at Co-PI's lab and used in the NCSU shear pressing process. The picture on the right shows excellent alignment with minimal waviness.

In order to produce an ideal consolidated structure of shear pressed CNTs, it is first necessary to study the morphology and alignment of the CNTs within the as-grown vertical array. The ideal array would possess uniform morphology from the base of the array to the top and contain long, perfectly straight nanotubes with as small a diameter as possible and high packing density of the CNTs. This is most desirable array morphology, because it would maximize the nanoscale reinforcement effects such as the total surface area of CNTs within given volume, their high length-to-diameter aspect ratio and sufficient mutual closeness for achieving full stress transfer within a CNT array composite. However, as practice shows, CVD-assisted CNT array growth methods result in very different morphologies. Although the length of CNTs may be in the range of millimeters, they are wavy, often coiled, significantly non-uniform along the growth direction, and contain large number of walls. Also importantly, the CNT density in the grown array is usually low, less than 1% by volume, which determines their lack of dimensional stability (CNTs with huge aspect ratio can easily buckle under compression, if not under own weight, in the absence of sufficient lateral support), their weakness in resistance to the resin flow, etc. These

are among the principal reasons why using as-grown CNT arrays as preforms for high performance nanocomposites appears very problematic. The alternative is applying additional forming methods which would provide better dimensional stability, increase CNT volume fraction and enforce their alignment in the desired direction(s). The shear pressing method, which has been comprehensively explored in this project and will be further described in the report, represents one promising approach to fabricate self-sustained, high volume fraction, aligned preforms for carbon nanotube reinforced composites.

The other important technological aspect is to optimize the stress transfer between CNTs via “intermediate” polymeric matrix and thus maximize mechanical properties of a nanocomposite. With this objective in mind, the two CNT functionalization methods were explored in order to add various oxygen functional groups to the nanotube sidewalls. Hydroxyl, carboxyl, and carbonyl groups are known to react well with amine side groups, as in dye chemistry, and should provide strong chemical bonds between the diamine epoxy and the functionalized nanotubes.

Many sets of experiments were conducted to find the desired CNT array growth conditions, the best CNT functionalization technique, to optimize the shear pressing angle, to assess best method of the epoxy resin infusion, and to preliminarily explore electrical resistivity of resin-infused shear-pressed sheets for possible strain sensing applications. They are described in the next section.

## **2.2. Influence of CNT Growth Conditions on the Array Morphology**

Multi-walled carbon nanotubes were grown in house using a metallic catalyst of Iron (II) Chloride ( $\text{FeCl}_2$ ) in a chemical vapor deposition (CVD) furnace. Initial conditions studied were the effect of temperature ( $760^\circ\text{C}$  and  $810^\circ\text{C}$ ) and concentration of catalyst (1 g and 2 g). The carbon source was acetylene gas dissolved in acetone fed at a rate of 600 sccm. Atmosphere was regulated by a chlorine and argon line flowed at 100 sccm and an additional argon line flowed at 300 sccm. Growth time was varied between 2.5-20 minutes to study the growth rate, which was found to be an approximate rate of  $100\text{ }\mu\text{m}/\text{min}$  up to a maximum height of CNTs of approximately 2.1 mm, at which point growth was terminated or at least slowed to a rate that approximates no growth. Some CNT arrays were post-treated at the growth temperature with the chlorine and argon flows for an additional period of time, usually 5 or 10 minutes, in order to remove excess amorphous carbon and Fe catalyst from the array and substrate. This can improve intermolecular attraction between the carbon nanotubes and promote release from the substrate. Carbon nanotube arrays were characterized using scanning electron microscopy (SEM) and some additional calculations were made to determine array densities from weight and volume measurements.

The SEM images are shown in Figure 2.2. They illustrate the different nanotube morphology over the height of the array. Nanotube structure is that of an extended helix as illustrated in Figure 2.3. This occurs due to defects in the CNT structure, thus the higher the waviness the more defects are present; such defects act as failure initiation sites.



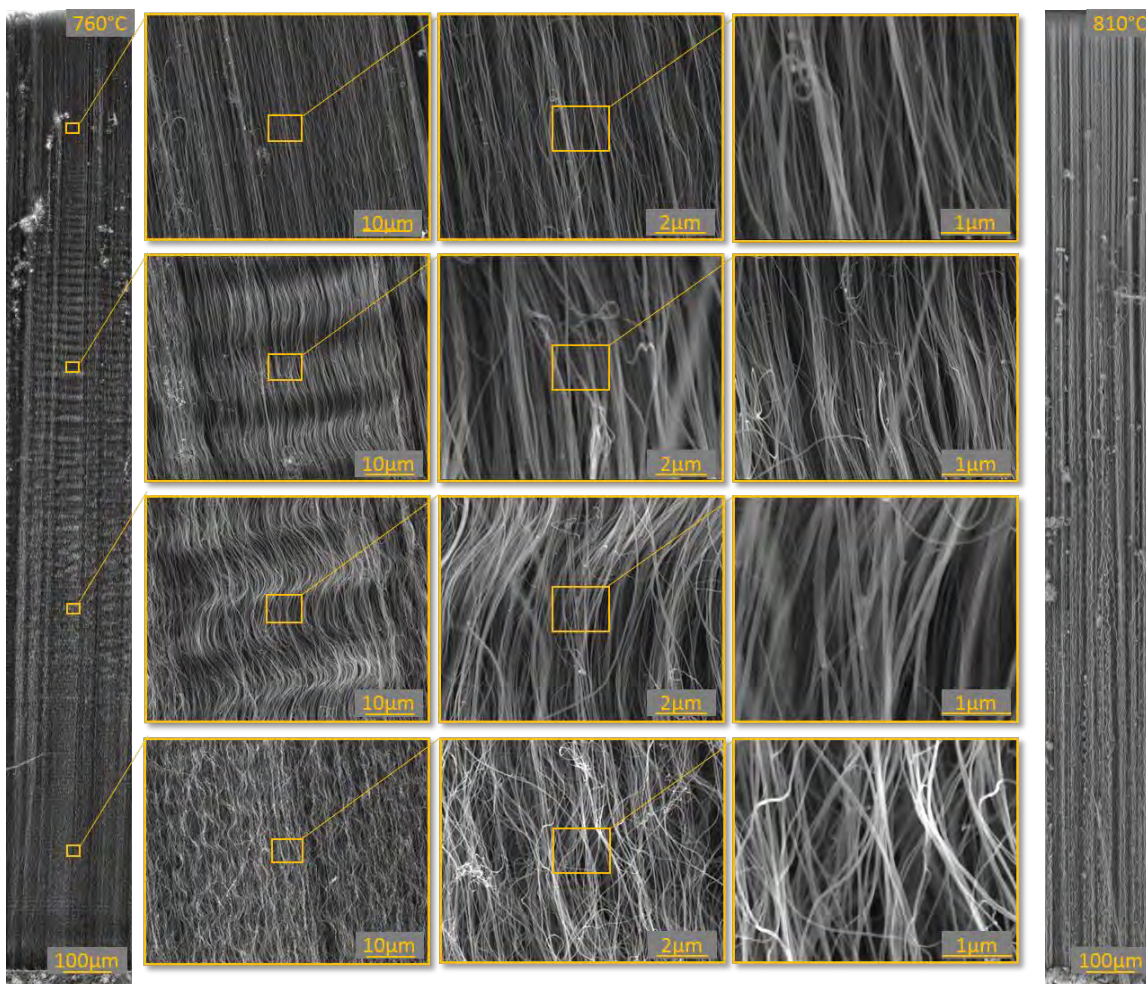


Figure 2.2. SEM images of CNT arrays grown at 760°C and 810°C.

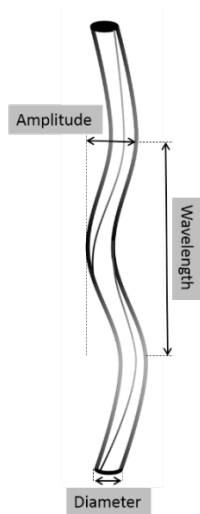


Figure 2.3. Graphic representation of CNT helical structure and characteristic measurements.

Additionally, there are, what appears to be close to perfectly straight CNTs, mixed into the dominant helical morphology. It is observed that there are three distinct regions of different helix angles and amplitudes moving from top to bottom of the grown CNT array as shown in Figure 2.3. These three characteristic regions can be distinguished in Figure 2.2 due to the changes in morphology create different areas of light and dark up the height of the array. Since the nanotube growth occurs from the substrate up, as indicated by the presence of catalyst observed at the base of the array after growth, the top of the array represents the characteristics of the nanotubes at the beginning of growth. By using Image J software, the nanotube diameter (mean sampling of 6), helix wavelength (mean sampling of 3), and helix amplitude (mean sampling of 3) were measured every 100  $\mu\text{m}$  starting at 100  $\mu\text{m}$  from the base of the nanotube array up to the 1500  $\mu\text{m}$ , as the total height of the array is slightly less than 1600  $\mu\text{m}$ . The ratio of wavelength to amplitude is a relative indicator of how close to straight nanotubes are, with higher values approaching linearity.

The principal geometric characteristics are depicted in Figure 2.4, with color indicating a relative presence of straight CNTs based on a frequency of finding them in the image. Red-colored bars indicate none straight CNTs found; blue-colored bars indicate straight CNTs found with a moderate frequency, and green-colored bars indicate that it was most frequent to find straight CNTs. These regions closely resemble the three regions of differing morphology seen in the SEMs of Figure 2.2.

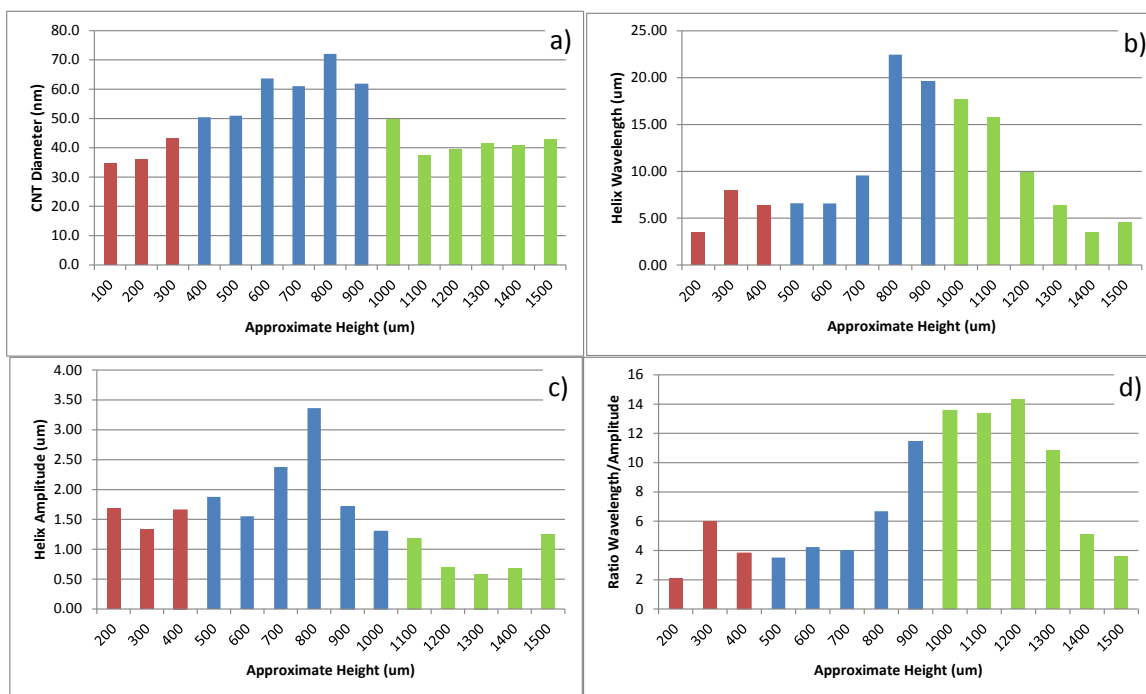


Figure 2.4. Mean data of sampled CNT diameter (a), wavelength (b), amplitude (c) and the wavelength/amplitude ratio (d) at regular intervals along the CNT height, from the base to the top. Color code explained in the text.

The variation of CNT diameter (see Figure 2.4a) shows nearly-linear growth up to  $\sim 800 \mu\text{m}$  reaching the diameter peak of  $\sim 70 \text{ nm}$ . Then sharp drop is observed till  $\sim 1100 \mu\text{m}$ , where the lowest value of  $\sim 37 \text{ nm}$  occurs; after that the diameter slowly grows again. Most frequently straight segments of the nanotubes are found in the distance range  $1000\text{--}1500 \mu\text{m}$ . Hence, the lowest diameter of around  $40 \text{ nm}$  correlates with more straight nanotube segments. Figure 2.4b shows that the helix wavelength slowly grows from  $200$  to  $800 \mu\text{m}$  distance from the base, then sharply rises and reaches its peak at  $\sim 800 \mu\text{m}$ ; then a nearly linear decrease till the top of the forest is seen. So, nearly straight nanotubes have a smaller wavelength. The helix amplitude variation in Figure 2.4c shows about twofold increase till  $\sim 800 \mu\text{m}$  distance is reached, then the amplitude sharply decreases till  $1300 \mu\text{m}$ , after which it starts increasing again. Naturally, straight segments of nanotubes can be found more frequently near the top, where the region of lowest waviness amplitudes is. It is also interesting to observe the wavelength/amplitude ratio variation in Figure 2.4d; this characteristic reaches highest values in the distance range between  $900\text{--}1300 \mu\text{m}$ .

It can be concluded from the compound of results in Figure 2.4 that a change in CNT morphology occurs once the array gets taller than  $500 \mu\text{m}$ , at which point the nanotube diameter increases and the centerline of the nanotubes becomes increasingly wavy. As perfectly straight and oriented nanotubes with uniform morphology and small diameter are desired, it appears that best array height would be approximately  $500 \mu\text{m}$ . It is also apparent that CNT growth is much more spurious at the top and at the base segments of the CNTs, meaning that the growth conditions significantly alter upon initiation and termination of the reaction. Therefore, controlling a uniformity of CNT growth conditions from start to finish is necessary for producing consistent CNT morphologies.

Two growth parameters were adjusted in order to produce a lower density array: growth temperature and amount of catalyst in the system. Growth time was constant at 10 minutes and involved no post-treatment in chlorine atmosphere. The results are depicted in Table 2.1 and show that the lowest array density is achieved at a higher growth temperature and increased catalyst concentration. Additionally, growth rate is also observed to increase with increasing growth temperature and catalyst concentration. However, due to the conflicting trends for catalyst amount between low and high growth temperatures, no clear conclusion could be drawn as to catalyst effect on array density, thus an economical decision was to use  $1 \text{ g}$  of catalyst and increase the growth temperature.

Table 2.1. Array height and density change with varying growth temperature and amount of catalyst.

Growth Temperature ( $^{\circ}\text{C}$ )	Catalyst Weight	Array Height ( $\mu\text{m}$ )	StDev	Array Density ( $\mu\text{g}/\text{mm}^3$ )	StDev
760	1g	<b>873</b>	79	<b>66.48</b>	6.7
760	2g	<b>889</b>	89	<b>95.55</b>	7.9
810	1g	<b>1021</b>	79	<b>47.41</b>	7.4
810	2g	<b>1433</b>	89	<b>22.39</b>	4.8

### 2.3. CNT Array Shear Pressing

The shear pressing process, which is the method used to produce high volume fraction aligned CNT sheets, has three main steps: 1) growing millimeter-range long CNT arrays on substrates; 2) using special shear pressing device to compress the arrays into a dense sheet with the CNTs aligned in one direction; and 3) infusing the produced CNT sheet with any desirable polymeric resin system. Particularly, relatively large and thick preregs (each with a thickness of 75-100 microns) have been fabricated earlier as demonstration samples of the novel CNT composites.

The top surface of a carbon nanotube array has been shown to have a high coefficient of friction [1]. This is most likely the result of the CNTs' relatively small size and relative immobility as compared to the other CNTs in the array. The CNT ends can fill microscopic pits and cracks in material touching the top of the array. We take advantage of this friction property to use a metal plate to shear CNT arrays horizontally, while applying a vertical force to condense the array into a dense film consisting of well aligned CNTs. Figure 2.5 demonstrates the shear pressing process conceptually. A linear bearing is used to direct the flat pressing plate at a defined angle to the CNT array.

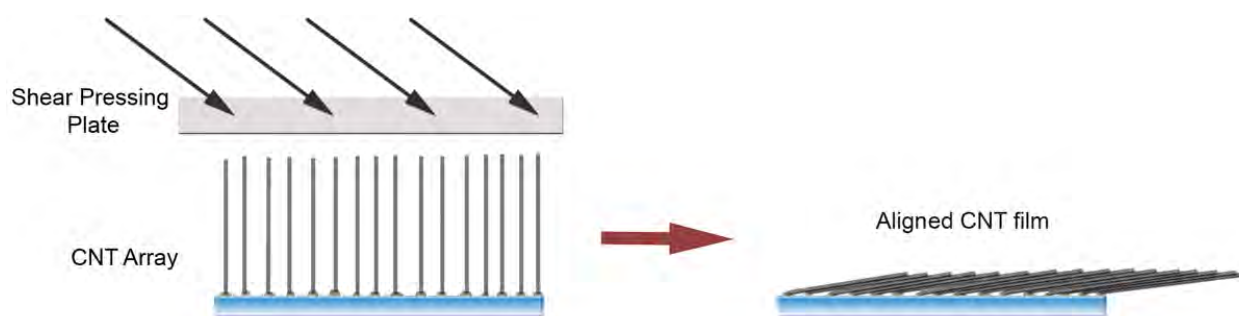


Figure 2.5. Schematic of the new process of shear pressing CNT arrays. A flat metal plate presses the arrays at a fixed angle to align them and compress them together.

In our earlier studies, the shear pressed CNT sheets infused with epoxy resins (see Figure 2.6), have shown increases in tensile strength up to 500% over the neat epoxy [2]. This is in sharp contrast with the effect obtained for dispersed CNT/epoxy composites which is usually limited to only 5-30% increase over the neat epoxy strength [3]. The huge difference between the two CNT composite systems results from the alignment of the CNTs, as well as from much longer CNTs and much higher volume fraction of the CNTs in the sheets. While the strain-to-failure of the aligned CNT composites is generally less than that of the epoxy, it was anticipated that the dramatic increase in stiffness and strength of this new CNT reinforced adhesive interleaves will have a much more influential impact on the interlaminar fracture toughness of composite laminates and on the strength of composite bonded joints. It is worth emphasizing again that this novel densified material formed from carbon nanotubes can be used either in its original dry form or as resin-infused prepreg. In both cases it is self-sustaining solid sheet, which possesses high dimensional stability in the thickness direction and keeps its shape very well. This makes it very suitable interleave material for embedment into composite laminates and bonded joints.



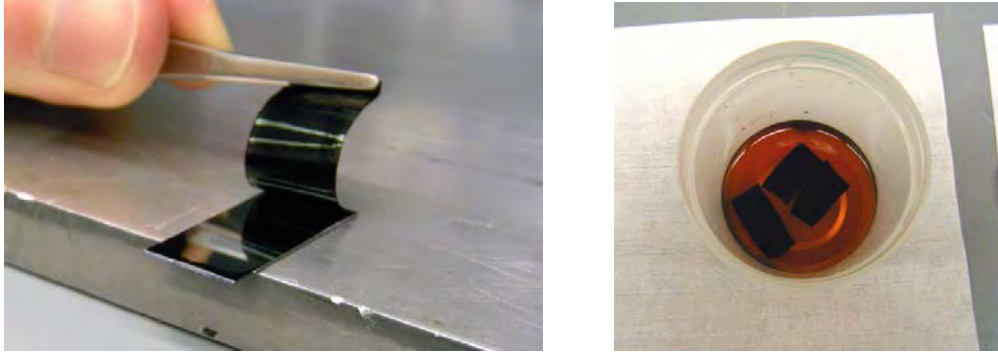


Figure 2.6. Removal of CNT shear pressed sheet from substrate (left) and sheets soaking in epoxy resin bath (right).

A recent AFOSR STTR Phase I project [4] allowed us to scale up and add automation to the shear pressing process, advancing from the earlier used hand operated device to a highly precise computer controlled shear press. The automated shear pressing is achieved by using two-coordinate press machine with synchronized horizontal and vertical displacements and precisely controlled load. The motion trajectories of the traverses (platens) are adjustable by the input into the computer controls. Figure 2.7 shows a conceptual design drawing and the actual built device, respectively.



Figure 2.7. The designed CNT shear pressing device (left) and the actual computer-controlled shear press built by 3TEX, Inc. (right).

A summary of the automated shear press capabilities and characteristics can be briefly described as follows.

(I) The shear press allows for two coordinate's motion with the load measuring system based on MiSUMi Automation Components, G&L Linear Motion control system and Loadstar™ sensors.  
 (II) The following technical characteristics can be achieved by design and construction of the press:

- a. Displacement in horizontal direction (x) up to 200 mm, nominal 5 mm

- b. Displacement in vertical direction (z) up to 200 mm, nominal 5 mm
- c. Speed in horizontal direction (x) – variable from 1 mm/min up to 100 mm/min
- d. Speed in vertical direction (z) – variable from 1 mm/min up to 100 mm/min
- e. Dimensions of work table size 200x200 mm
- f. Load active measurement up to 150 kg<sub>f</sub>
- g. PC based interface of control system.

Our research team now has the capability to grow some of the largest area vertically aligned CNT arrays in an academic research lab. These arrays are very uniform, which is important for the shear pressing process. Most CNT array processing routes involve the deposition of metal catalyst particles using a physical vapor deposition route such as sputtering or evaporation [5, 6]. This is a time consuming step due to pre-deposition pumping, and the substrate size is limited to the size of the deposition system. The method adopted by our research team is based on evaporation of a metal salt catalyst initially reported in [7]. Due to the vapor phase deposition of the catalyst particles at the beginning of the CVD process, CNTs are nucleated on any flat quartz surface in the furnace hot zone. It is a low pressure nucleation and growth process running at around 5 torr, allowing us to grow uniform arrays on large size substrates without causing diffusion limited uneven growth seen in atmospheric CVD processes. Arranging multiple substrates vertically in the furnace allows us to produce multiple large arrays in a single run. With larger CVD systems, this technology is well suited for being scaled up by future industrial partners.

Vertically aligned arrays of multi-walled CNTs were fabricated in-house using chemical vapor deposition (CVD) onto a quartz substrate. Growth conditions used an iron (II) chloride catalyst in an argon and chlorine atmosphere at 810°C with acetylene gas as the carbon source. Array height is relatively uniform across the growth surface, but can vary in the direction of gas flow up to  $\pm 100\ \mu\text{m}$  from the height at the middle of the array. CNT arrays with height ranging from  $\sim 500\ \mu\text{m}$  to  $\sim 1500\ \mu\text{m}$  have been grown and used for the interleaves in our broader research, but for the part of work reported here the CNT array height was adjusted to  $\sim 500\ \mu\text{m}$  by choosing specific growth time. A post treatment with the carbon feed gas turned off (Ar/Cl<sub>2</sub> atmosphere) for 10 minutes helped to remove excess amorphous carbon that improved interaction amongst the CNTs and their improved interaction with the epoxy resin infused into the shear-pressed interleave preforms.

The automated shear pressing device shown in Figure 2.8 allows for linear application of a defined force at the trajectory angle available from 0° to 90° (the angle is measured from horizontal direction), or in parabolic trajectory. This is achieved by computer-controlled two-directional movement of pressing plates; the upper plate moves vertically while the lower one moves horizontally. Optimal shear pressing angles have been determined to be between 20°-35° in order to avoid loss of alignment of the CNTs, especially those located near the sheet surface. Within this angle range, undesirable effects of slipping or buckling (resulting from the lower plate sliding over the surface of the CNT sheet after the peak compression is reached) are minimized. Excessive vertical compression can be avoided by utilizing the force sensing of the device, which can be programmed to stop at a specified compression force. The product of this operation is termed here a “shear-pressed sheet” (SPS). All SPS samples used in this study were

only prepared under the linear force trajectory because the parabolic one (which enables for a more gentle consolidation of the structure) has not been yet optimized for variations in array height and would add more variability to the resulting SPS morphology.

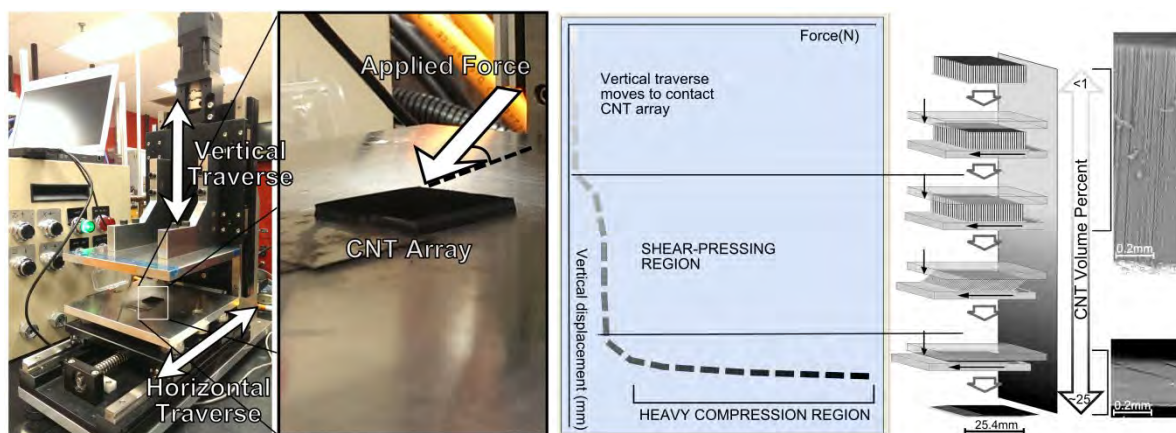


Figure 2.8. Automatic shear press with a graphic illustrating the process of shear pressing CNT arrays. SEM images to the right show the cross section of an array before (top) and after (bottom) shear pressing.

The formation of the SPS occurs in two steps: (1) shear pressing, whereby the array is “felled” and its original vertical alignment changes to a nearly horizontal, and (2) compression, during which the array with shear-induced CNT alignment is compressed with much higher force to (i) further align CNTs closer to the horizontal plane and (ii) increase the CNT volume fraction in the interleaf. The CNT inclination angle in the produced SPSs was estimated around 7°-8° with respect to horizontal plane.

As-grown CNT arrays were shear pressed at the chosen force trajectory angle of 30° to a maximum force of 500 N, which equates to 270-800 kPa of pressure, depending on the array dimensions. The resulting thickness of produced SPS samples was ~75 μm. It was measured for each sample using a Mitutoyo IP65 micrometer accurate to 1 μm. The in-plane dimensions of SPS samples were 25x75 mm with CNT alignment induced along the 75 mm dimension. Figure 2.9 shows that dominant unidirectional CNT alignment is present in the SPS, which has thus been consolidated into a solid sheet. The sheet can be securely separated from the press plate and able to keep its integrity and shape under delicate handling. In this way, the dry CNT sheet production is complete. After that it can be either placed directly onto the prepreg (further termed as the case of “dry interleaf”) or pre-infused with appropriate resin and then placed onto the prepreg (termed as the case of “infused interleaf”).

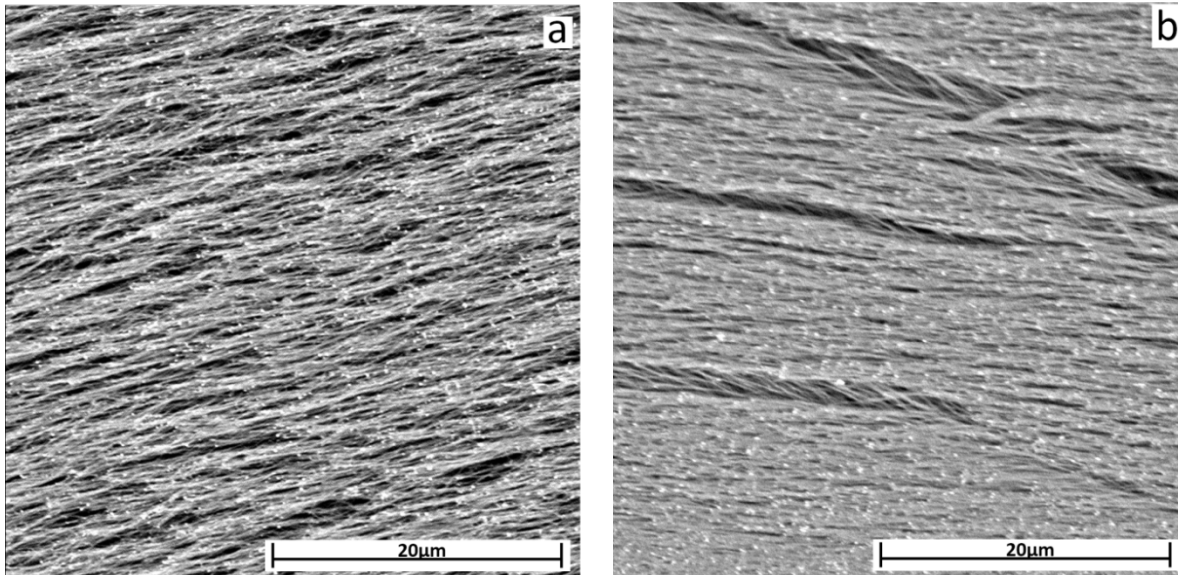


Figure 2.9. SEM images of shear pressed CNT sheet: top view (a) and cross-sectional view (b).

## 2.4. CNT SPS Functionalization

In order to improve transfer of stress from matrix to the carbon nanotubes it is necessary to add functional groups to the sidewalls of the CNTs in order to promote strong chemical bonds with the matrix. Only the Epotek resin was used in this project to study the effects of functionalization as both resin systems are diamine based, and they should react similarly with the chosen functional groups. Oxygen functional groups would be ideal as they have been shown to form chemical bonds with amines, as in dye chemistry of organic fibers. It is important for the functionalization process to have no negative impact on the advantageous properties of the CNTs, particularly their high aspect ratio and anisotropy. Traditional wet processes mix nanotubes in an oxidizing bath at elevated temperatures using an acidic compound and an oxidizing agent. This approach damages the CNT structure causing a drastic reduction in tensile properties, and often results in “cutting” the nanotube into smaller segments. Paper [8] provides a good review of the chemistry of CNTs that includes common methods of adding functional groups, where functional groups are attached along the nanotubes, and advantages/disadvantages of the various methods.

Oxygen plasma functionalization optimized for MWCNTs is shown in [9] to preferentially add hydroxyl groups to CNT arrays. Using exactly same procedure as in above cited work, CNT arrays were treated here in  $O_2/CF_4$  plasma in a capacitive coupled dielectric barrier discharge atmospheric pressure plasma system. The custom-built system consists of two parallel Cu plate electrodes ( $60 \times 60 \text{ cm}^2$ ), with a spacing of 3 cm. The plasma was operated by a 4.8 kW audio frequency power supply at 1.67 kHz. All treatments were carried out for 5 minutes in 1.0% oxygen + 1.0%  $CF_4$  + 98% helium gas mixture (by mass). After treatment, the arrays were immediately shear pressed (as will be described later in the report) and infused with epoxy resin.



Acidic wet chemical oxidation was also studied because it is the most likely method to generate sidewall functional groups to the CNTs according to [8]. A novel wet oxidation method was adapted from the process described in [10], which was used on disperse nanotubes, in order to add functionalized groups to the CNTs without sacrificing their alignment within the SPS or their aspect ratio. By taking advantage of the structural stability of the SPS, it was possible to rinse the SPS preform with liquid without sacrificing CNT alignment of the structure. In one particular procedure, four SPSs were placed on top of a quartz Buchner funnel which is drawing vacuum, as depicted in Figure 2.10. The SPSs were then alternately rinsed with 10%  $\text{H}_2\text{SO}_4$  and 1N  $\text{K}_2\text{MnO}_4$  for 30-45 minutes and were also rinsed with liberal amounts of DI water in order to remove  $\text{K}_2\text{SO}_4$  and  $\text{MnSO}_4$ . It was observed that there was also a small amount of brown particulate on the SPSs, which is assumed to be the insoluble  $\text{MnO}_2$ , despite the absence of any applied heat. The SPSs were rinsed with concentrated  $\text{HCl}$  to form  $\text{MnCl}$ , which was then rinsed out of the structure with DI water. The SPSs, still on the funnel, were placed in a vacuum oven at  $50^\circ\text{C}$  for approximately 15 minutes to dry, at which point they could easily be removed then infused with resin.

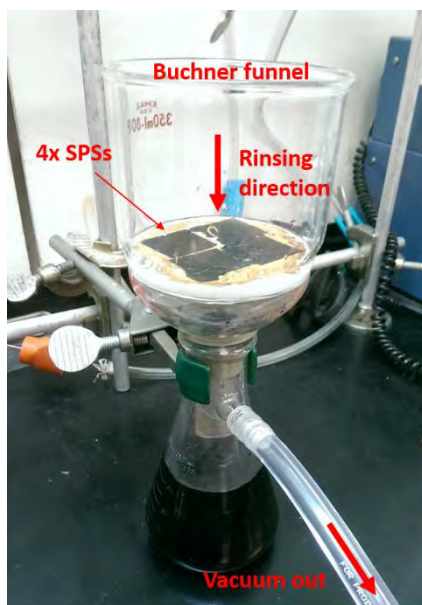


Figure 2.10. Acidic wet chemical oxidation set-up.

A result of the CNT functionalization within the SPS has been initially evaluated by using a water contact angle measurement with a  $3\ \mu\text{L}$  droplet of DI water on what was the top of the CNT array as well as the bottom. Measurements were taken from images captured from a video at times of 0, 1, 5, 10, and 15 seconds. Figure 2.11 shows representative images of contact angles one second after wetting the surface of the SPSs.

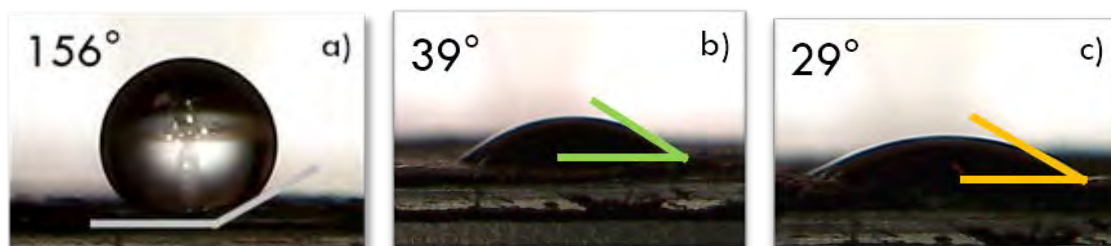


Figure 2.11. Contact angle at 1 second after wetting for non-functionalized SPS (a), acid functionalized (b), and plasma functionalized (c).

Three measurements were averaged for each image using Image J software; those are summarized in Table 2.2. These results show that both functionalization methods are effective in adding hydrophilic functional groups to the CNT surface. They also indicate that the plasma treatment is seemingly more effective due to the much lower and more uniform contact angles on both sides of the SPS. The acidic treatment showed more effective on the surface of the SPS to which the oxidants are applied; that result suggests that the rinsing procedure has not been optimal for achieving uniform functionalization.

Table 2.2. Mean Contact Angle 3uL DI water.

Specimen	Time (s)				
	0	1	5	10	15
<b>Non-Funct. Top</b>	154	156	151	146	141
<b>Non-Funct. Bottom</b>	102	100	81	76	72
<b>Acid Top</b>	41	39	32	28	26
<b>Acid Bottom</b>	80	75	66	66	61
<b>Plasma Top</b>	39	29	17	5	0
<b>Plasma Bottom</b>	30	23	15	0	0

## 2.5. Tensile Testing of Non-functionalized and Functionalized CNT SPS Composites

In order to evaluate the effect of functionalization on stress transfer efficiency in the CNT SPS/Epoxy nanocomposites, the SPS preform was infused with Epotek 301-2 resin system heated to 80°C in a microwave, at which point excess resin was removed and the structure partially cured. Then, the fabricated prepreg nanocomposite was cut into 1-2 mm wide strips for tensile testing, and then fully cured and bonded to tabs. Thickness and width were recorded for each specimen. The tensile coupon loading direction was aligned with the preferential CNT alignment direction. A minimum of 3 specimens per each material kind were produced and tested. Gauge length was 7 mm, and the displacement rate was purposely chosen very low, at 0.1 mm/min.

The obtained stress-strain curves for all tested specimens are shown in Figure 2.12, where “N”, “A” and “P” correspond to non-functionalized, acid-functionalized and plasma-functionalized SPS, respectively.

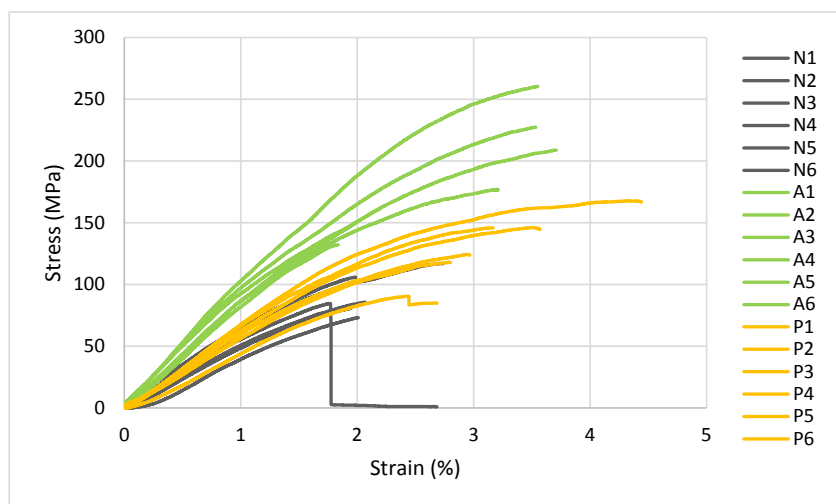


Figure 2.12. Stress – strain curves for non-functionalized, acid-functionalized and plasma-functionalized SPS reinforced nanocomposites.

Results for the tensile modulus, maximum force, maximum stress, maximum strain and break force averaged within each group of the tested materials are summarized in Table 2.3. They show that both CNT functionalization methods used here are effective in improving the ultimate failure stress and strain of the SPS nanocomposites. The acid functionalization increases modulus by 62%, failure stress by 113% and failure strain by 42% while the plasma functionalization makes respective increases by 8.7%, 45% and 52% respectively over the non-functionalized SPS nanocomposite. Thus, the CNT reinforcement effect shows stronger in the case of acid functionalization, while the plasma functionalized nanocomposite reveals more of a “ductile” behavior. This difference was not expected *a priori*, before the mechanical tests were performed, since the characteristic contact angles (according to the data in Table 2.2) were lower for the plasma treated SPS, and that suggested the presence of more oxygen functional groups. Therefore, apparently better “wetting” of the CNTs in SPS by the epoxy resin, if achieved by some specific functionalization method, does not guarantee a higher modulus or higher failure stress of the nanocomposite.

Table 2.3. Summary of SPS nanocomposite tensile testing.

Sample	Max Modulus (GPa)	Max_Force (N)	Max_Stress (MPa)	Max_Strain (%)	Break_Force (N)
<b>Non-Functionalized</b>	5.843	13.72	91.18	2.12	11.62
<b>Acid</b>	9.483	29.26	194.42	3.00	29.25
<b>Plasma</b>	6.352	19.92	132.07	3.23	19.84

One possible hypothesis to explain these trends is that the plasma treatment mostly creates adsorbed functional groups that are not chemically bonded to the CNT sidewalls, which yields the much improved wetting but only minimal improvement to the stress transfer efficiency and, consequently, to the tensile modulus. On the other hand, the carboxyl functional groups produced by the acid treatment are more reactive than the hydroxyl groups produced by the plasma treatment; besides, the former ones are able to react more effectively with the epoxy resin amine groups. This difference between the two functionalization methods may lead to a more pronounced “structural consolidation” effect on the nanocomposite and, accordingly, result in higher tensile modulus and failure stress values.

## 2.6. References

1. Kinoshita, H.; Kume, I.; Tagawa, M.; Ohmae, N. “High Friction of a Vertically Aligned Carbon-Nanotube Film in Microtribology.” *Appl. Phys. Lett.* 2004, **85**, 2780-2781.
2. Bradford, P.D.; Wang, X.; Zhao, H.; Maria, J.; Jia, Q.; Zhu, Y. “A Novel Approach to Fabricate High Volume Fraction Nanocomposites with Long Aligned Carbon Nanotubes.” *Composites Sci. Technol.* 2010, **70**, 1980-1985.
3. Rana, S.; Alagirusamy, R.; Joshi, M. “A Review on Carbon Epoxy Nanocomposites.” *J. Reinforced Plastics and Composites*, 2009, **28**, 461-487.
4. Air Force STTR Phase I, “Multifunctional Prepregs and Laminated Composites Made by Shear Pressing Carbon Nanotube Arrays.” May 2010 – March 2011, completed. PI: Dr. Alexander Bogdanovich, 3TEX, Inc. Program Manager: Dr. Les Lee, AFOSR.
5. Zhang, H.; Cao, G.; Wang, Z.; Yang, Y.; Shi, Z.; Gu, Z. “Influence of Ethylene and Hydrogen Flow Rates on the Wall Number, Crystallinity, and Length of Millimeter-Long Carbon Nanotube Array.” *J. Physical Chemistry C*, 2008, **112**, 12706-12709.
6. Chakrabarti, S.; Kume, H.; Pan, L.; Nagasaka, T.; Nakayama, Y. “Number of Walls Controlled Synthesis of Millimeter-Long Vertically Aligned Brushlike Carbon Nanotubes.” *J. Physical Chemistry C*, 2007, **111**, 1929-1934.
7. Inoue Y.; Kakihata K.; Hirono Y.; Horie T.; Ishida A.; Mimura H. “One-step Grown Aligned Bulk Carbon Nanotubes by Chloride Mediated Chemical Vapor Deposition.” *Appl. Phys. Lett.*, **92** 2008.
8. Tasis, D.; Tagmatarchis, N.; Bianco, A.; Prato, M. “Chemistry of carbon nanotubes.” *Chem. Rev.*, **2006**, *106*, 1105–1136.
9. Stano, K. L.; Carroll, M.; Padbury, R.; McCord, M.; Jur, J. S.; Bradford, P. D. “Conformal Atomic Layer Deposition of Alumina on Millimeter Tall, Vertically-Aligned Carbon Nanotube Arrays.” *ACS Appl. Mater. Interfaces*, **2014**, *6*, 19135–19143.
10. Wepasnick, K. A.; Smith, B. A.; Schrote, K. E.; Wilson, H. K.; Diegelmann, S. R.; Fairbrother, D. H. “Surface and Structural Characterization of Multi-walled Carbon Nanotubes Following Different Oxidative Treatments.” *Carbon*, **2011**, *49*, 24–36.

## CHAPTER 3. FRACTURE TOUGHNESS OF COMPOSITE LAMINATES WITH EMBEDDED CNT SPS INTERLEAVES

This chapter presents experimental study of the Mode I progressive fracture of carbon/epoxy composite laminates modified with high volume fraction, aligned, non-functionalized and functionalized CNT shear pressed sheet interleaves. A dry or resin infused SPS is integrated between prepreg plies prior to the laminate cure. The obtained results show that both dry and pre-infused CNT SPS interleaves significantly, up to two times, increase the critical strain energy release rate of the baseline non-interleaved laminate. The non-functionalized, plasma treated and acid treated SPSs are used. Both functionalization methods maintain the high alignment and aspect ratio of the CNTs. Although adding the CNT functionalization step results in no significant toughening effect (e.g. increase in the  $G_{IC}$  values) compared to the non-functionalized interleaves, the characteristics of the fracture surfaces appear to be dramatically different.

### 3.1 DCB Specimen Fabrication

Composite samples were fabricated with ten plies ( $[0^\circ]_{5S}$  lay-up) of unidirectional carbon fiber prepreg (50K Sigrafil carbon fibers impregnated with TCR UF3325 epoxy resin). Five different laminates were compared with a minimum of three specimens tested per laminate: (1) “Baseline”, which is a non-interleaved laminate, (2) “Dry” interleaf, which is interleaved with an as-is (non-functionalized CNT) SPS that was not pre-infused with resin, (3) “Non-functionalized” composite interleaf, which is the non-functionalized SPS pre-infused with a low viscosity epoxy resin, (4) “Acid-functionalized” composite interleaf, which is an SPS first functionalized using the wet chemical method of an acid activated oxygenation reaction and then pre-infused with same low viscosity epoxy resin, and (5) “Plasma-functionalized” composite interleaf, which is an SPS first functionalized with the plasma method and then pre-infused with same low viscosity epoxy resin. The samples are further abbreviated to ‘B’, ‘D’, ‘N’, ‘A’, and ‘P’ respectively. For the infused samples, the low viscosity resin used was Epotek 301-2. An attempt was made to fabricate a “control” composite laminate sample with same pure low viscosity resin interleaf in order to observe the net effect of CNT SPS reinforcements on the Mode I fracture toughness. However, that pure resin interleaved laminate showed high dependency of the fracture toughness on even minor changes in the DCB specimen fabrication procedure. Due to this reason, those test data are not included here.

The resin infusion was performed after a 5-ply prepreg stack was assembled and the dry SPS was transferred to the top of the stack. At that point the resin was heated to 90°C in a microwave to decrease the viscosity to <65 cP and spread in a thin layer over the SPS. The 5-ply prepreg stack with the SPS and resin layer on top of it was then placed in vacuum at room temperature for 10-15 minutes to promote further resin infiltration inside the SPS. After that, excess resin was removed from the SPS and the other stack of 5 pre-assembled prepreg plies was added on top. In this way, either a “dry” or an “infused” SPS interleaf was integrated at the mid-surface of the laminate between top 5 and bottom 5 plies of prepreg (as depicted in Figure 3.1). The laminate lay-up was allowed to rest for a period of 24 hours under a steel plate weight (~100 Pa of pressure) in order to allow the infused SPS to partially cure so as to maintain its shape under curing pressure. The laminate samples were then cured in a hot pressed vacuum bag that simulates conventional autoclave processing at a pressure of 310 kPa and a temperature of 144°C

for a period of 2 hours per the manufacturer's instructions. Importantly, the CNT SPS reinforcement provides high dimensional stability to the interleaves in regard of their thickness and in-plane dimensions. This feature might be beneficial for practical applications in high-precision devices and structures (particularly, miniature ones) which require well-defined dimensions of the toughening interleaves and joining elements, the requirement that may be difficult to satisfy with traditional adhesives.

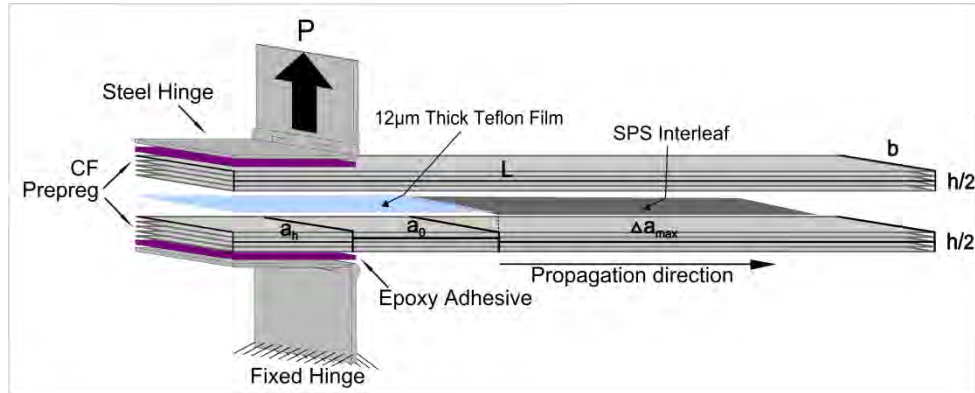


Figure 3.1. DCB Specimen schematic.

ASTM D5528 standard [1] was used when preparing composite samples for DCB testing. Specimens were cut into strips using a wet blade diamond saw and their edges were sanded smooth with 400 grit wet sandpaper. Importantly, the 'B' specimens were cut from the same panel as the 'D' specimens; this eliminates some processing variability between different material samples which were intended for a mutual comparison. White spray paint was applied to one edge of the DCB specimen in order to better observe crack propagation. The edge of each specimen was then etched every 200 µm using a laser cutter to allow for precise measurement of crack propagation. Two steel hinges with 28.5 mm length and 1.5 mm thickness were symmetrically bonded to the sample surfaces using Henkel Hysol® EA 9309.3NA epoxy, which was rapid-cured according to Henkel instructions at 82°C for 1 hour. A detailed schematic of the DCB test specimen is shown in Figure 3.1 with the specimen properties recorded for each specimen. Here, 'L' denotes the specimen length, 'b' width, 'h' thickness, ' $a_0$ ' the initial delamination length, ' $\Delta a_{max}$ ' the maximum length of delamination, and ' $a_h$ ' the length of the hinge. An  $a_0$  of ~ 70 mm was used in order to achieve the  $a/h$  ratio of ~10, and a width of ~22 mm was used, which more closely met the ASTM standard recommended specimen geometry [1]. The initial delamination was induced using 12-µm thick Teflon film; its length was precisely measured on each test specimen. The ultimate crack length  $\Delta a_{max}$  was in the range of 75-85 mm.

### 3.2. DCB Experimental

Mode I fracture toughness testing was conducted at a constant rate of displacement of 0.25 mm/min. As mentioned above, DCB testing generally followed ASTM standard [1], but there were some deviations. One of them was to not introduce a pre-crack prior to the start of data collection, due to the observed fiber bridging effect in the control specimens during preliminary tests. In fact, even the 2-mm long pre-crack could have added some toughening side effect



(which was noted in [2]), thus making it much more difficult to isolate the CNT SPS toughening effect, which was of principal interest in this study.

The other deviation from the ASTM standard was in the methodology applied for the recording and processing of experimental data. Figure 3.2 shows the experimental set-up used to record each consecutive crack propagation increment with a resolution of 200  $\mu\text{m}$ . For a steady-state crack propagation process, the load and displacement data were recorded after every 1 mm crack propagation step. For the observed instantaneous crack propagation events, data were recorded to the nearest 200  $\mu\text{m}$  crack increments. At those instants, the current level of applied displacement was paused in order to mark the crack tip location (thus allowing us to determine current crack length ‘a’). Any additional crack advancement during the paused displacement stage was also recorded, as some additional energy could still be released (though at a smaller and gradually declining rate). The camera was repositioned if necessary.

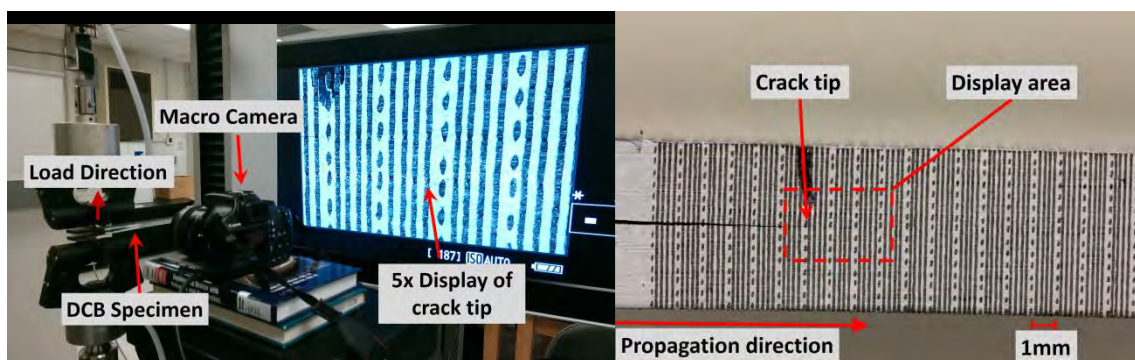


Figure 3.2. Experimental set-up (left) and sample image used to record  $\Delta a$  (right).

To study the fracture path and delamination characteristics, a dual approach was used utilizing traditional microscopy with a Motic and field emission SEM on a FEI Verios 460L. Microscopy was used to view the fracture path on the unpainted opposite side of the specimen and both fracture surfaces of the ultimately failed specimens. SEM samples were prepared by cutting a small sample from the undamaged composite panel at the crack tip and polishing the edge up to 2000 grit wet sandpaper. This allowed for a view of the interleaf cross section to evaluate the quality of resin infusion into the sheet. Once the cross section was viewed, the sample was fractured manually in a manner that imitated DCB loading. This allowed for a clean view of the fracture cross section in SEM.

### 3.3. DCB Data Processing

Load vs. displacement curves were all adjusted to “zero displacement – zero load” position, so that the slope of the curve at the initial loading stage (which is determined by the flexural stiffness of the composite beam arms) intersects with the coordinate origin of the plot. This makes all results free from the test setup variability, and particularly from a possible variation in the hinges and their attachment, specimen clamps, or errors in zeroing the load. Mode I critical strain energy release rate,  $G_{IC}$ , values were determined for all conducted tests according to “Compliance Calibration” (CC) method (a.k.a. “Berry’s” method). In addition, all other data reduction procedures recommended by the ASTM standard [1] were used and compared with the

CC method. No distinct differences between the results were found, however the CC method afforded the luxury of  $G_{IC}$  calculation before and after instantaneous crack propagation and showed the least variation for the ‘B’ type specimens. It was also concluded that the “Modified Beam Theory” and “Modified Compliance Calibration” data reduction methods yielded practically identical results, while the CC method showed a slightly smaller slope of the data.

The obtained load-displacement curves are summarized in Figure 3.3 for representative 1-2 specimens of each material kind. As seen, infused SPS interleaves produce different characteristic curves due to the observed much higher variability in the delamination propagation paths (those will be discussed later in the report).

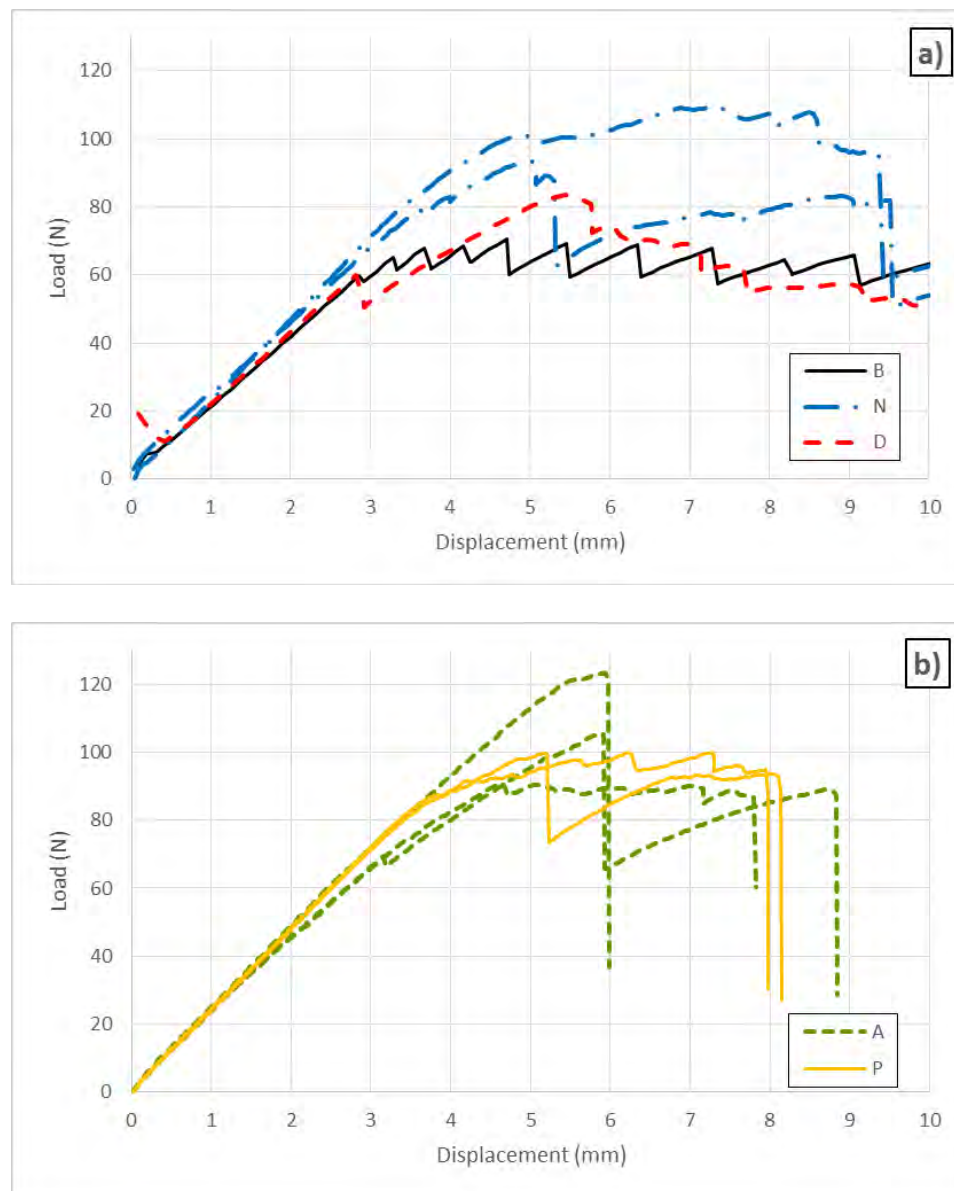
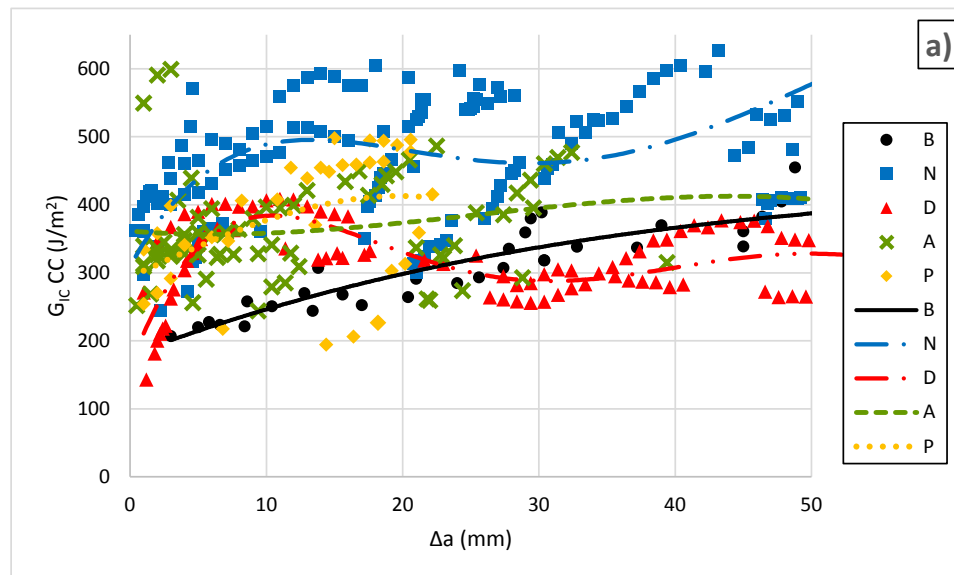


Figure 3.3. Representative load vs. displacement curves for B, D, and N interleaves (a), and A and P interleaves (b).



Figure 3.4a shows the compound of all fracture toughness results for all specimens tested; this well illustrates the observed data scatter. It has to be pointed out that in this work, unlike in traditional DCB test data collection and reduction (where  $G_{IC}$  values are calculated at specific values of  $\Delta a$ ), test data were collected here in a manner that enabled for a high-precision monitoring of each actual crack advancement and, subsequently, measuring with high accuracy each actual crack length increment  $\Delta a$ , rather than assuming equal consecutive increments. Obviously, this data collection approach makes it more difficult to visually distinguish among data sets corresponding to each individual specimen when all the data sets are shown on one plot as in Figure 3.4a. Also, mutual comparison among different materials becomes very difficult. To overcome these problems, the compound data subset corresponding to each material kind was further represented by a best fit smooth polynomial trendline at the point of  $R^2$  convergence. The corresponding five trendlines are shown in Figure 3.4b; they are commonly termed “R-curves”. As seen, with the use of adopted datapoint approximation technique, the R-curves obtained for five different material cases can be compared at a glance. To avoid any possible misinterpretation, it has to be emphasized that the original load-displacement curves in Figures 3.3a and 3.3b contain numerous load “jumps” at specific (non-equally spaced) displacement values corresponding to consecutive instantaneous crack increments. On the other hand, the smooth R-curves in Figure 3.4b do not reflect on actual crack propagation instances and their respective crack increments and should be only viewed as representing some general trends in the crack propagation process common for all specimens of each material kind.



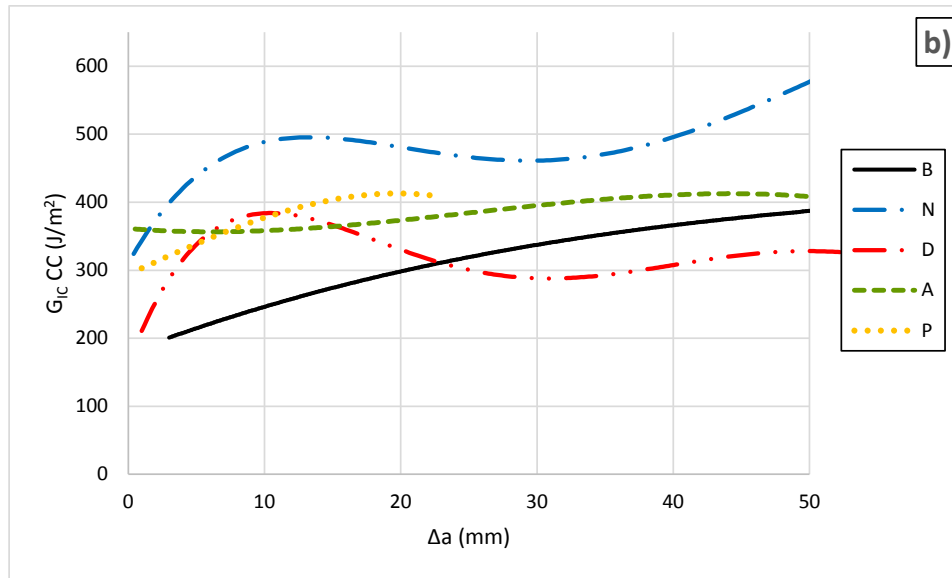
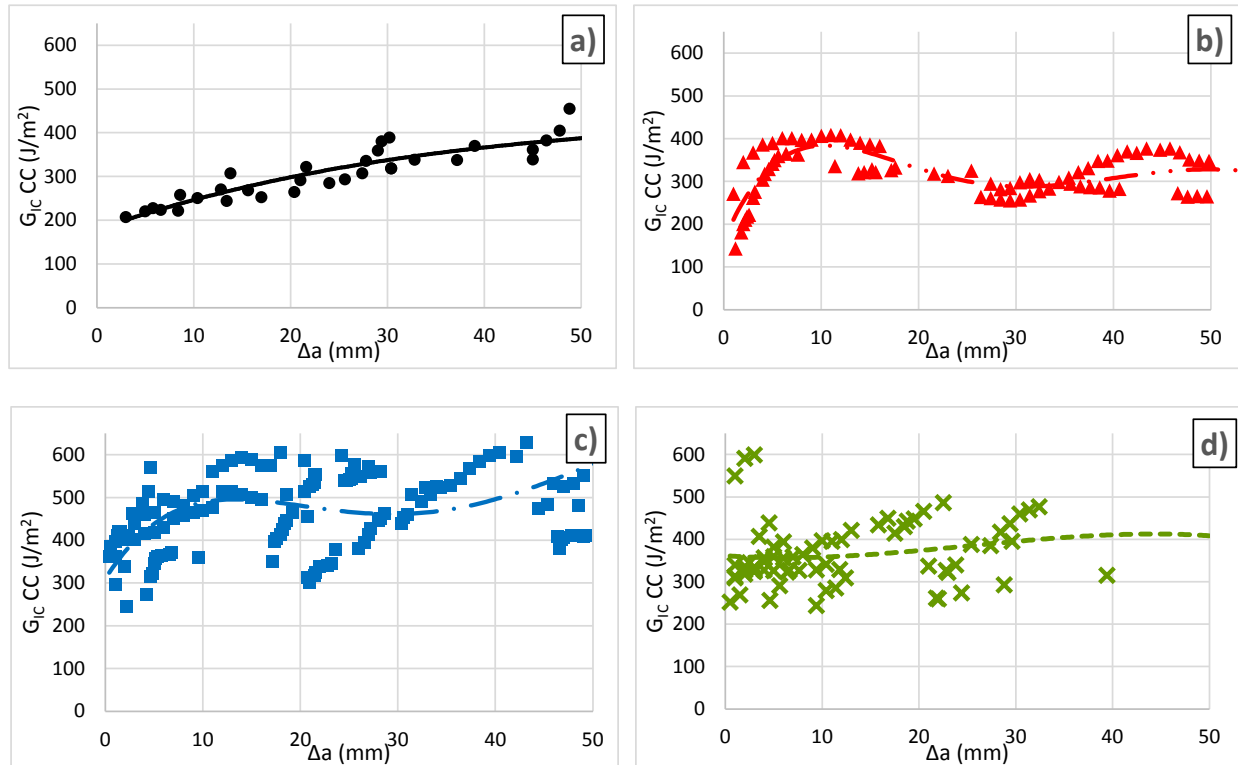


Figure 3.4. CC fracture toughness data collected for all tested specimens (a), and best-fit polynomial trendlines for each material kind (b).

To further illustrate this point, Figure 3.5 show five individual data sets and their respective trendlines; it looks like the trendlines adequately represent respective data sets (depicted by same colors).



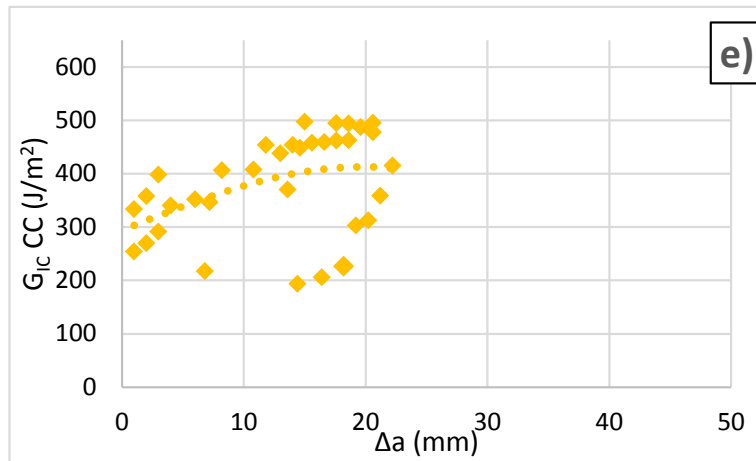


Figure 3.5. Best-fit polynomial trendlines for baseline (a), dry (b), non-functionalized (c), acid functionalized (d), and plasma functionalized (e) material types.

The advantages of the above described non-conventional data representation technique are that, if deriving such smooth trendlines, it becomes possible to (i) calculate the  $G_{IC}$  values for any desired and, importantly, any pre-determined equally spaced crack tip locations, (ii) use identical (although arbitrarily chosen) crack increments for all of the materials and all individual test specimens, and thus (iii) easily summarize and compare  $G_{IC}$  results obtained for all tested ‘B’, ‘D’, ‘N’, ‘P’ and ‘A’ type laminates in a compact way.

### 3.4. Discussion of DCB Test Results

Table 3.1 compares the percent difference in  $G_{IC}$  values for the four interleaved laminates, namely ‘D’, ‘N’, ‘P’, ‘A’; all values are normalized to the ‘B’ (baseline non-interleaved) laminate. Green color indicates an increase of  $G_{IC}$  while red color indicates its decrease vs. the baseline case. In the case of ‘D’ laminate, the highest  $G_{IC}$  increase of 61.4% is seen for the 7 mm crack length. The gradual rise up to this point closely matches the trend of the infused ‘N’ sample, but after that the ‘D’ case shows gradual reduction to 0 at ~25-mm crack length, and then increasingly negative trend up to the final 50-mm crack length recorded in these tests. This gradual decline in  $G_{IC}$ , as compared to the ‘B’ case, in the authors’ opinion is likely due to the inherent  $G_{IC}$  increase with the crack growth for ‘B’ laminate due to fiber bridging effect that competes with the  $G_{IC}$  increase owed to the SPS interleaf. Fiber bridging is well documented in the testing of unidirectional composites; it typically results in substantial “artificial” increase of Mode I fracture toughness [3], [4], [5]. The role that fiber bridging plays, if any, in adding to the toughness of the interleaved samples, is intimately dependent on the realized fracture path for each specific material; that aspect will be discussed later in the paper with support of the obtained fractography data.

Table 3.1. Percent change of  $G_{IC}$  values for different interleaved laminates over the non-interleaved baseline laminate Results were obtained with the use of trendlines with identical crack increments  $\Delta a$  taken for all five material kinds.

$\Delta a$	Dry	Infused		
		Non-Funct.	Plasma	Acid
0.2	-4.9	75.8	63.9	100.3
1	13.1	84.6	62.6	93.2
2	30.5	92.8	61.2	85.2
3	43.1	98.5	60.0	78.2
4	51.8	102.2	58.9	71.9
5	57.4	104.3	57.8	66.2
6	60.4	104.9	56.9	61.1
7	61.4	104.5	56.0	56.6
8	60.7	103.1	55.1	52.5
9	58.8	101.0	54.1	48.8
10	55.9	98.4	53.2	45.5
15	33.7	80.4	47.3	32.9
20	10.7	61.3	38.4	25.2
25	-5.9	46.1	25.1	20.3
30	-14.6	36.7		
35	-17.0	33.4		
40	-16.0	35.4		
45	-14.6	41.2		
50	-15.3	49.1		

‘N’ type laminates show significant improvement in the  $G_{IC}$  values for the whole range of crack length. Interestingly, as Table 3.1 reveals, the resin-infused interleaf yields non-monotonic variation of the  $G_{IC}$  improvement with increasing crack length, and the trend closely resembles that of the dry SPS case. The initial  $G_{IC}$  increase in ‘N’ case is 75.8%, then it grows up to the peak of 104.9% for 6-mm crack length, and after that decreases similarly to the case ‘D’. However, it still holds a 46.1% increase at the crack length of 25 mm, contrary to zero effect in the case ‘D’ for the same crack length. The minimum of 33.4% is reached in case ‘N’ for 35-mm crack, and after that the trend is another growth of the  $G_{IC}$  improvement. We do not have explanation of these peculiarities at this point, although as an upward trend in an R-curve is commonly considered indicative of fiber bridging between conventional composite plies. Based on that, we hypothesize that the initial upward trend for both ‘D’ and ‘N’ interleaved laminates may be due to the “nano-bridging” which provides significant reinforcement to the otherwise pure resin interlayer between the prepreg plies.

### 3.5. SEM and Optical Microscopy of Fractured DCB Samples

The SEM images shown in Figure 3.6 were taken at the midplane of the composite interleaves before testing. Figure 3.6a shows that no prepreg resin has reached the center region of the interleaf as the CNTs are compact but dry. Note that apparent lack of alignment is most likely a byproduct of sanding the composite surface. The infused samples show that resin has generally

penetrated through the whole thickness of the interleaf, although there is still significant number of voids present which indicates that the resin infusion technique could be further improved. Interestingly, the plasma functionalized interleaf shows the poorest quality of infusion; it needs additional investigation to assess if this is a meaningful phenomenon or just a single composite processing artifact.

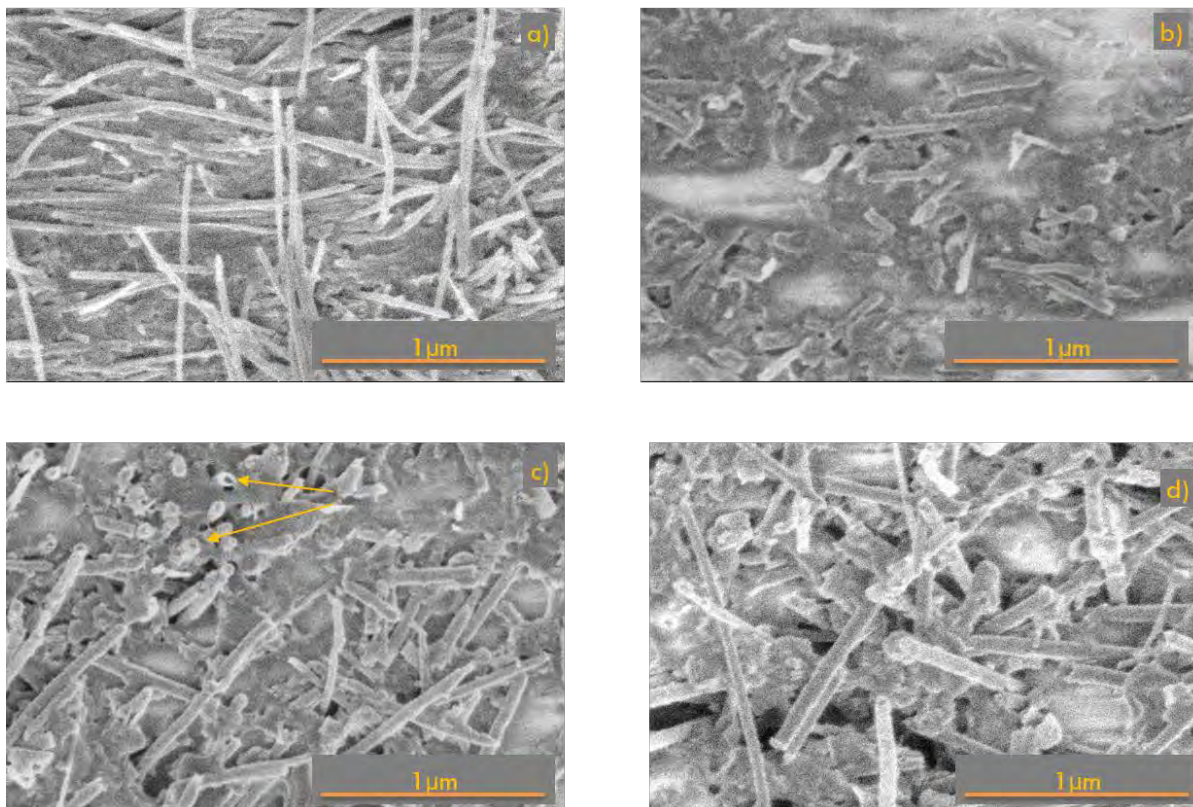


Figure 3.6. Cross-sectional images of the center region of the ‘D’ (a), ‘N’ (b), ‘A’ (c), and ‘P’ (d) interleaves.

Optical microscopy was conducted on the fracture surface of the test specimens, as depicted in Figure 3.7. Images were taken with the Teflon film located to the left of the fracture surface, meaning the leftmost side of the fracture surface images corresponds to  $a_0$ . As the majority of the fracture surface elements show black areas on symmetric sides, it is taken as an evidence that when the crack propagates through the ‘D’ interleaf, it should cause either CNT fracture at the crack tip or their pull-out from both parts of the SPS under separation, or likely a combination of both these effects; otherwise the CNTs would not be observed (in a nearly equal amount) on both fracture surfaces. By analogy with adhesive joints this can be classified as “cohesive failure” mechanism. As also seen, there is a small region with a dark CNT surface and a glossy grey surface (although the gloss is difficult to see in the image). This suggests that it is also possible for the delamination to deviate outside the SPS interleaf along the interface between the outer CNTs and prepreg resin; this can be accordingly classified as “adhesive failure” type.



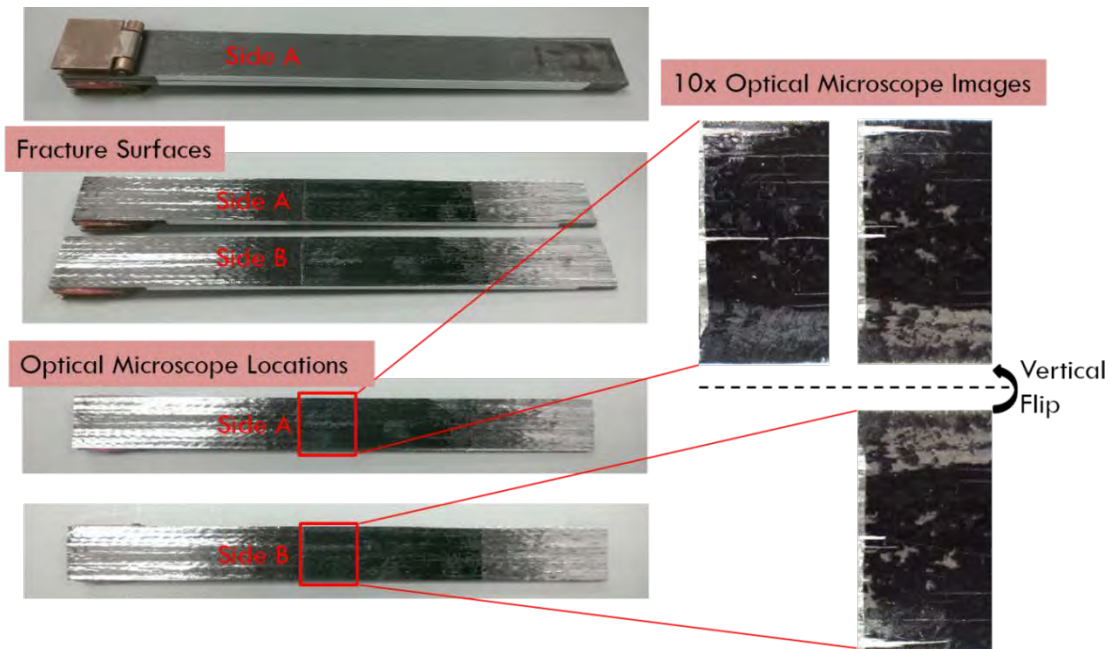


Figure 3.7. Schematic of how fracture surfaces are analyzed.

Figure 3.8 is a representative image of a 'D' specimen fracture surface, and it shows a probable propagation path through and beside the CNT interleaf based on visual surface characteristics to be discussed.

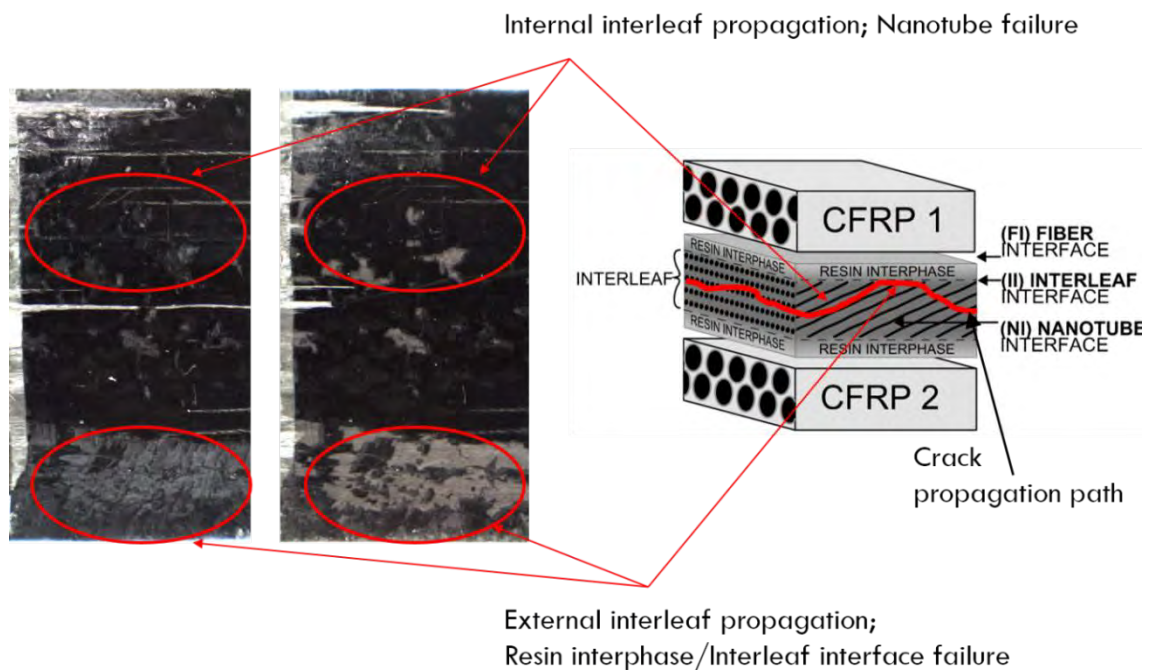


Figure 3.8. Fracture surface of representative 'D' specimen with schematic of typical crack path based on fracture surface characteristics.

Furthermore, some CNTs have probably penetrated into the prepreg resin surface layer and possibly even reached to the nearest carbon fibers. An example of such alternating cohesive-adhesive crack propagation mechanism is observed in Figure 3.9 for the ‘N’ interleaf. While there is obvious crack propagation through the SPS, there is also a crack deviation outside of the SPS and penetration into the composite ply. However, without more thorough micrography it is hard to conclude how deep and how frequent such CNT penetrations into the prepreg resin are. Ideally, extensive bridging of fibers which belong to adjacent composite plies by carbon nanotubes would be the best result, due to it eliminates the weakest link in the system – a pure resin interface. And, as denser the CNT bridging is, the higher interfacial fracture toughness shall be.

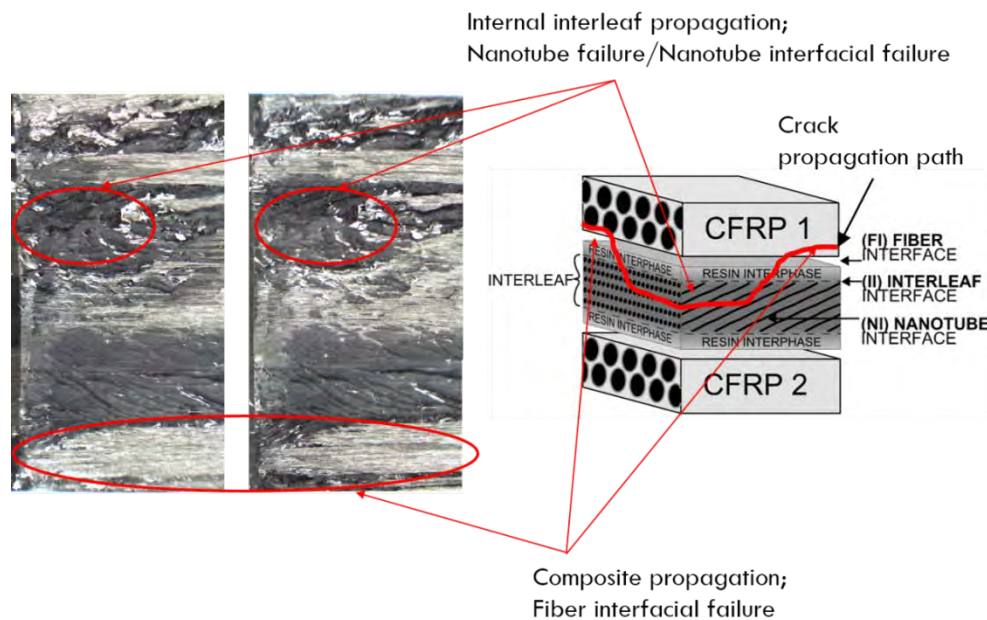


Figure 3.9. Fracture surface of representative ‘N’ specimen with schematic of typical crack path based on fracture surface characteristics.

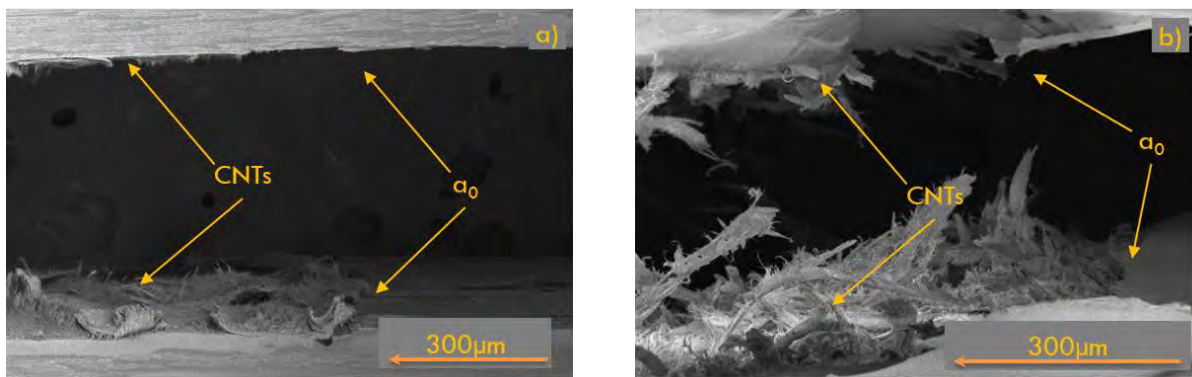


Figure 3.10. SEM of ‘D’ (a) and ‘N’ (b) near crack initiation. Scale arrow denotes crack propagation direction.

Figure 3.11 shows comparison of the fracture surfaces for the ‘D’, ‘N’, ‘A’ and ‘P’ cases. Figure 3.11a shows that numerous, seemingly random, long CNT pull-outs and long resin fracture characteristics develop during crack propagation thus leading to significant increase in  $G_{IC}$ . It is seen in Figure 3.11a (as indicated by arrows), there is a clear distinct interface between the SPS interleaf and prepreg resin which means that the latter is unable to penetrate into the SPS structure. This relatively weak interface is likely susceptible to an “easier” crack propagation. This was also seen in Figure 3.8 and Figure 3.9 as a change in crack path to a weaker interface; such a change always results in a reduced  $G_{IC}$ . Comparing the fracture surfaces of the ‘D’ interleaf in Figure 3.11a, to the ‘N’ interleaf in Figure 3.11b, it is clear that the resin infusion into SPS preform has increased the irregularity of the fracture surface. This results in increased fracture toughness for the ‘N’ interleaf. The fracture surfaces of the functionalized SPS interleaves are dramatically different from those of the non-functionalized SPS interleaves. Figures 3.11c-d show the presence of clean fracture of the CNTs and matrix, with uniform CNT pull-out, thus revealing a certain effect of the oxygen functional groups on the fracture behaviors. Relatively short CNT pull-outs (between 5-10  $\mu\text{m}$  in length) are present in both ‘A’ and ‘P’ interleaf cases.

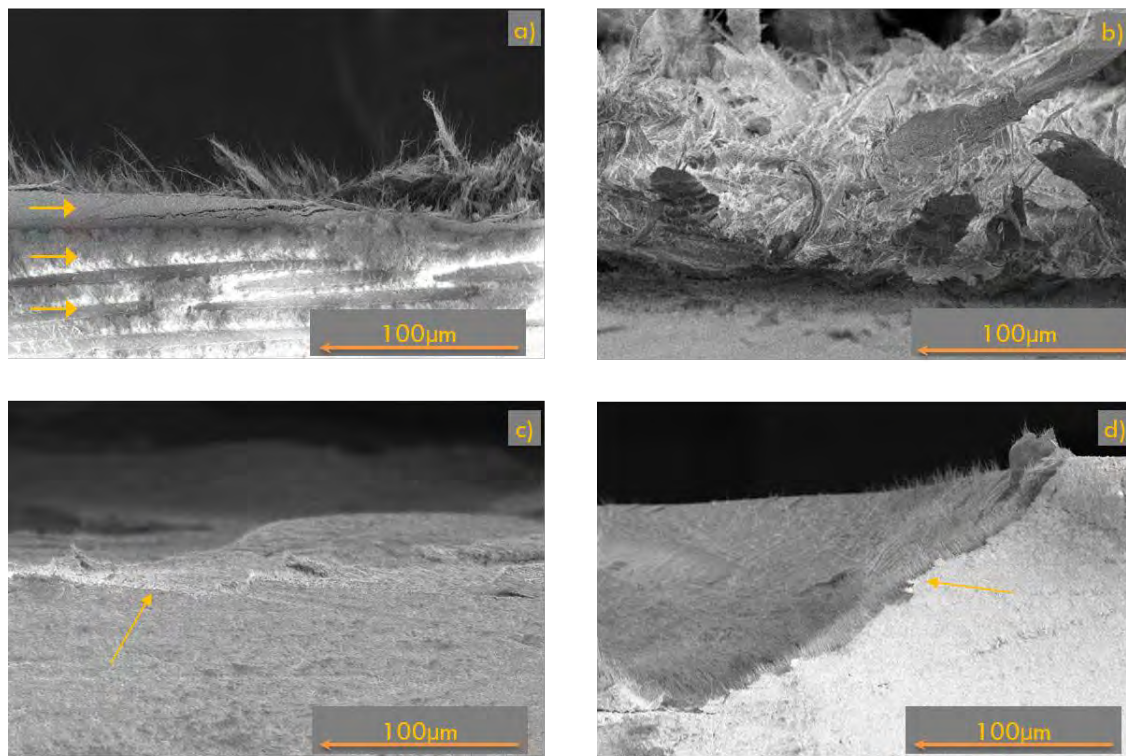


Figure 3.11. Micro scale SEM images of ‘D’ (a), ‘N’ (b), ‘A’ (c), and ‘P’ (d) interleave cases. Scale arrow denotes crack propagation direction.

SEM images shown in Figure 3.10 provide further insight into the micro characteristics of the interleaved fracture surfaces. It shows the cross section of both fracture surfaces at  $a_0$  for ‘D’ and ‘N’ cases. It is clear from Figure 3.10a-b that CNTs are present on both fracture surfaces which



confirms that delamination crack propagates through the SPS in both ‘D’ and ‘N’ interleave cases.

A closer look at the characteristic fracture surfaces in Figure 3.12 shows the differences in the CNT pull-out phenomena for the different interleaves, with longer and non-uniform pull-outs for dry and non-functionalized interleaves as in Figures 3.12a-d, and short regular pull-outs characterized by uniform lengths and more aligned CNTs, as in Figures 3.12c,f.

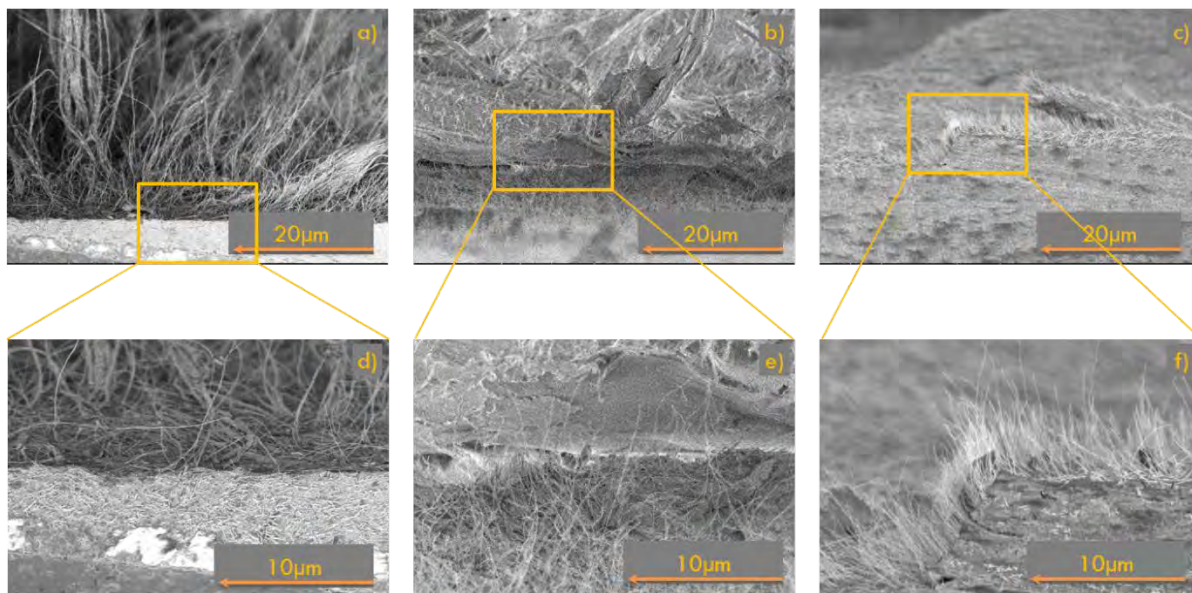


Figure 3.12. Approaching nano scale SEM of ‘D’ (a,d), ‘N’ (b,e), and ‘A’ (c,f) interleaves near crack initiation. Scale arrow denotes crack propagation direction.

From the conducted microscopy studies it is apparent that pre-infusing the SPS preform with low-viscosity epoxy resin and additional functionalization of the CNTs make a substantial effect on the fracture surface characteristics and delamination propagation path, which result in variations in the measured Mode I fracture toughness values. The use of pre-infused SPS introduces more variation in the delamination path which alternates between cohesive and adhesive fracture types. Even more, it can result in a complex delamination crack propagating outside of the interleaf and possibly penetrating into the adjacent composite ply, which results in the highest increase of the laminate fracture toughness. Functionalization of the CNTs results in a cleaner fracture surface with relatively regular, short and aligned CNT pull-outs.

Experimental results presented in this chapter show that the use of SPS interleaves pre-infused with a low viscosity epoxy resin before integrating it within the laminated composite makes strong positive effect on Mode I fracture toughness of CFRP laminates. The increase of  $G_{IC}$  values measures up to 105%. Surprisingly, both CNT functionalization methods used here did not show the anticipated significant additional  $G_{IC}$  increase; understanding the reason(s) for that warrants further studies. Particularly, the bulk properties of the non-functionalized and functionalized SPS composites should be characterized and compared in order to get more insight into the load transfer mechanisms between the CNTs and the matrix.

As evidenced by the much “smoother” load vs. displacement curves, the pre-infused SPS interleaves show better ability than the non-interleaved and dry SPS interleaved laminates to resist catastrophic failure. It is possible that this will also manifest in improved fatigue resistance, which may be another important subject of future studies.

Apart from the Mode I fracture toughness performance (which was in the focus of this study), the CNT SPS reinforcements provide high dimensional stability to the interleaves and structural joining elements. This feature may be particularly beneficial for interfaces and joints in high-precision devices and structures (particularly, miniature ones) which require very thin preforms with well-defined dimensions - the requirement that may be difficult to satisfy with traditional adhesives.

### 3.6. References

1. ASTM Standard, “Standard Test Method for Mode I Interlaminar Fracture Toughness of Unidirectional Fiber-Reinforced Polymer Matrix Composites”. ASTM, 2012.
2. Stevanovic, D.; Jar, P.-Y. B.; Kalyanasundaram, S.; Lowe, A. “On Crack-Initiation Conditions for Mode I and Mode II Delamination Testing of Composite Materials.” *Compos. Sci. Technol.* 2000, **60**, 1879-1887.
3. Szekrenyes, A. “Overview on the Experimental Investigation of the Fracture Toughness in Composite Materials.” *Dep. Appl. Mech.*, 2002, 1–19.
4. Brunner, A. J.; Blackman, B.R.K.; Davies, P. “A Status Report on Delamination Resistance Testing of Polymer–Matrix Composites.” *Eng. Fract. Mech.*, 2008, **75**, 2779-2794.
5. Hu, X.; Mai, Y. “Mode I Delamination of Fibre Bridging in Carbon Fiber Epoxy Composites With and Without PVAL Coating.” 1993, **46**, 147–156.

## **CHAPTER 4. CNT INTERLEAVING OF ADHESIVELY BONDED COMPOSITE JOINTS**

### **4.1. Introduction**

Failure of composite joints is typically associated with shearing stress within the joint. Basic shear strength of an adhesive is commonly determined with the use of a lap joint specimen. However, this test specimen configuration is non-symmetric, and such imbalance of the joint typically results in a transverse tensile loading component of the adhesive which adds to the primary shear loading component. A double strap (a.k.a. double-doubler) joint achieves a balanced structure and enables for the realization of a purer form of shear failure. Also, importantly, very high, though localized, transverse tensile (“peeling”) stress may be arising in the vicinity of each lap joint corner. That stress is commonly viewed as the primary cause of premature delamination-type failure of the joint. Double Cantilever Beam (DCB) Mode I fracture test is thought to closely mimic the peeling stress effect around the joint corners due to its principal driving force is same in both cases – high transverse tensile stress originated at the crack tip. The DCB specimen toughness improvement seen in the results of previous chapter suggests that modification of the adhesive layer of a lap joint with CNT shear-pressed sheet (SPS) interleaves may also offer a potential for improving the joint strength. However, even with evidence of CNT reinforcement improving Mode I fracture toughness, there is no guarantee of improvement in a practical joint structure due to the contribution of the other failure modes. Thus, actual lap joint fabrication and testing is necessary to validate the effect of CNT SPS interface reinforcement and possible strength enhancement. This chapter presents out initial exploration in this direction.

### **4.2. Experimental Joint Sample Preparation**

Two composite bonded lap joints were fabricated in order to test the influence of CNT SPS modified adhesive layer on the strength of the joint. As the objective of the study has been set to observe the strength enhancement of the CNT-modified bonding layer within the joint rather than the strength of the interface between the bonding layer and composite, SPSs was pre-infused with relatively low viscosity epoxy resin and then incorporated into a unidirectional prepreg ply layup and co-cured with them. SPSs were located in place where adhesive bonding layer would normally be located, between the cured composite adherends, and will be accordingly referred to as SPS bonding interlayer. Specimens cut from the layup possess the same geometry as lap joint and double strap joint. The co-curing eliminated the need to find a low viscosity resin (otherwise needed for the SPS pre-infusion). Both joint configurations were tested on an MTS 2000kN load cell with a 2000 psi hydraulic clamping force at a strain rate of 0.1 mm/min and a gauge length of 240 mm. Specimen width was approximately 22 mm. CNT alignment direction in the SPS is be parallel to the direction of loading.

#### **4.2.1. Single-Lap Joint Fabrication and Testing**

CNT SPSs were fabricated as described in Chapter 2 and are composed of ~1500  $\mu\text{m}$  long CNTs in a 25x25 mm array. SPSs were used as-produced, in a dry form. Test methods were followed the recommendations from [1, 2, 3], the specimen geometry incorporated tabs in order to

eliminate effects from grip misalignment observed in lap joint samples specified by the standards. Fabrication followed the process illustrated in Figure 4.1, beginning with a  $[0^\circ]_8$  layup of carbon fiber prepreg with the SPS placed between two 12  $\mu\text{m}$  thick pieces of Teflon film. The prepreg layup was cured in a vacuum bag layup under 45 psi pressure at 290°F for 2 hours. At which point the structure was removed and cuts were made to a point when the Teflon film was visible using a diamond blade circular table saw, allowing for tabs to be removed and producing a lap joint.

Four Single-lap joint (SLJ) specimens were tested without the SPS and are further referred to as “Baseline” (B) and three SLJ specimens referred to as “Dry” (D) were tested with the SPS along entire overlap region (where an adhesive layer would otherwise be present).

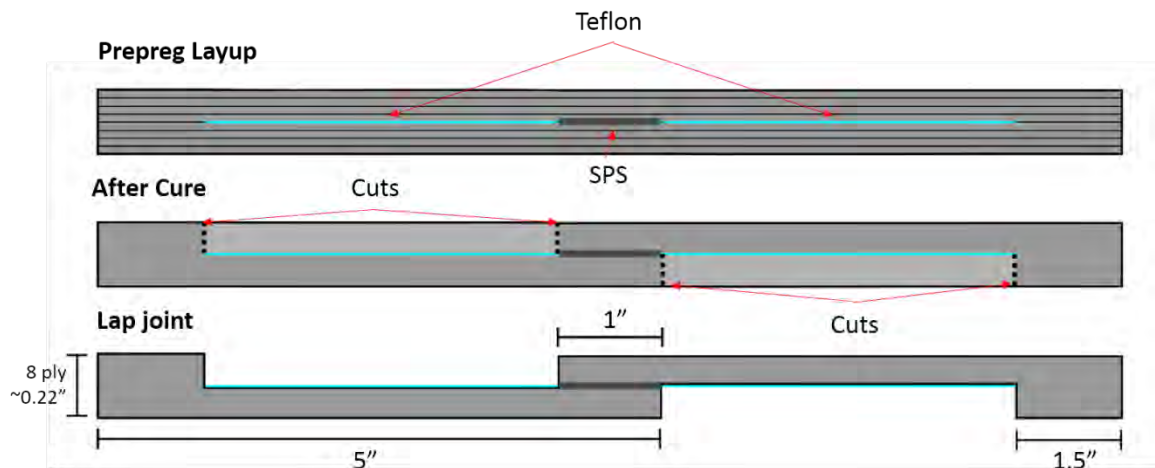


Figure 4.1. Single-lap joint fabrication illustration and specimen dimensions.

#### 4.2.2. Double-Strap Joint Fabrication and Testing

Double-strap joints (DSJ) were fabricated from unidirectional carbon fiber prepreg in a  $[0^\circ]_{16}$  lay-up as illustrated in Figure 4.2. Two straps were fabricated from four plies of the prepreg and two adherends were fabricated from 8 plies. A small portion of the blue protective film was then removed in order to place an 1 x 3 inch size SPS that contain  $\sim 500 \mu\text{m}$  long CNTs onto the tacky surface of the straps. The SPS preform was infused with Epotek 301-2 resin system. The resin infusion was performed after a 5-ply prepreg stack was assembled and the SPS was transferred to the top prepreg surface. At that point the resin was heated to 90°C in a microwave to decrease the viscosity to  $<65 \text{ cP}$  and spread in a thin layer over the SPS and prepreg surface. The 5-ply prepreg panel with attached infused SPS was then placed in vacuum at room temperature for 10-15 minutes to promote better resin infiltration into the SPS. After that excess resin was removed from the SPS and the remaining 5 prepreg plies were added on top. The laminate lay-up was allowed to rest for a period of 24 hours under a steel plate in order to allow the infused SPS to partially cure so as to maintain its shape during cure. The prepreg layup was cured in a vacuum bag layup under 45 psi pressure at 290°F for 2 hours. Specimens were cut using a wet tile saw with a diamond blade.

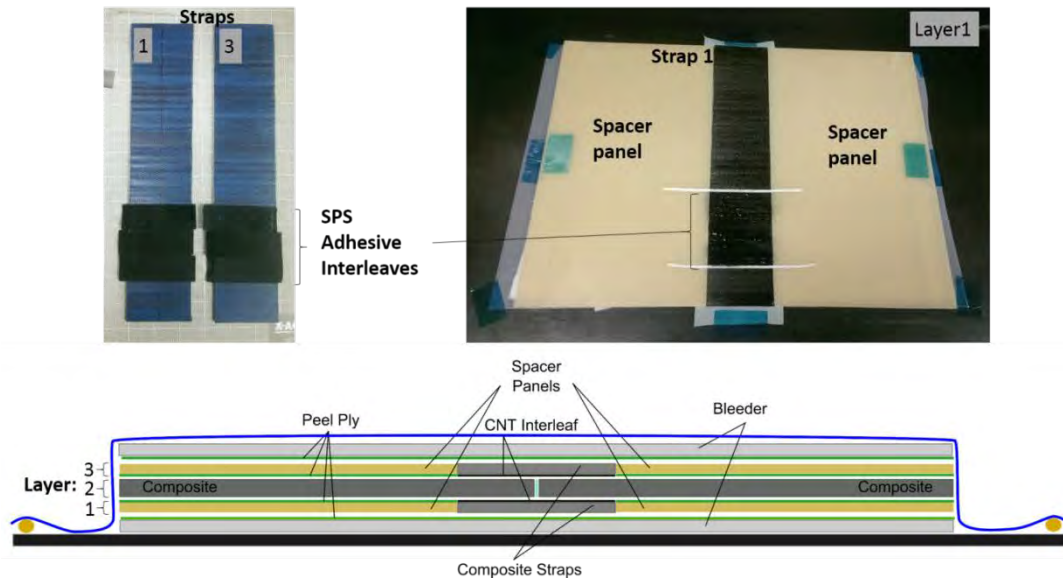


Figure 4.2. DSJ prepreg lay-up and fabrication.

Figure 4.3 shows the examples of the cured and cut DSJ. Edges of the joints were carefully filed down to create a flat surface while taking care not to damage the adherend at the end of the overlap corner line. Due to some shifting during cure and minor processing errors during the lay-up, some slight misalignment of the straps was possible, as is shown in Figure 4.3. This could cause premature failure of the joint. An attempt was made to mitigate the effect by filing the edges, however in most cases there was some misalignment up to 1 mm. On all but one specimen this appeared to have no effect as both straps failed at the same instant. Five “Baseline” (B) specimens, which contained no SPS at the bondline, and five “Infused” (I) specimens, which contained infused SPS between the straps and adherends, were fabricated and tested.

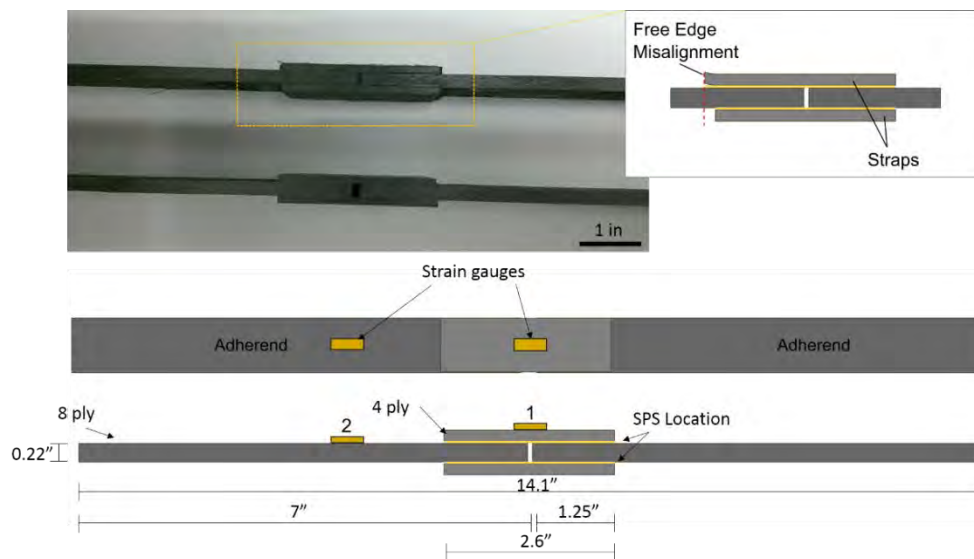


Figure 4.3. DSJ geometry and strain gauge locations.

Two Micro-Measurements 350 ohm strain gauges with a 2.1 gauge factor were mounted at the center of the DSJ specimens, one on the adherend and the other on the strap. Specimens were mounted in the test fixture as shown in Figure 4.4.

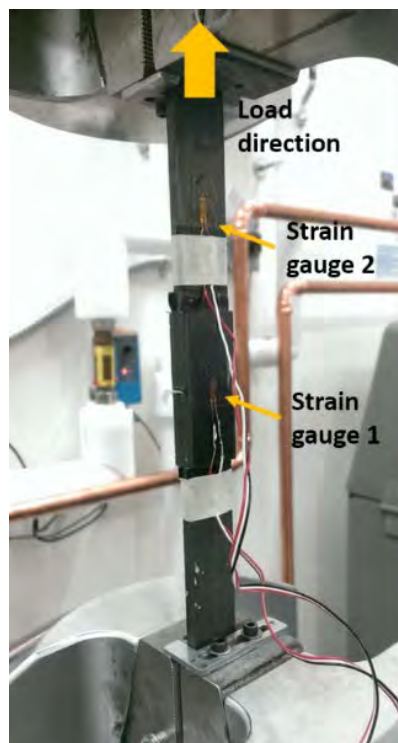


Figure 4.4. DSJ test set-up.

### 4.3. Experimental Results and Discussion

The principal test data for SLJ are summarized in Table 4.1. It appears that there is a slight reduction in failure loads and failure displacements as the result of SPS incorporation at the bondline. This result is consistent with what has been reported in Chapter 3 from DCB testing (i.e., a reduction in interlaminar fracture toughness for the same kind of interleaf). This result may also imply that Mode I delamination, or peel-type failure, is the dominant failure mode in the SLJ case. Evidences of same kind correspondence between the DCB and SLJ sample behaviors can be also found in the literature, see [4] for example. It was anticipated that the SPS incorporation should correlate most evidently between “initial” fracture toughness change in the DCB test and the failure load change in the SLJ test, because the joint fails instantaneously (which is not of course observed in the DCB tests) and the joint failure therefore load does not depend on the “propagation” fracture toughness of the DCB sample. Indeed, according to Table 3.1, the Dry SPS interleaf incorporation in the DCB reduced initial fracture toughness by ~5%, while as Table 4.1 shows, incorporation of the same type SPS in the SLJ reduced its failure load by ~11%. This difference suggests that in SLJ case, the contribution of the other failure modes is also significant.



Table 4.1. SLJ test data at point of failure.

	<b>Displacement (mm)</b>	<b>Load (kN)</b>
<b>Baseline</b>	<b>0.435 ± 0.074</b>	<b>9.538 ± 0.847</b>
<b>Dry SPS</b>	<b>0.376 ± 0.012</b>	<b>8.474 ± 0.308</b>

The principal test data for DSJ case are summarized in Table 4.2. Overall, the effect of Infused SPS is rather marginal. The joint failure load increased by 4.6% and the joint failure strain measured on the grips increased by 14%. At the same time, the strains at failure point measured on the adherend and strap surfaces both decreased - by 7.5% and 7.8%, respectively. The latter result is very interesting by itself – it implies that under somewhat higher load level the composite adherends and straps are loaded less within the DSJ that has SPS reinforced interleaves at the bondlines (as illustrated in Figure 4.3). The only explanation for that may be that the SPS nanocomposite interleaves redirect significant part of the load onto them in the most critical region, e.g., the joint bondline. This stress re-distribution results in the joint failure load and failure strain increases. In other words, the joint bondline reinforcement with CNT SPS nanocomposite makes certain positive effect.

This joint configuration should fail in a purer form of shear failure, which would be mainly related to the Mode II fracture toughness (that was not studied here). In agreement with this presumption, a rather small, 4.6%, DSJ failure load improvement shows little correlation with the Mode I DCB test results. Indeed, the Non-functionalized sample case in Table 3.1 (which is equivalent to the Infused DSJ case) shows much higher, 76%, “initial”  $G_{IC}$  improvement over the Baseline sample in DCB testing. Therefore, contrasting with the SLJ case, this confirms that failure of the DSJs is not dominantly governed by Mode I peel stresses, and that the effect of CNT SPS on Mode II interlaminar fracture toughness is expected to be much lower than that on Mode I.

Table 4.2. Double strap joint test data at point of failure.

	<b>Peak Load (kN)</b>	<b>Grip Displacement (mm)</b>	<b>Grip Strain %</b>	<b>Peak Adherend Strain %</b>	<b>Peak Strap Strain %</b>
<b>Baseline</b>	<b>32.6 ± 1.37</b>	<b>0.990 ± 0.038</b>	<b>0.420 ± 0.011</b>	<b>0.306 ± 0.056</b>	<b>0.204 ± 0.061</b>
<b>Infused</b>	<b>34.1 ± 1.79</b>	<b>1.135 ± 0.068</b>	<b>0.473 ± 0.028</b>	<b>0.283 ± 0.004</b>	<b>0.188 ± 0.025</b>

We can conclude from this preliminary study of the CNT SPS effect on the strength of lap joints that significant improvement in Mode I fracture toughness observed in respective DCB tests (see Chapter 3) does not translate nearly as well as expected into the lap joint strength. Since the peel stress seems to control the SLJ failure initiation and, at the same time, the performed tests show instantaneous joint failure, the “propagation”  $G_{IC}$  values are not relevant at all. In the case of DSJ, shear stress rather than peel one seems to be dominate the joint strength; this makes no correlation between that joint type strength and the DCB test data. Mode II interlaminar fracture tests are required to establish such a correlation. On the positive side, the joint test results reveal

that infused CNT SPS interleave incorporated within DSJ takes significant portion of load which increases the failure load and failure strain values for the joint. All these effects deserve further comprehensive studies.

#### **4.4. References**

1. ASTM Standard Test Method for Determining Strength of Adhesively Bonded Rigid Plastic Lap-Shear Joints in Shear by Tension Loading 1. 2013, **01**, 8–10.
2. ASTM Standard Test Method for Lap Shear Adhesion for Fiber Reinforced Plastic (FRP). 2013, **01**, 1–2.
3. ASTM Standard Guide for Use of Adhesive-Bonded Single Lap-Joint Specimen Test. 2013, **01**, 1–6.
4. Matthews, F. L.; Kilty, P. F.; Godwin, E. W. “A Review of the Strength of Joints in Fibre-Reinforced Plastics. Part 2. Adhesively Bonded Joints.” *Composites*, 1982, **13**, 29-37.



## **CHAPTER 5. CARBON NANOTUBE DRAWN SHEET AND SHEAR-PRESSED SHEET PIEZORESISTIVE STRAIN SENSORS**

Carbon nanotubes (CNTs) have a unique set of properties that may be used for the production of a next generation structural health monitoring materials. This research introduces a novel CNT based material for potential strain sensing applications. The aligned sheet of interconnected CNTs was drawn from a chemical vapor deposition (CVD) grown CNT array and then bonded to the surface of glass fiber/epoxy laminates. Various types of mechanical tests were conducted, accompanied by real-time electrical data acquisition, in order to evaluate the electro-mechanical behavior of the developed sensing material. Specimens were loaded in the longitudinal and transverse CNT sheet orientations to investigate the anisotropy of the piezoresistive effect. The CNT sheets exhibited good sensing stability, linearity, sensitivity and repeatability within a practical strain range; which are crucial sensor features for health monitoring. It was also demonstrated that the CNT orientation in the sheet had a dramatic effect on the sensitivity, thus validating the usefulness of this sensing material for directional strain/damage monitoring. Finally, pre-straining of the CNT sheet sensors was conducted to further enhance the linearity of electro-mechanical response and long-term stability of the proposed strain sensing under cyclic loading.

### **5.1. Introduction**

With the application of advanced composites rapidly increasing into the aerospace and transportation industries, real time structural health monitoring (SHM) systems are attracting attention in the composites research community. The intrinsic properties of CNTs make them desirable for application in SHM and advanced material fields [1]. Among those various attractive properties, their piezoresistive nature makes CNTs good candidates for strain and damage sensing applications. In recent years, many researchers have investigated a diverse variety of CNT-based sensing materials with different CNT architectures, including pristine CNTs assemblies (pure CNT yarns [2-6] and buckypaper [7-10]) and CNT/polymer hybrid composites with random or aligned CNT dispersions (CNT fibers [11-13], films [14-21] and bulk composites [22-30]). However, the existing CNT-based strain sensing materials suffer from different issues which often limit their further development into actual sensors for practical applications. For example, CNT yarn sensors show excellent repeatable and stable piezoresistive behavior, but the so-called “gauge factor” (GF) values are typically low (as reported in [3] for example, they are around 0.5). Buckypaper CNT sensors have low strength and usually fracture at very low strain levels (though good sensitivity had been achieved in [7]). The greater sensitivity and higher mechanical strength of CNT/polymer nanocomposites shown in many research publications is encouraging. However, the problem of initial electrical resistance drifting under zero loading may limit their use as real sensors. These type of material have also exhibited electrical resistance hysteresis during cyclic loading [28, 30].

The CNTs can not only serve as sensor elements, but also function as a reinforcing constituent within composites, thus opening new avenues for multi-functional applications. A highly desirable feature of advanced CNT-reinforced composite materials is controlled alignment of the CNTs inside the host polymer matrix, which naturally improves the mechanical properties of composite in the alignment direction [31]. In addition, many researchers have claimed that good

alignment of CNT assemblies is beneficial for increasing the piezoresistive effect. For instance, CNTs in polysulfone matrix were aligned by an electrical field, which resulted in improved electrical and piezoresistive sensing capabilities of the composite films [32]. In [33] it was predicted that CNT alignment in the direction of the applied strain would increase the piezoresistive sensitivity of the composite.

The ultimate objective of our research presented in this chapter was to develop a novel type of CNT-based piezoresistive strain sensors which possess higher sensitivity than the earlier reported ones and, at the same time, are repeatable, robust, easy to make, and cost effective. It is envisioned that this type of CNT sensors can be either surface mounted or embedded into composites.

As a first step toward achieving these objectives, we introduce here a novel aligned CNT strain sensing patch (SSP) that can be bonded to the surface of traditional composites. Continuous aligned carbon nanotube sheets are pulled directly from “drawable” CVD grown multi-walled CNT arrays. Then they are transferred onto fiberglass/epoxy prepregs and cured altogether with the host laminate, thus becoming an integral part of composite structure capable of *in situ* health monitoring. Notably, the CNT sheets are so thin (in the range of micrometers) that they make no disruptive effect of the structural performance of a host composite.

## 5.2. Materials and Fabrication

Drawable MWCNT arrays were synthesized through a chlorine-assisted low pressure CVD method; the arrays typically consist of individual CNTs with 25 - 40 nm diameter and ~1 mm length, as described in [34]. Glass fiber/epoxy prepreg (Fibre Glast 7781 E-glass prepreg) was used to fabricate the CNT SSP. Through the use of prepreg, consistent resin content and repeatable properties should be attained. The data sheet for the cured resin used with the chosen prepreg gives a tensile modulus of 3.03 GPa and elongation at break of 4.0%. This particular prepreg was chosen as the base material for CNT SSP fabrication because the mechanical properties of the cured prepreg composites are similar to mechanical properties of the host composite. The prepreg is easy to handle, it provides structural stability to an otherwise thin and fragile CNT sheet, and has a sticky surface which is important for fixing the CNT sheet in place during processing.

To fabricate the CNT SSP, the aligned CNT sheet was directly drawn out from the CNT array, and then transferred to a small prepreg with dimensions of 50.8 mm × 19.05 mm (2 inches × 0.75 inches). SSP were produced in which (a) the CNT sheet draw direction was aligned with the loading direction (“parallel specimens”) and (b) the CNT sheet draw direction was perpendicular to the loading direction (“perpendicular specimens”). Only a few micrograms of CNTs are needed to produce a single CNT SSP, making the material costs for fabrication very economical. The CNT SSP was attached to the surface of pre-fabricated fiber glass composite (G10/FR4 fiberglass laminate from American Epoxy and Metal Inc.) coupons. The coupons had dimensions of 300 mm × 30 mm × 6.35 mm (L × W × T) and were tabbed at the ends with 2 mm thick G10/FR4 fiberglass sheets with a taper angle of 20°. The sample and tab dimensions were selected to satisfy ASTM standard D3039/D3039M - 08 - Tensile Properties of Polymer Matrix Composite Materials [35].

A complete work flow is presented in Figure 5.1. The fabrication procedure of integrated specimens following steps of CNT array deposition and vacuum bagged SSP curing is illustrated in Figure 5.1. Fine copper foils were cut into uniform dimensions (20 mm  $\times$  10 mm) and precisely positioned on the surface of the host composite coupons and fixed with high temperature tape. Next, the CNT SSP was applied with the CNT sheet facing the composite coupon surface and the two ends contacting the copper foil electrodes. A nylon peel ply and then breather cloth was placed on the outer surface of the SSP. The assembly was vacuum bagged and the SSP was cured at 154°C for ~1 hour in a platen hot-press under atmospheric pressure only.

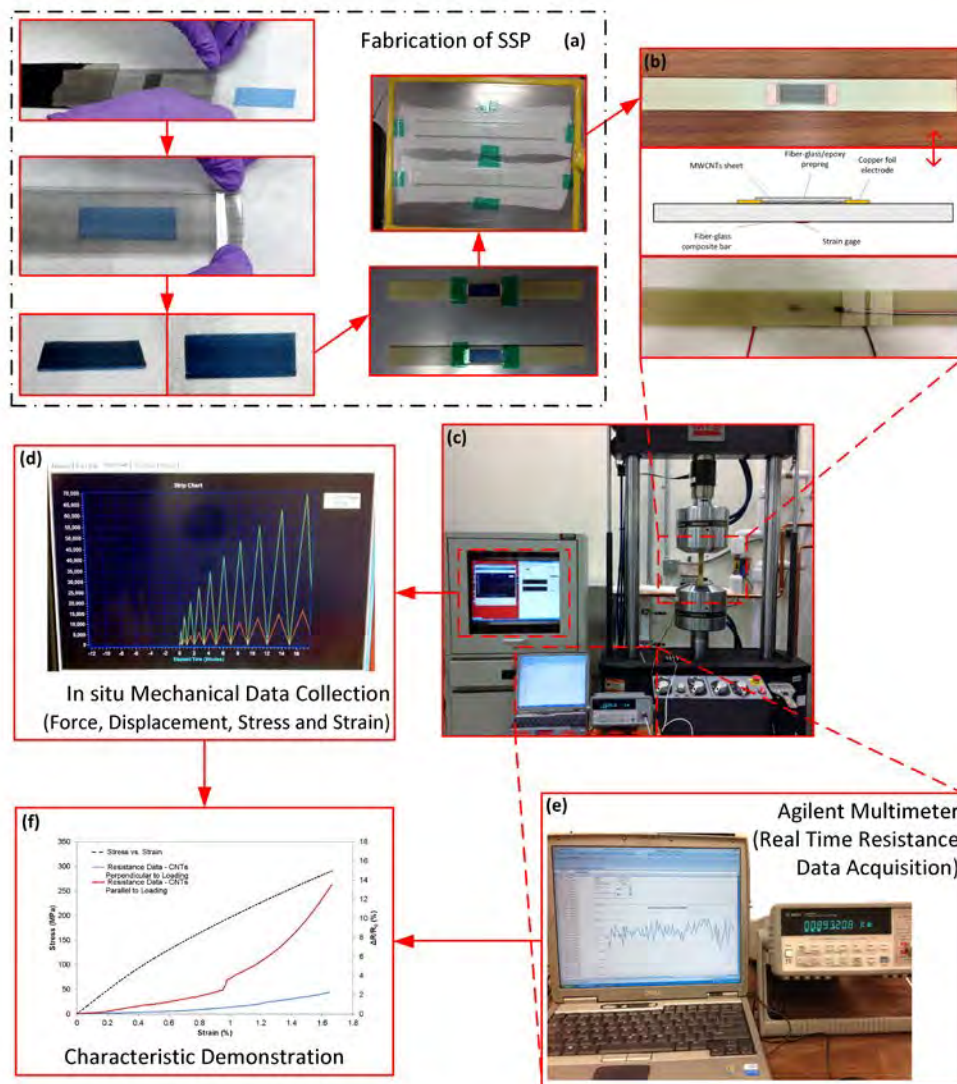


Figure 5.1. Diagram of experimental work flow; details in the text.

Figure 5.1b shows schematic and close-up of SSP with both surfaces showing the components structure. Two wires of the same length (~1 m) were soldered onto the surface of the two copper

foil electrodes at the ends of the SSP to achieve good electrical contact between the sensor and the measurement device. In order to get independent real-time and accurate strain measurement comparison with the CNT SSP strain monitoring data, an external commercial metal foil strain gauge (Vishay Micro-Measurements 250LW) was mounted on the opposite face of the host composite. As further illustrated in Figures 5.1c, 5.1d, 5.1e and 5.1f, all the mechanical data and real-time electrical resistance response were recorded simultaneously and plotted to demonstrate the piezoresistive behavior.

### 5.3. Characterization and Testing

In order to evaluate the sensing performance of the CNT SSP, different types of experiments were performed using an MTS Landmark servo hydraulic 250 kN test system including: (1) monotonic tensile tests, (2) constant strain rate cyclic tensile tests, (3) 1000 cycle fatigue tests and (4) load controlled incremental loading-unloading tensile tests. The typical experimental set-up and mounting of the test coupon on the mechanical testing equipment is shown in Figure 5.2.

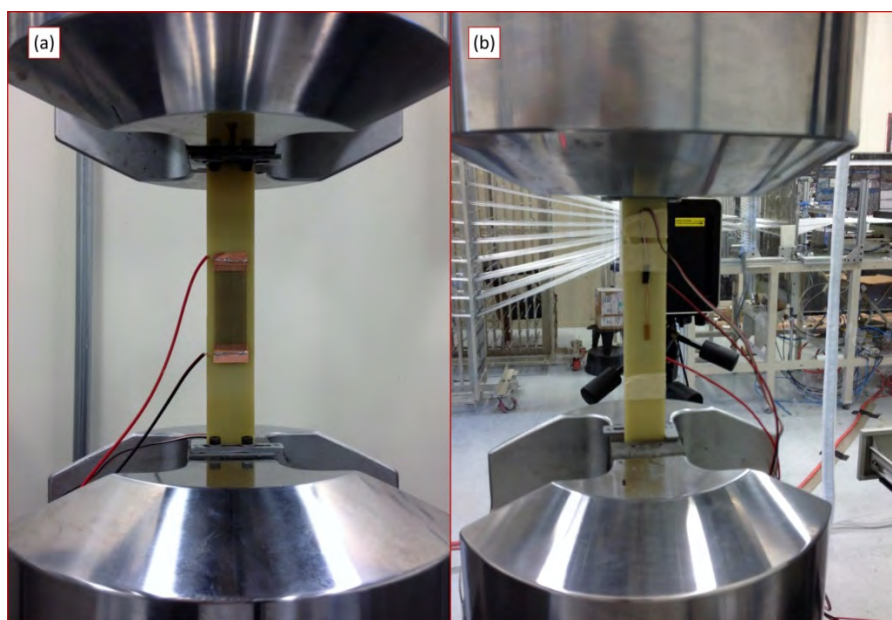


Figure 5.2. Typical mechanical tensile test set-up: front surface with a CNT SSP (a) and back surface with a metal foil strain gauge (b).

In all types of tensile tests, the electrical resistance of the CNT SSP was recorded simultaneously by an Agilent 34420A multimeter at a frequency of 10 Hz. The resistance measurements were conducted by using a four-probe method along the longitudinal direction of the composite coupon to eliminate the influence of wiring resistance. Generally, the following data were all simultaneously recorded: (1) force and displacement from the testing machine, (2) stress and strain from the external strain gauge (see Figure 5.1d) and (3) electrical resistance from the multimeter (see Figure 5.1e). Monotonic tensile tests were performed with a fixed displacement speed of 1.5 mm/min. In total, two groups of specimens, three “parallel” and three “perpendicular” were monotonically strained to failure to ensure that all of them had similar piezoresistive behavior. For the case of the incremental tensile tests, the specimens were loaded

and unloaded at the same rate with progressively increasing peak values of cyclic loading with a step value of 7 kN until coupon failure. A total of six specimens (three parallel and three perpendicular ones) were tested in the defined progressive damage accumulation loading – unloading cycles. At the end of each cycle, the specimens were unloaded to zero loading state of the machine, in order to monitor the induced damage via residual strain measurements of the coupon and corresponding irreversible resistance change of the CNT SSP. All the mechanical tests were conducted in a controlled laboratory environment. The temperature vs. resistance behavior was investigated while the specimen was kept in a Ransco RTH-200-S thermal chamber.

#### 5.4. Validation of CNT SSP Stability

One of the basic requirements for any sensor is that it should be stable during use. The electrical resistance variation of the fabricated CNT SSPs has been measured in this study over a period of multiple days, under room temperature, ambient atmosphere, without any mechanical load applied, as shown in Figure 5.3a. It can be seen that the electrical resistance readings fluctuate in very small amplitude (within  $\sim 0.1\%$  of the initial reading over 120 hours; CV% of 0.031% as calculated). This result indicates that without mechanical loading, the CNT SSP has excellent long-term electrical resistance stability. This is probably due to the intrinsic physical structure of the CNT sheet in which  $\sim 1$  mm long CNTs have a huge density of initial mutual contacts and that does not vary considerably if the environmental conditions are kept constant.

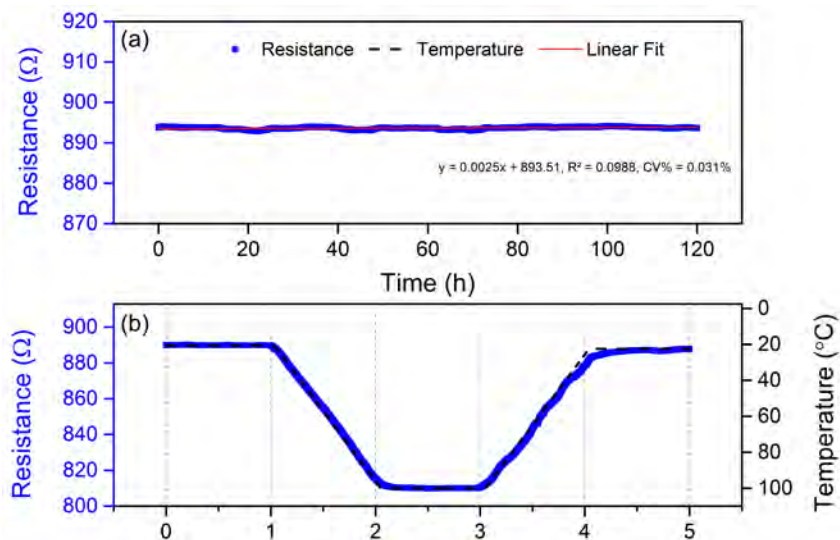


Figure 5.3. (a) Long term intrinsic electrical resistance stability validation: the resistance of the SSP was measured under zero load at room temperature for time period over 120 hours and showed high stability (a). Electrical resistance varied in accord with the temperature variation in the range of 22 - 100°C, and was able to restore its room temperature value after the CNT SSP was exposed to 100°C temperature for 1 hour (b).

As some literature data show, CNT/polymer composites suffer from electrical resistance drifting over time with no applied mechanical load [15]; this effect may limit their capability to function

as sensing materials in practical applications. The problem has been traced in [15] to the defects in CNT wall structures and the localized heating caused by electrical current concentration. In contrast to the CNT sensor materials with low CNT volume content, the relatively high CNT volume content sensor materials studied here have much greater initial density of mutual CNT contacts and, respectively, shows much lower sensitivity to defects possessed by individual CNTs. This effectively eliminates the undesired localized heating effect by building up alternative electrical pathways.

The electrical resistance of CNT SSP showed good stability during a five hour dynamic thermal test under a zero mechanical load condition, as shown in Figure 5.3b. The sensor was kept in the thermal chamber, and the electrical resistance was measured while the sensor was under a predetermined heating and cooling program. First, the sample was kept at room temperature for one hour. Then the chamber temperature was increased linearly from room temperature to 100°C (approximate max use temperature for the resin system) during a one hour time period. After that the temperature was kept constant at 100 °C for one hour. Finally, the sample was cooled down to room temperature over the course of an hour and held at room temperature for one more hour. It was observed that the electrical resistance of the CNT SSP remained practically constant during all time periods when temperature was kept constant, which indicates its electrical resistance stability for any temperature within this range. It is in a good agreement with previous experimental results for highly conductive CNT sensors, e.g. reported good stability of electrical resistance for CNT yarn sensors during 100 minutes of measurements at -196°C, 25°C and 110°C temperatures [3]. Also importantly, as seen in Figure 5.3b, the electrical resistance increased in the same linear fashion during the linear cooling stage. Overall, Figure 5.3b shows that the variations of the temperature profile and the electrical resistance profile match with each other, thus displaying that the electrical resistance depends linearly on the temperature change. Similarly, a linear thermal piezoresistive behavior was observed in other long nanotube assemblies with numerous inter-nanotube contacts, e.g. CVD grown pure MWCNT forest [36], MWCNT sheets [37] and aligned MWCNT papers [38]. The variable range hopping mechanism has been used to explain the linear thermal-electrical resistivity behavior [39]. The electrons would more likely hop across the highly interconnected nanotube network instead of via tunneling. Therefore, it is reasonable to expect this quasi-linear decrease of relative electrical resistance change corresponding to the temperature increase in the range tested.

The samples tested here showed an overall consistent and reversible electrical resistance vs. temperature behavior, thus demonstrating that the CNT SSP is able to function as a thermostable sensor within the range of temperatures studied here. While it was already suggested in other works that the long CNT assemblies have the potential to function as thermal sensors [36-38], our present results show that thin sheets of aligned CNTs in strain sensing patches may be able to serve the same purpose.

## **5.5. Sensitivity and Linearity of CNT SSP Electromechanical Behavior**

In order to investigate the piezoresistive response of the CNT SSP, the electrical resistance of the sensors was measured *in situ* while the sensors were mechanically strained in the axial direction of the coupon. Due to the superior electrical conductivity in the CNT longitudinal direction, the “parallel” SSPs have much lower electrical resistance (800-1000 Ohm) values than the



“perpendicular” ones (50-60 kOhm), as measured in our work. The typical mechanical tensile stress vs. strain curve and normalized resistance change  $\Delta R/R_0$ , where  $\Delta R$  is the real-time resistance minus original resistance  $R_0$  before straining of the SSPs as a function of strain are plotted altogether in Figure 5.4.

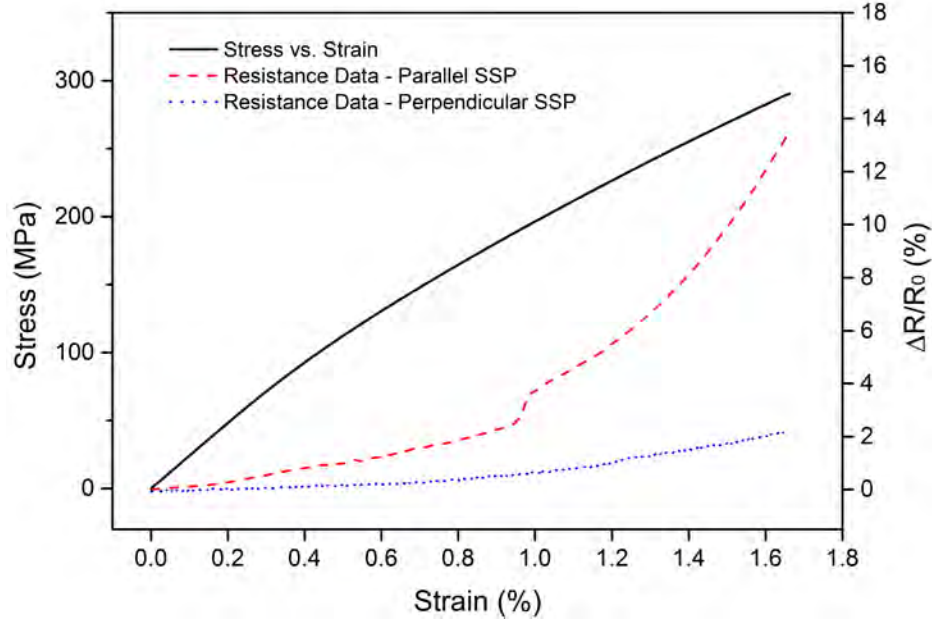


Figure 5.4. The stress - strain curve from monotonic tensile test and the normalized resistance change ( $\Delta R/R_0$ ) vs. strain ( $\epsilon$ ) curves for “parallel” and “perpendicular” SSPs.

The parallel SSP showed close to linear response of electrical resistance change vs. strain at lower strain levels (0 - 0.8%). Then, an abrupt change in  $\Delta R/R_0$  curve was observed around the strain of  $\sim 0.9\%$  in all the parallel specimens tested; the curve becomes non-linear and with a steeper slope. We can hypothesize that this might be due to the initiation of nano- and micro-cracking within the SSP intrinsic structure. The perpendicular sensors showed a nearly linear piezoresistive response with increasing strain overall; however, a change in the curve slope to a higher one is seen in the higher strain range, indicating an internal structure change of that SSP. For the purpose of strain sensing, a high sensitivity to applied strain is desirable for practical applications. The sensitivity is generally estimated by “gauge factor” (GF), which relates the normalized resistance change ( $\Delta R/R_0$ ) to the applied strain ( $\epsilon$ ) through the following equation:

$$GF = (\Delta R/R_0)/\epsilon \quad (5.1)$$

The GF is the slope of the coupled  $\Delta R/R_0$  and  $\epsilon$  curve. As shown in Figure 5.4, the parallel SSP has much higher GF which would be more beneficial for strain sensing.

Much research has been done on CNT dispersed nanocomposites with various types of polymer matrix. However, our SSP made with aligned CNT sheet is unique material for piezoresistive strain sensing. The CNT sheet consists of long nanotubes, forming a locally dense network of bundle-to-bundle connections or contacts as in [17, 39] rather than being arranged in an end-to-



end configuration or crossing at single junctions. Unlike most sensors made with short CNTs, long CNTs used here form numerous direct contacts with their neighbors where nanotube surfaces touch each other with either no separation or sufficiently small distance in-between.

Generally, as assessed in the literature, the piezoresistive behavior of CNT strain sensing materials can be mainly attributed to three aspects: (1) the intrinsic piezoresistivity of individual CNTs due to the energy bandgaps change in response to external strain; (2) change of contacting inter-nanotube electrical resistance, e.g., increase/decrease of the contact areas between CNTs; and (3) tunneling resistance change between neighboring CNTs due to inter-tube distance change [25, 40, 41]. Numerous electrical conductive pathways in the bundled CNT drawn sheet structure give the strain sensing material studied here very high electrical conductivity. The resistance between adjacent CNTs which are in direct contact, is by orders of magnitude lower than that between separated CNTs which can only conduct electric current through “tunneling” mechanism. In a parallel electrical circuit that contains both low resistance (bundled and numerous directly contacting CNTs) and high resistance (CNTs separated by a tunneling distance) resistors, the circuit’s overall resistance will be determined almost entirely by the low resistance elements. As a result, the change in resistance for our specimens is much more likely related to the piezoresistive behavior of individual nanotubes and the variations of direct CNT contacts.

For the parallel SSPs, at low strains (0-0.8%), the specimens exhibited a quasi-linear piezoresistive curve, with a lower GF compared to that seen for the higher levels of strain. It was also observed in all three specimens that a characteristic abrupt jump in the resistance and, respectively, abrupt increase in the GF occurred at around 0.8% strain. As suggested in [25], with the increase of strain value, the formation of nano-cracks was likely initiated in the epoxy matrix system of SSP. There would likely be a non-uniform stress distribution around CNTs in the epoxy matrix, leading to the onset of random nano-cracking in SSP at relatively low strain level [25]. At higher strain levels ( $\epsilon > 0.8\%$ ), the direct CNT contact network would be more significantly disrupted, possibly causing the de-bundling or fracture of a small fraction of CNTs which are located in the vicinity of the advancing cracks. This hypothesis is supported by the results seen in the incremental tensile tests discussed in the next section.

For perpendicular SSPs, the orientation of CNTs is largely normal to the loading direction. As a result, the fraction of CNTs being strained along their length is much lower and thus the piezoresistive response under strain is much weaker. As the strain is increased and nano-cracks are originated, the CNT network gets also affected (though in a more moderate way) showing no jump in the electrical resistance change. The whole system of CNTs may have been better preserved, possibly due to the fact that the CNT orientation would have been in the same direction as the developing nano-cracks.

Due to a good alignment of CNTs in the sheet, the parallel specimens have much higher sensitivity than the perpendicular ones. The GF of typical parallel SSPs are largely in the range of 1-8 while the perpendicular SSPs have their GF between 0.3-1.3, as seen in Figure 5.5.

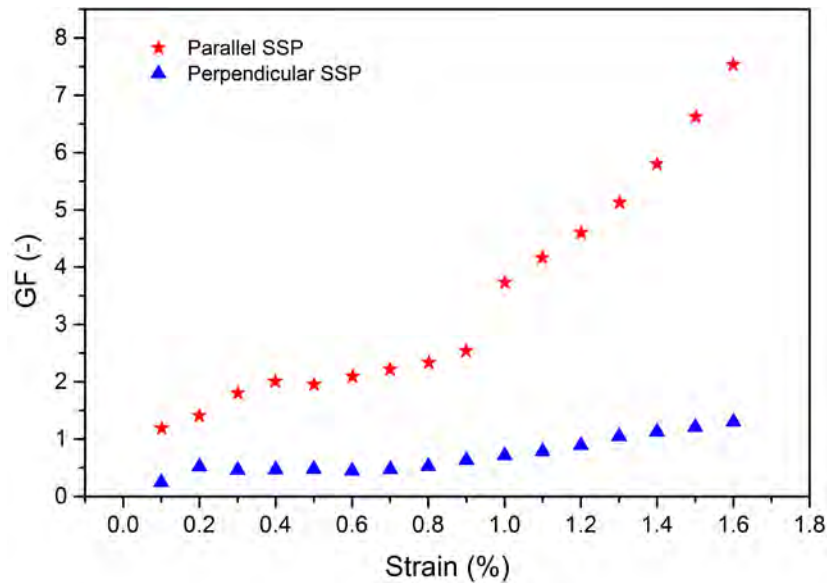


Figure 5.5. Gauge Factor of parallel and perpendicular SSPs at different strain levels in the monotonic tensile test with the sample being loaded to failure.

## 5.6. Cyclic Uniaxial Tensile Test

The quasi-static tensile tests discussed above showed relatively high GF. However, many CNT based strain sensing elements have shown that their behavior changes after repeated loading - unloading cycles. To study this effect, cyclic tensile tests were conducted to determine whether the piezoresistive behavior of this sensing material is maintained during multiple loading cycles. Figure 5.6a shows the piezoresistive responses of the parallel and perpendicular CNTs SSPs under cyclic loading. Both types of the sensors were strained to 0.8% and then unloaded back to zero strain for 10 cycles in total. The composite coupons were cyclically loaded at a rate of 2 cycles per minute.

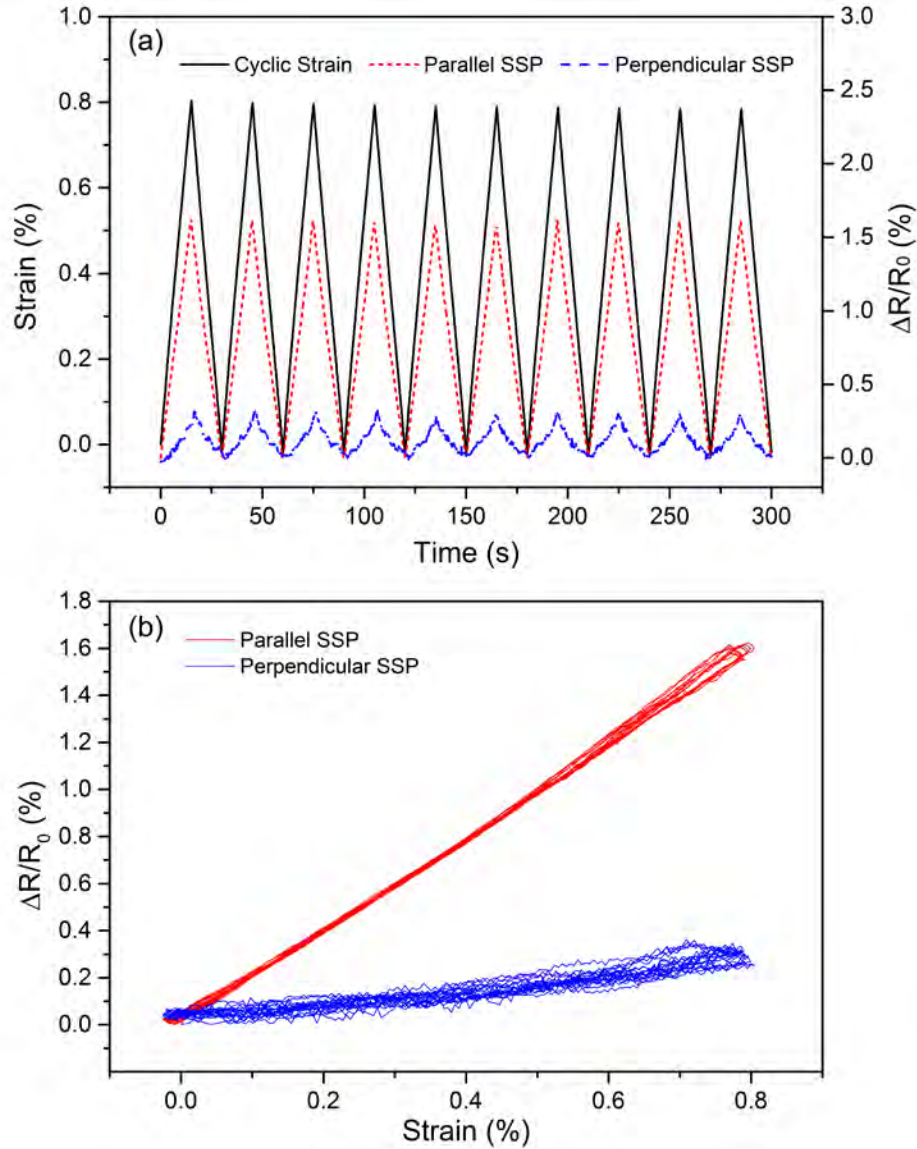


Figure 5.6. Cyclic tensile test: normalized electrical resistance change of parallel and perpendicular SSPs versus time in response to 10 cycles of loading – unloading with 0.8% maximum strain (a); hysteresis behavior of parallel and perpendicular SSPs (b).

The normalized electrical resistance change showed nearly-linear response to the cyclic strain variation; this response was maintained for all cycles without any significant resistance drifting. As indicated by the results in Figure 5.6a, in the strain range of 0 - 0.8% the linear piezoresistivity was preserved for both the parallel and perpendicular cases of CNT SSPs after multiple cycles of loading and unloading, showing no obvious hysteresis over multiple cycles which is seen in Figure 5.6b. Based on the distinct behaviors of SSP with two different CNTs orientations, the aligned CNT sheet strain sensing materials may be utilized to not only detect the strain that the underlying structure is undergoing, but also identify the principal direction from which the external load is applied.

## 5.7. Exploration of a Damage Sensing Potential

Load-controlled incremental tensile testing was used to further assess the potential of the SSPs to sense damage. The incremental tensile loading step was approximately 7 kN. The response of parallel and perpendicular SSPs to the defined incremental mechanical loading-unloading procedure is seen in Figure 5.7. In this figure, the applied stress and strain, as well as the electrical resistance change of two types of SSPs, are all plotted vs. time in order to analyze the corresponding piezoresistive behavior and also the damage detection capability of the SSPs with both parallel and perpendicular CNTs orientations. The test samples were unloaded to zero after each cycle. A residual strain and irreversible  $\Delta R/R_0$  of both parallel and perpendicular SSPs appeared for higher stress cycles.

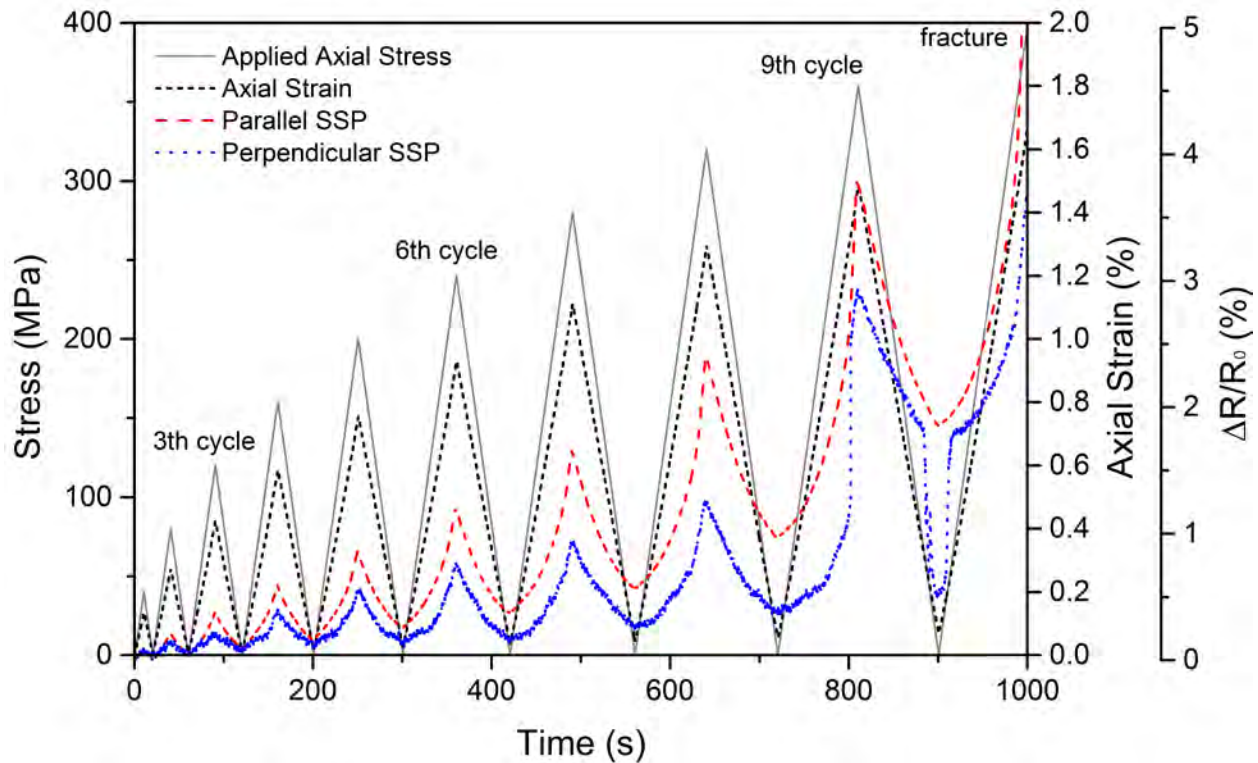


Figure 5.7. The real-time electrical resistance variation of parallel and perpendicular SSPs as well as stress/strain data corresponding to the progressively increasing load with 7 kN increment for each cycle until ultimate failure.

As seen in Figure 5.7, after the fourth loading cycle some residual strain in the test coupon was present when the specimen was unloaded to zero. The residual strain increased with each subsequent loading cycle. A similar behavior was noticed for the case of electrical resistance change of the SSPs with both CNTs orientations. After the fourth loading cycle, a distinct irreversible resistance change was present after the specimens were unloaded. This is in correspondence with the emerging residual strain data as recorded by the conventional strain gauge. This result indicates the potential for the SSPs to perform damage sensing.

Figure 5.8 further shows the developing residual strain in the host composite after each cycle of loading-unloading with the corresponding irreversible resistance change of CNT SSPs. The irreversible electrical resistance change of parallel sensors can be correlated with the residual strain progression during the first six cycles, and it deviates substantially afterwards. For the perpendicular SSPs, the irreversible resistance change curve follows, for its most part, the residual strain variations through the loading – unloading cycles.

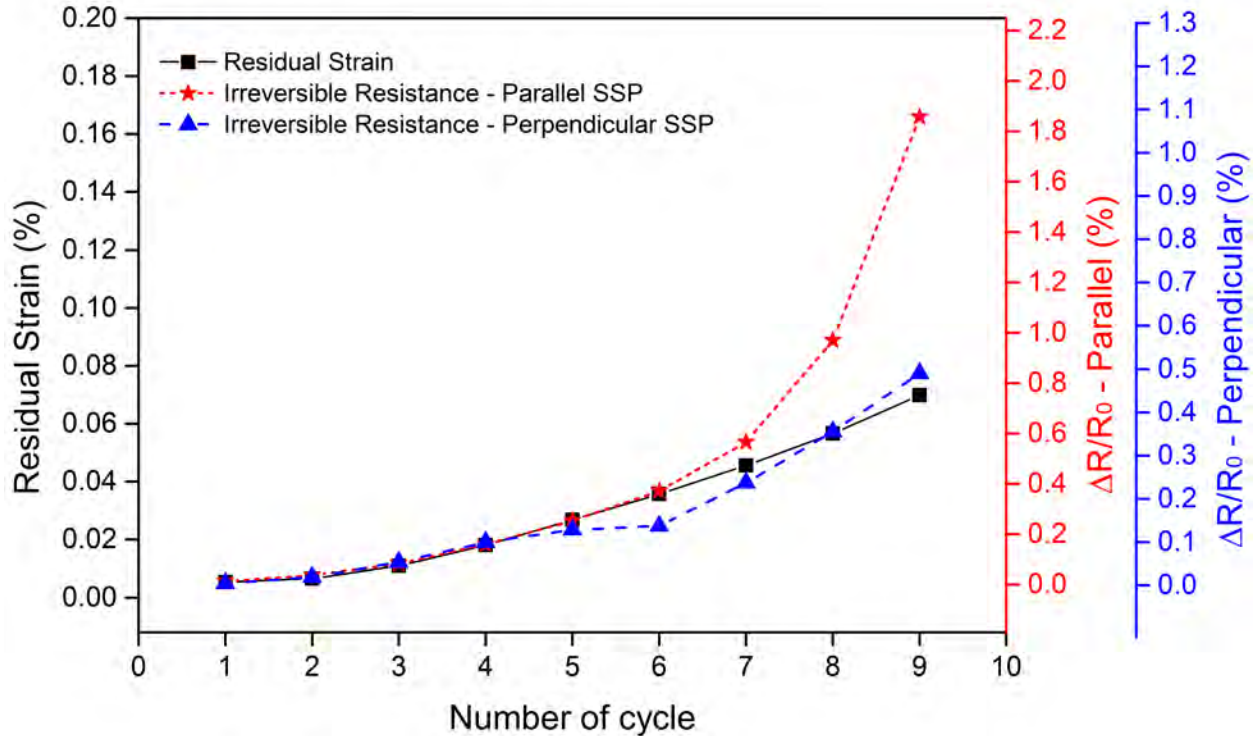


Figure 5.8. Residual axial strain and corresponding irreversible resistance change of parallel and perpendicular SSPs in the cyclic tests with progressively increasing load; the cycles are identical to those in Figure 5.7.

As shown above, the CNT SSPs exhibited quite consistent piezoresistive performance during a few cycles of mechanical loading – unloading. It was expected that similar multi-cycle stability would also be possible. However, our further experimental results showed that this may not be the case.

The fatigue uniaxial tensile tests conducted up to 1000 cycles were performed under 0.4% and 0.8% maximum strain levels to reveal the resistance change during fatigue loading cycles. The highly repeatable resistance change patterns seen in Figure 5.9 for 0.4% strain amplitude in both types of SSPs demonstrated the feasibility of cyclically stable sensing performance for relatively low strain levels. When 0.8% strain was applied, the resistance change at consecutive loading peaks increased, and the difference between the resistance change at the maximum and minimum load values also increased during the fatigue test.



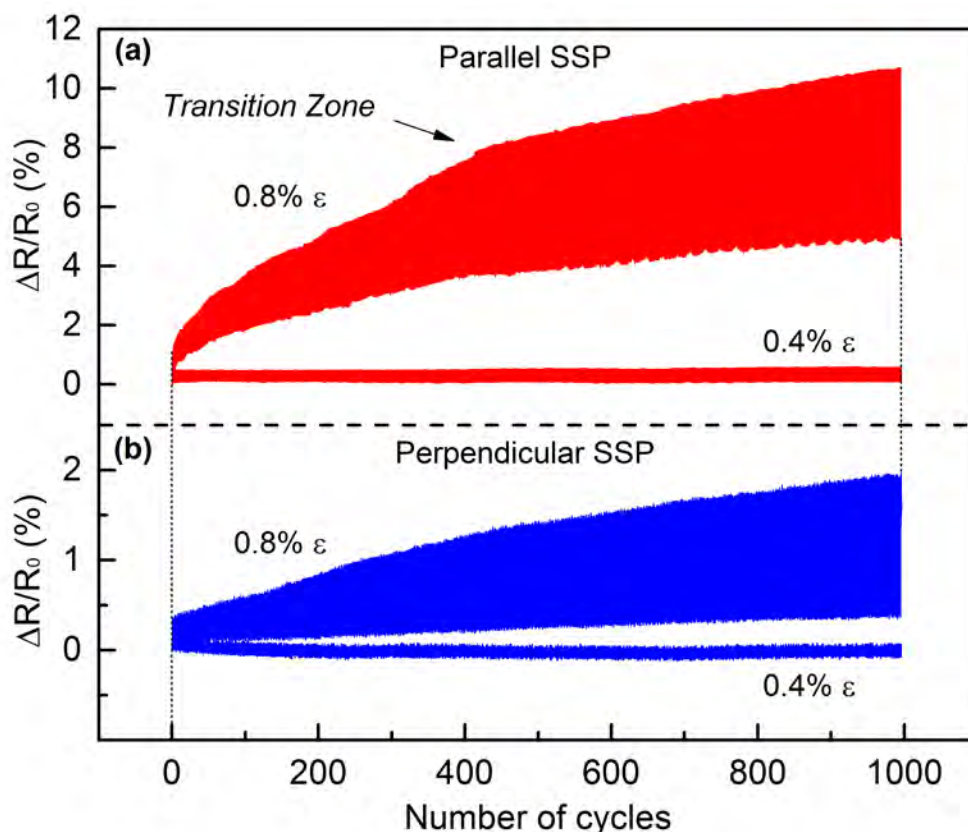


Figure 5.9. Relative resistance change ( $\Delta R/R_0$ ) response of parallel (a) and perpendicular (b) SSPs stretched to 0.4% (red) and 0.8% (black) strain during 1000 cycle-long fatigue test.

For the parallel SSP, a large increase of  $\Delta R/R_0$  was initially observed within the first several hundreds of cycles, while afterwards the  $\Delta R/R_0$  increased at a lower rate. We define this as a transition zone, where a trend of stabilization of the resistance change is observed; the latter is more pronounced in the case of parallel specimens. Importantly, during the 1000 cycle fatigue tensile tests, no extreme increase of electrical resistance change was observed, thus indicating that the SSPs were capable to function reasonably well at 0.8% strain amplitude fatigue loading.

## 5.8. Effect of Pre-straining on the Sensing Performance

Overall, the piezoresistive behavior of CNTs SSPs studied here was very stable and predictable at low strain levels, yet even better performance can possibly be achieved by further improvements of the CNT sheet structure. The piezoresistive response of CNT SSPs to the applied strain, as revealed in this work, can only be described as “quasi-linear”, which is the behavior type reported in many other studies of CNT sensing materials [4, 11, 16, 32]. Thus, more work is needed in the future to get closer to the ideal linear response for a broader strain range.

One approach in this direction is to use a pre-straining procedure, which has been implemented for some parallel SSP samples. The test coupons with attached parallel CNT SSP were first

stretched under a load controlled mode to 56 kN (~1.2% strain) and then loaded with a 7 kN increment per cycle. After the pre-straining, some of the specimens were used in the quasi-static monotonic tensile test till fracture, while some others were used in the 1000 cycle fatigue test (with the peak strain taken 0.8% for all cycles). The electrical resistance was in-situ measured during the whole process. As expected, the piezoresistive behavior of pre-strained specimens showed a closer to linear response for higher strains, as seen in Figure 5.10.

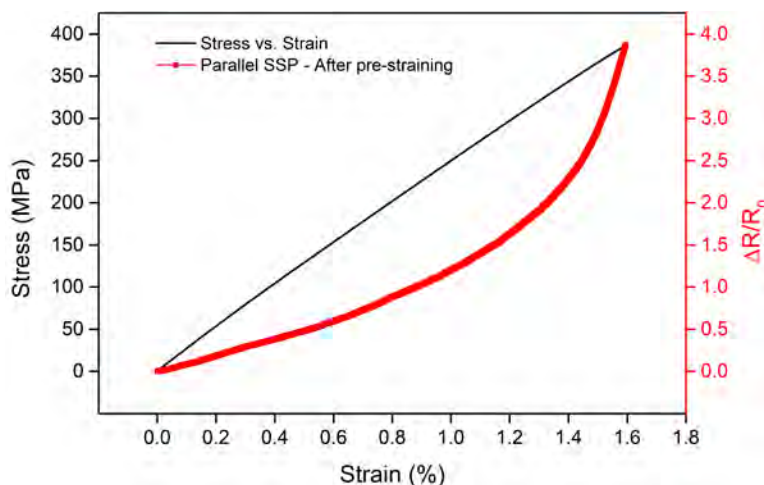


Figure 5.10. Monotonic tensile test after pre-straining, showing closer to linear behavior but lower sensitivity (GF of ~1).

As the specimens were pre-strained, the whole structure of the SSP experienced a process of pre-cracking. Since such precracks in the matrix had already permanently changed the CNT network, it was reasonable to expect that the SSP would be stabilized and behave in a “more linear” manner. As shown in Figure 5.11, the GF for the pre-strained SSP maintained a relatively constant value in the strain range from 0 to 1%.

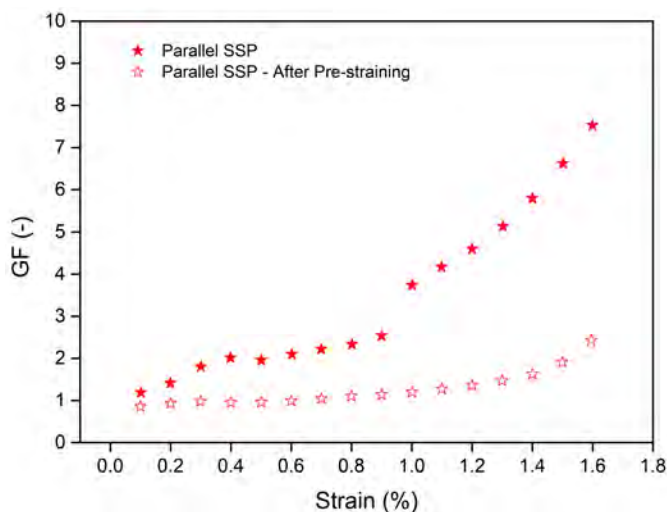


Figure 5.11. Comparison of the GF behavior of parallel SSPs with and without pre-straining under linearly increasing strain.



Since the damage was induced in the pre-strained SSPs, there was neither a major new crack formation nor a significant additional crack development when the parallel samples were loaded up to 1.0%. This is why the abrupt jump in the resistance change observed in Figure 5.4 of parallel SSPs is not observed here.

To evaluate the effect of pre-straining on the long-term piezoresistive behavior of the specimens, the data from the SSP with and without pre-straining were plotted altogether in Figure 5.12 for comparison. There is no obvious drift of  $\Delta R/R_0$  variation during the cycling of pre-strained CNT SSPs. Therefore, the pre-straining process proved to be an effective method to improve the piezoresistive performance of the CNT SSPs.

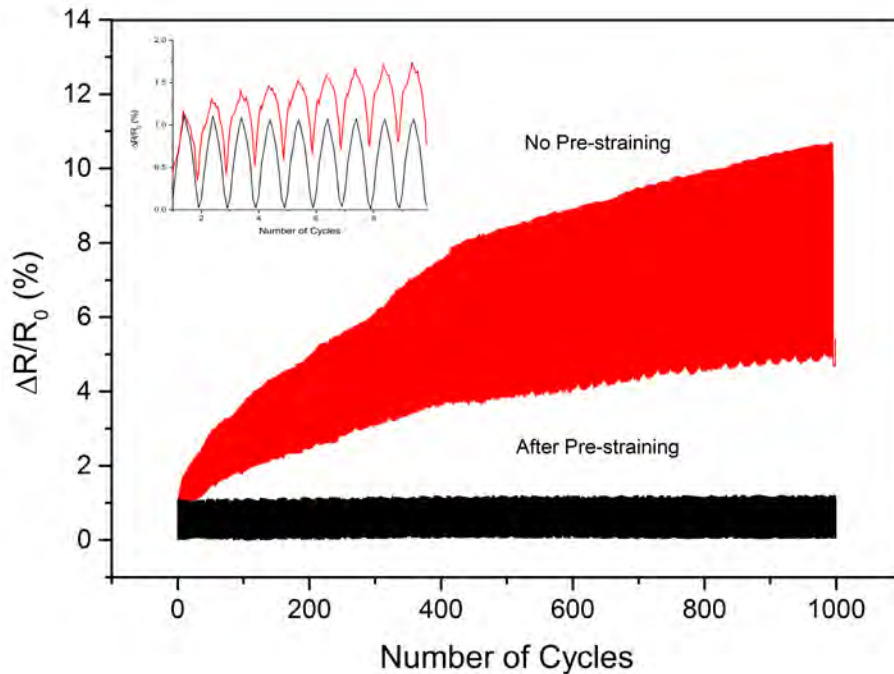


Figure 5.12. Comparison of the piezoresistive response of parallel SSPs without pre-straining (red) and after pre-straining to 1.2% (black) for 1000 cycle fatigue test. Inset: close-up of 10 cycles of  $\Delta R/R_0$  response to strain.

## 5.9. Conclusions from the CNT SSP Sensing Tests

(1) A new type of anisotropic piezoresistive CNT strain and damage sensing material was fabricated and experimentally evaluated. The sensors showed good intrinsic piezoresistive stability of the aligned nanotube sheet structure and a reversible resistance change when exposed to changing temperature.

(2) Although both parallel and perpendicular CNT SSPs followed a similar electrical resistance response to the applied strain, there was a significant effect of nanotube orientation on the SSP sensitivity, showing distinct GF in the ranges of 1 - 8 and 0.5 - 1.3 for parallel and perpendicular SSPs, respectively. This strongly anisotropic sensing performance may be useful for determining

the dominant in-service stress component(s) if multiple sensors with different orientations are used.

(3) The piezoresistive response of the CNT SSPs during 1000-cycle fatigue test displayed significant drift over time, revealing gradual damage development in the conductive nanotube network.

(4) To further improve the piezoresistive performance of the CNT SSPs, a pre-straining process was applied and showed a closer-to-linear behavior over an even wider strain range.

(5) While in this work the CNT sheets were applied to composites in the form of a surface attached patch, it is feasible to integrate them into composites as non-intrusive extremely thin and light sensors. This part of performed work is presented in Chapter 6.

## **5.10. Electromechanical Behavior of CNT SPS Composite**

One proposed application of the developed CNT shear-pressed sheets was using them as integrated strain sensors. The high intrinsic piezoresistivity and anisotropy of the electrical conductivity of CNTs, when they are embedded in the composite is favorable for creating detectable resistance change through loading in the CNT alignment preferential direction. Very little research has been conducted so far on high volume fraction CNT composites since the focus typically lies on low volume fraction (i.e. around ~1% volume fraction, which is near the typical percolation threshold) dispersed CNT composites. The closest related work [3] to the present study involved straining of infused CNT yarns; the results obtained there showed both positive and negative resistivity changes with increasing strain. That indicates complex electromechanical behavior of nanocomposites densely populated with CNTs which can also be expected when the CNT SPS are attempted as strain sensors. Experimental results obtained so far show that such an expectation is certainly true.

In order to characterize the nanocomposite, SPS tensile specimens infused with Epon 862 resin were fabricated; the CNT volume fraction was estimated in the range of 20-25% based on weight measurements and the literature data for the densities of epoxy resin and multi-walled CNTs. Silver epoxy was used to bond the tabs laser cut from 400 grit sandpaper and resistance wires as shown in Figure 5.13. Gauge length of the specimens was 7 mm. Thickness and width values of each experimental specimen were individually measured. The loading rate was chosen at 0.1 mm/min as in other tests performed in this project. Resistance was measured with an Agilent 34420A multimeter at a frequency of 10 Hz.

Results obtained for five tested SPS composite specimens are presented in Figure 5.14. Overall they show highly scattered data in both the tensile mechanical response and in the electrical resistivity variation. Such a huge scatter of the tensile stress-strain curves, as the one seen in Figure 5.14b, is surprising of course, and it can only be explained by a very high susceptibility of the CNT morphology, their SPS preform architecture and the final composite performance to the entire sequence of the manufacturing steps. Particularly surprising are high variations of the slope (i.e. the longitudinal modulus) and of the ultimate stress, which is about 4 times among individual specimens.

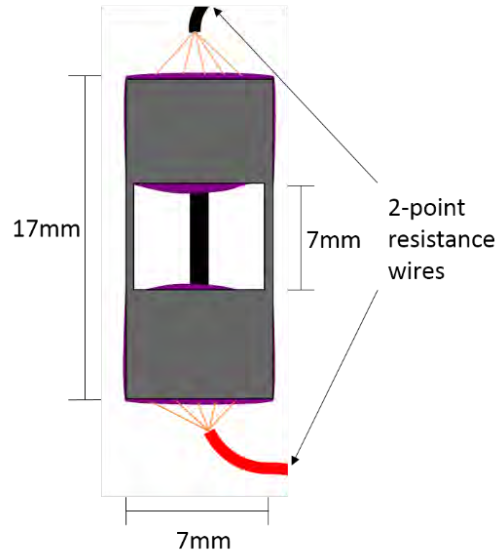
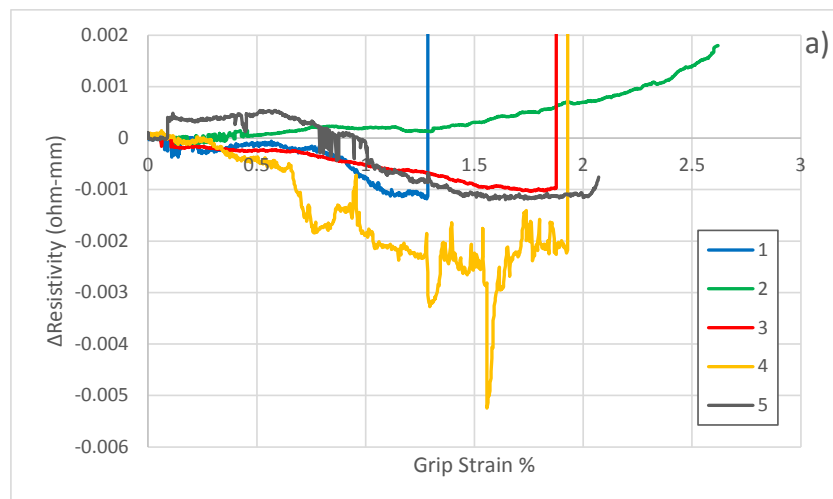


Figure 5.13. SPS composite tensile specimen for 2 point probe piezoresistive measurements.

Further, as Figure 5.14a shows, the resistivity vs. strain curves lack any consistency between five tested specimens. A very small change in resistivity response to strain occurs initially. However, three out of five specimens show an instantaneous high change in resistivity past a certain point, which is in the range of 1.3-1.9% strain. Also as Figure 5.14c shows, the jump magnitude itself for those three specimens is not consistent – it varies many times between specimens 4, 1 and 3. Normally, this “jumpy” change of electrical resistivity would be associated with some catastrophic damage suddenly appearing in the specimen which usually occurs near the point of ultimate failure. Specimen 1 shows this change at ~1.3% strain (while the ultimate failure strain is significantly higher, ~2%). But specimens 3 and 4 show excellent correlation between their respective ultimate failure strain and resistivity jump strain values. Although exact nature of these phenomena remains unknown at this point, the latter result can be viewed as initial validation that these CNT SPS composites have a potential for being developed into embedded strain and damage sensors (after significant effort towards achieving their much more stable and consistent electro-mechanical behavior, of course).



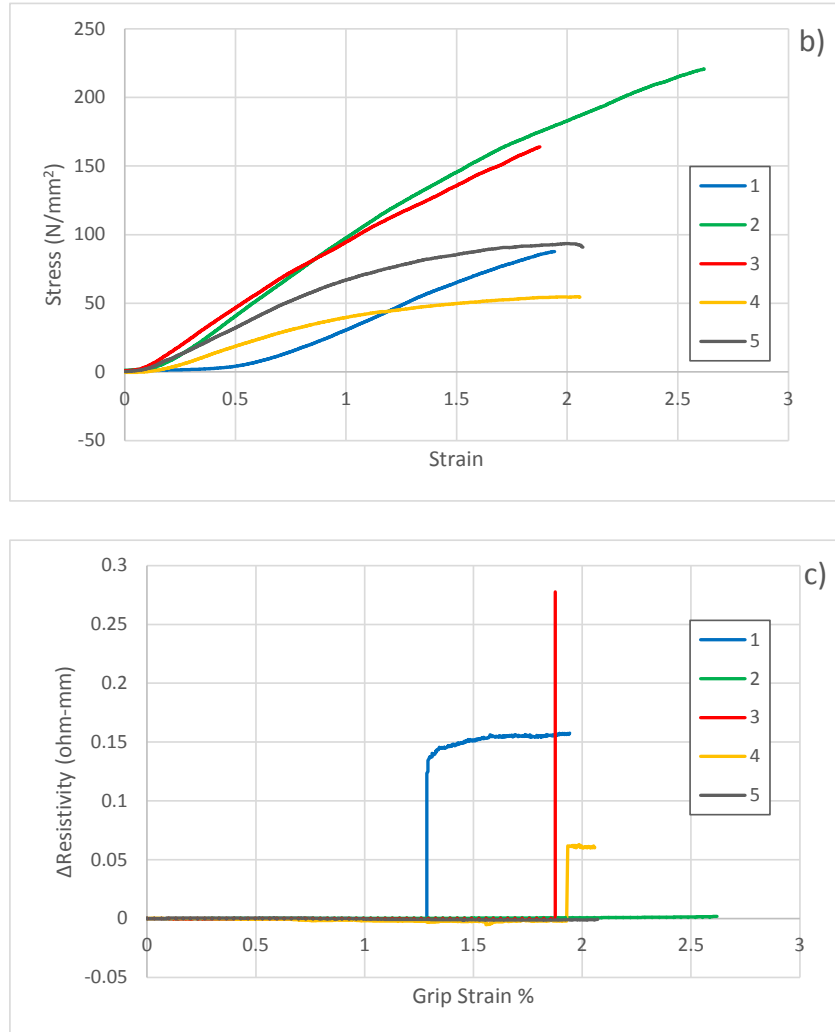


Figure 5.14. CNT SPS composites' electro-mechanical behavior under tensile loading: resistivity vs. strain variations (a); stress - strain variations (b); resistivity vs. strain variation with a different y-axis scale (c).

### 5.11. CNT SPS Composite as Surface-mounted Sensor

The large amount of “noise” seen in the resistivity vs. strain curves of Figure 5.14a is most likely due to changes from the contact resistance of the attached electrodes. To reduce this effect, a second test has been conducted by mounting the SPS composite specimen to the surface of a large fiberglass composite coupon. Then, a 4 point probe method was used to record resistance data, as illustrated in Figure 5.15. In this case the SPS composite was cured directly on the fiberglass composite coupon. Two samples were fabricated from SPS preform infused with two resin systems: Epon 862 and Epotek 301-2. The Epon SPS contained  $\sim 1500 \mu\text{m}$  long CNTs and the Epotek contained  $\sim 500 \mu\text{m}$  long CNTs. Electrodes of copper foil were bonded to the SPS composite after light sanding with 400 grit sandpaper. The region was then wiped clean with

ethanol, and silver epoxy was used to bond the foil to the prepared location. Wires were then soldered to the electrodes to provide 4 point measurement of resistance, which was used to calculate the change in resistivity of the SPS composite as strain was increased. Three specimens of each kind were prepared and tested on an MTS Landmark servo hydraulic 250 kN test system at a loading rate of 4 mm/min, and strain data were collected with a Micro Measurements 320  $\Omega$  strain gauge.

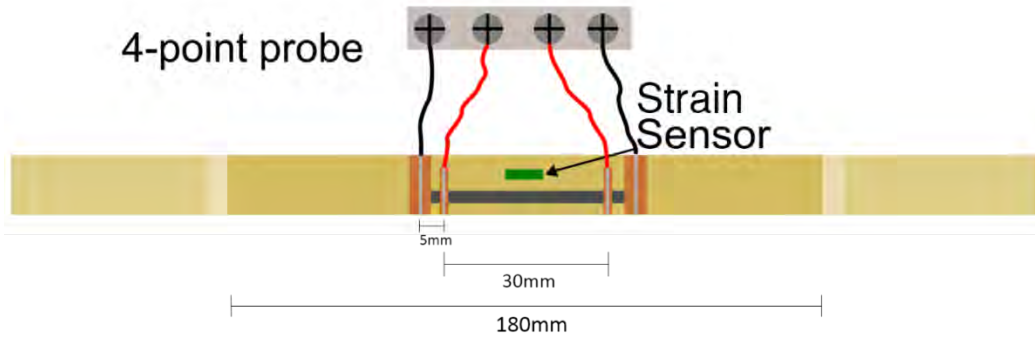
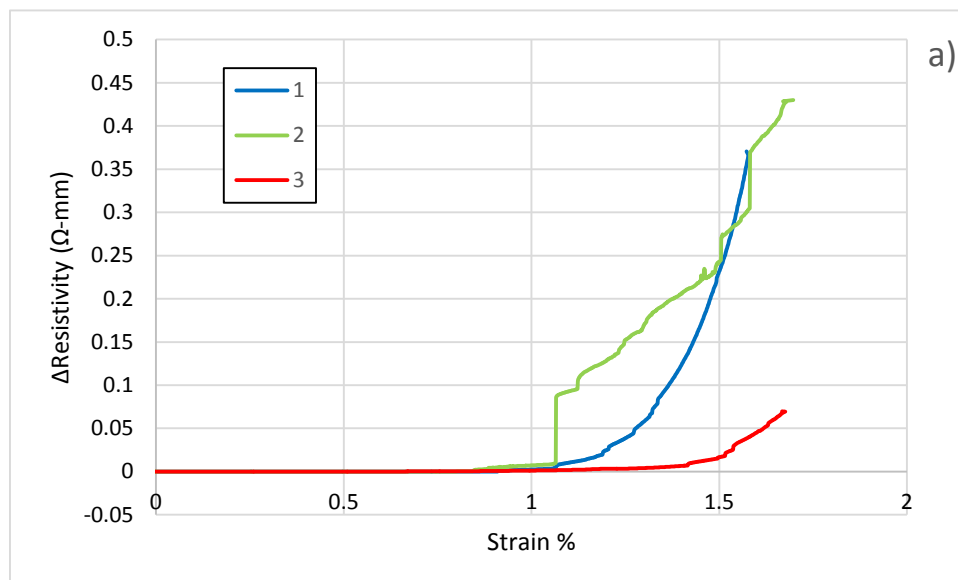


Figure 5.15. 4 point probe resistance measurement of SPS composite mounted on fiberglass composite surface.

Test results are shown in Figure 5.16. When comparing these results with the ones in Figure 5.14a it becomes evident that the noise of the curves is dramatically reduced and the consistency of electro-mechanical behavior within the group of three specimens in Figure 5.16a is much higher than in Figure 5.14a. Yet, the behavior seen in Figure 5.16b is still inconsistent within the group despite the fact that all specimens were fabricated from the same CNT array. In particular, the curve for specimen 1 in Figure 5.16b shows continuous resistance decrease with increasing strain, the curve for specimen 3 shows continuous increase, and the curve for specimen 2 show a combination of these two opposite behaviors.



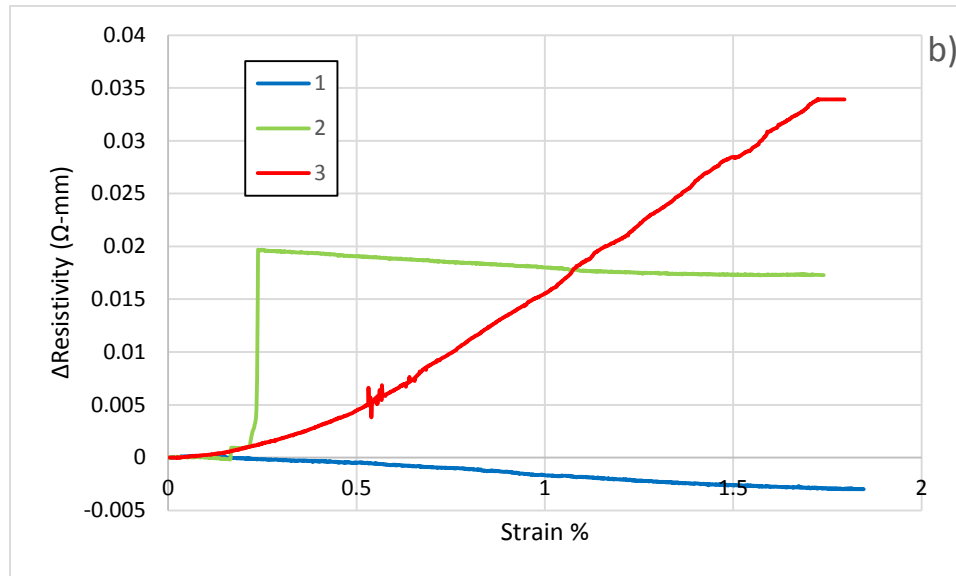


Figure 5.16. Resistivity measurements for Epon 862 infused (a) and Epotek 301-2 infused (b) CNT SPS composites.

In summary, as the presented results show, the sought stability and consistency of electro-mechanical behavior of these CNT SPS nanocomposites has not been achieved even if they are bonded to the other composite surface. One possible hypothesis is that opposite electrical resistance variations with strain may be due to the effect of different chirality of the CNTs, which has been shown in [43]. It is possible that the growth method of the CNTs produces regions of different chiralities depending on the distance to the wall of the tube furnace, as molecular flow and diffusion into the arrays may be different. Another influence might occur from the slight draw that occurs when transferring the prepreg to the surface of the fiberglass composites. This has been shown to have a large effect on electrical properties of aligned CNT composites [44]. As this processing step is hard to control, the result may be inconsistent between same batch specimens, hence it could also account for the observed differences in electro-mechanical response. Some other physical effects not discussed here may be of significance as well.

## 5.12. Conclusions

In conclusion, as it stands now the electro-mechanical behavior of high volume fraction CNT composites is not consistent enough to claim that they can be practically used as embedded strain sensors. Also importantly, the mechanisms of their electrical resistance change are not understood so far, and it certainly requires further extensive experimental and theoretical studies in order to isolate each important variable and to determine its contribution to the total response of very complex CNT networks within the SPSs and their composites under mechanical loading. Additional problem is that the gauge factor values achieved at this time with SPS composites are relatively low (barely 1) and it is not clear how to increase this number substantially.

Some additional comments on the performed SPS sensor study may be useful. It is evident from the literature that maximized (and commonly sought) CNT-reinforced composite self-sensing

capability corresponds to a rather low volume content (typically much below 1%, and can be as low as 0.005%) of short CNTs dispersed in a polymer matrix; the critical CNT volume content corresponds to the characteristic percolation threshold of each specific CNT-polymer mixture system. Also, it is always desirable using single-walled CNTs with unidirectional alignment in order to achieve a percolation effect at the lowest possible volume fraction. Single-walled CNTs are necessary to enhance the intrinsic piezoresistance of the nanotubes as they have much higher resistance changes with strain compared to multi-walled CNTs. Further, concerning intrinsic electro-mechanical behavior, it is questionable how effective is the stress transfer from one CNT to the other through a matrix, knowing that the efficiency of internal stress transfer within a nanocomposite is critical to the realization of intrinsic piezoresistivity changes. It is worth pointing out that the CNT SPSs studied here are very different from the aforementioned ideal CNT piezoresistive networks in at least three aspects: (i) they are made of very long CNTs, (ii) the CNTs are essentially multi-walled, and (iii) the SPS reinforced composites are far and away above the common percolation threshold in terms of the CNT volume fraction.

Intrinsic behavior is also dependent on chirality of the CNT. Chirality can change depending on growth conditions, growth location, number of walls, catalyst type, etc., and all that may result in either positive or negative resistivity change under mechanical loading. Chirality can also change along the length of a nanotube. In order to understand the mechanisms of a CNT sensor, it is necessary to determine the most conductive chirality in the CNT network, which will further determine the in-situ piezoresistive behavior of a composite sensor. This can easily be measured with single-walled, possibly even double-walled nanotubes, but not with multi-walled ones. It could be possible to “burn out” some chiralities using electric current in order to simplify the system. This approach is based on the principle that electric current will flow through the most conductive CNTs, generating heat and degrading that structure. In this way it is possible to gradually and sequentially eliminate the most conductive chirality until the desired structure is reached. According to available multi-layer graphene measurements, through thickness conductivity is 1000 times lower than that along planar surface, so it is unlikely for an electron to “penetrate” through an outer wall and reach the adjacent inner wall in a nanotube unless there is a large defect or the tube ends are open. This means that inner wall chirality will not have any significant impact on the piezoresistive behavior while it will show up in the measurement, thus hiding the actual chirality of the outer walls. Note that as was shown in Section 2.2, the number of walls in the grown CNTs is measured in tens.

With nanocomposite systems that are similar to our SPSs in terms of high CNT volume fraction, it appears that the maximum gauge factor achieved was only  $\sim 1$  (which we are close to). This value would further decrease if the preform structure is densified further. In order to reduce that very high variability of the electromechanical response reported in Sections 5.10 and 5.11, it would be desirable to control the nanotube architecture within an SPS by achieving better alignment of the CNTs and maximize their packing density. However, that would obviously make a negative effect on the gauge factor value. Some literature shows that random CNT structure actually results in a higher gauge factor, which suggests that high alignment of the CNTs in SPS (which is one of its unique characteristics) would play against increasing gauge factor.

Therefore, at this point CNT SPS preforms and their composites look not consistent enough and not sensitive enough to be used as a strain sensor. Also, the current state-of-the-art long CNT



morphology in the vertically grown arrays is very wavy, which is another important factor since the intrinsic CNT piezoresistance would be best transferred to the SPS sensor if the CNTs were perfectly straight and aligned with the loading direction of a sensor. The drawn CNT sheets also studied here are actually closer to the ideal CNT piezoresistive structure, but even those are still somewhat inconsistent as far as initial resistivity is concerned.

### 5.13. References

1. Thostenson, E. T.; Ren, Z.; Chou, T. Advances in the Science and Technology of Carbon Nanotubes and Their Composites: A Review. *Composites Sci. Technol.*, 2001, **61**, 1899-1912.
2. Abot, J.L.; Song, Y.; Vatsavaya, M.S.; Medikonda, S.; Kier, Z.; Jayasinghe, C.; et al. Delamination Detection with Carbon Nanotube Thread in Self-sensing Composite Materials. *Composites Sci. Technol.*, 2010, **70**, 1113-1119.
3. Zhao, H.; Zhang, Y.; Bradford, P.D.; Zhou, Q.; Jia, Q.; Yuan, F.; et al. Carbon Nanotube Yarn Strain Sensors. *Nanotechnology*, 2010, **21**, 305502.
4. Hehr, A.; Schulz, M.; Shanov, V.; Song, Y. Embedded Carbon Nanotube Thread Piezoresistive Strain Sensor Performance. *Sens. Rev.*, 2014, **34**, 209-219.
5. Song, Y.; Hehr, A.; Shanov, V.; Alvarez, N.; Kienzle, N.; Cummins, J.; et al. Carbon Nanotube Sensor Thread for Distributed Strain and Damage Monitoring on IM7/977-3 Composites. *Smart Mater. Struct.*, 2014, **23**, 075008.
6. Hehr, A.; Schulz, M.; Shanov, V.; Song, Y. Micro-crack Detection and Assessment with Embedded Carbon Nanotube Thread in Composite Materials. *Structural Health Monitoring*, 2014, 1475921714532987.
7. Dharap, P.; Li, Z.; Nagarajaiah, S.; Barrera, E. Nanotube Film Based on Single-wall Carbon Nanotubes for Strain Sensing. *Nanotechnology*, 2004, **15**, 379.
8. Li, X.; Levy, C.; Elaadil, L. Multiwalled Carbon Nanotube Film for Strain Sensing. *Nanotechnology*, 2008, **19**, 045501.
9. Li, Z.; Dharap, P.; Nagarajaiah, S.; Barrera, E.V.; Kim, J. Carbon Nanotube Film Sensors. *Adv. Mater.*, 2004, **16**, 640-643.
10. Vemuru, S.; Wahi, R.; Nagarajaiah, S.; Ajayan, P. Strain Sensing Using a Multiwalled Carbon Nanotube Film. *The Journal of Strain Analysis for Engineering Design*, 2009, **44**, 555-562.
11. Alexopoulos, N.; Jaillet, C.; Zakri, C.; Poulin, P.; Kourkoulis, S. Improved Strain Sensing Performance of Glass Fiber Polymer Composites with Embedded Pre-stretched Polyvinyl Alcohol–Carbon Nanotube Fibers. *Carbon*, 2013, **59**, 65-75.
12. Sebastian, J.; Schehl, N.; Bouchard, M.; Boehle, M.; Li, L.; Lagounov, A.; et al. Health Monitoring of Structural Composites with Embedded Carbon Nanotube Coated Glass Fiber Sensors. *Carbon*, 2014, **66**, 191-200.
13. Zhang, J.; Liu, J.; Zhuang, R.; Mäder, E.; Heinrich, G.; Gao, S. Single MWNT-Glass Fiber as Strain Sensor and Switch. *Adv. Mater.*, 2011, **23**, 3392-3397.
14. Kang, I.; Schulz, M. J.; Kim, J.H.; Shanov, V.; Shi, D. A Carbon Nanotube Strain Sensor for Structural Health Monitoring. *Smart Mater. Struct.*, 2006, **15**, 737.
15. Loh, K. J.; Kim, J.; Lynch, J. P.; Kam, N. W. S.; Kotov, N. A. Multifunctional Layer-by-Layer Carbon Nanotube–Polyelectrolyte Thin Films for Strain and Corrosion Sensing. *Smart Mater. Struct.*, 2007, **16**, 429.

16. Njuguna, M.; Yan, C.; Hu, N.; Bell, J.; Yarlagadda, P. Sandwiched Carbon Nanotube Film as Strain Sensor. *Composites Part B: Engineering*, 2012, **43**, 2711-2717.
17. Park, M.; Kim, H.; Youngblood, J.P. Strain-dependent Electrical Resistance of Multi-walled Carbon Nanotube/Polymer Composite Films. *Nanotechnology*, 2008, **19**, 055705.
18. Pham, G.T.; Park, Y.; Liang, Z.; Zhang, C.; Wang, B. Processing and Modeling of Conductive Thermoplastic/Carbon Nanotube Films for Strain Sensing. *Composites Part B: Engineering*, 2008, **39**, 209-216.
19. Zhang, R.; Deng, H.; Valenca, R.; Jin, J.; Fu, Q.; Bilotti, E.; et al. Strain Sensing Behaviour of Elastomeric Composite Films Containing Carbon Nanotubes Under Cyclic Loading. *Composites Sci. Technol.*, 2013, **74**, 1-5.
20. Zhang, W.; Suhr, J.; Koratkar, N. Carbon Nanotube/Polycarbonate Composites as Multifunctional Strain Sensors. *J. of Nanoscience and Nanotechnology*, 2006, **6**, 960-964.
21. Liu, Y.; Chakrabartty, S.; Gkinosatis, D. S.; Mohanty, A.K.; Lajnef, N. Multi-walled Carbon Nanotubes/Poly (l-lactide) Nanocomposite Strain Sensor for Biomechanical Implants. 2007, 119-122.
22. De la Vega, A.; Sumfleth, J.; Wittich, H.; Schulte, K. Time and Temperature Dependent Piezoresistance of Carbon Nanofiller/Polymer Composites Under Dynamic Load. *J. Mater. Sci.*, 2012, **47**, 2648-2657.
23. Gao, L.; Thostenson, E.T.; Zhang, Z.; Chou, T. Sensing of Damage Mechanisms in Fiber-Reinforced Composites Under Cyclic Loading Using Carbon Nanotubes. *Advanced Functional Materials*, 2009, **19**, 123-30.
24. Ku-Herrera, J.; Avilés, F. Cyclic Tension and Compression Piezoresistivity of Carbon Nanotube/Vinyl Ester Composites in the Elastic and Plastic Regimes. *Carbon*, 2012, **50**, 2592-2598.
25. Li, C.; Chou, T. Modeling of Damage Sensing in Fiber Composites Using Carbon Nanotube Networks. *Composites Sci. Technol.*, 2008, **68**, 3373-3379.
26. Nofar, M.; Hoa, S.; Pugh, M. Failure Detection and Monitoring in Polymer Matrix Composites Subjected to Static and Dynamic Loads Using Carbon Nanotube Networks. *Composites Sci. Technol.*, 2009, **69**, 1599-1606.
27. Saafi, M. Wireless and Embedded Carbon Nanotube Networks for Damage Detection in Concrete Structures. *Nanotechnology*, 2009, **20**, 395502.
28. Böger, L.; Wichmann, M. H.; Meyer, L. O.; Schulte, K. Load and Health Monitoring in Glass Fibre Reinforced Composites with an Electrically Conductive Nanocomposite Epoxy Matrix. *Composites Sci. Technol.*, 2008, **68**, 1886-1894.
29. Zetina-Hernández, O.; Duarte-Aranda, S.; May-Pat, A.; Canché-Escamilla, G.; Uribe-Calderon, J.; Gonzalez-Chi, P.; et al. Coupled Electro-mechanical Properties of Multiwall Carbon Nanotube/Polypropylene Composites for Strain Sensing Applications. *J. Mater. Sci.*, 2013, **48**, 7587-7593.
30. Thostenson, E. T.; Chou, T. Real-time In Situ Sensing of Damage Evolution in Advanced Fiber Composites Using Carbon Nanotube Networks. *Nanotechnology*, 2008, **19**, 215713.
31. Fiedler, B.; Gojny, F. H.; Wichmann, M. H.; Bauhofer, W.; Schulte, K. Can Carbon Nanotubes be Used to Sense Damage in Composites? 2004, **29**, 81-94.
32. Oliva-Avilés, A.; Avilés, F.; Sosa, V. Electrical and Piezoresistive Properties of Multi-walled Carbon Nanotube/Polymer Composite Films Aligned by an Electric Field. *Carbon*, 2011, **49**, 2989-97.

33. Theodosiou, T.; Saravanos, D. Numerical Investigation of Mechanisms Affecting the Piezoresistive Properties of CNT-doped Polymers Using Multi-scale Models. *Composites Sci. Technol.*, 2010, **70**, 1312-1320.
34. Yildiz, O.; Bradford, P. D. Aligned Carbon Nanotube Sheet High Efficiency Particulate Air Filters. *Carbon*, 2013, **64**, 295-304.
35. ASTM Standard D3039/D3039M-08, 2008, "Standard Test Method for Tensile Properties of Polymer Matrix Composite Materials". ASTM International, West Conshohocken, PA, 2007.
36. Koratkar, N.; Modi, A.; Lass, E.; Ajayan, P. Temperature Effects on Resistance of Aligned Multiwalled Carbon Nanotube Films. *J. of Nanoscience and Nanotechnol.*, 2004, **4**, 744-748.
37. Zhang, M.; Fang, S.; Zakhidov, A. A.; Lee, S.B.; Aliev, A. E.; Willims, C.D.; et al. Strong, Transparent, Multifunctional, Carbon Nanotube Sheets. *Science*, 2005, **309**, 1215-9.
38. Wang, D.; Song, P.; Liu, C.; Wu, W.; Fan, S. Highly Oriented Carbon Nanotube Papers Made of Aligned Carbon Nanotubes. *Nanotechnology*, 2008, **19**, 075609.
39. Zhang, Y.; Sheehan, C. J.; Zhai, J.; Zou, G.; Luo, H.; Xiong, J.; et al. Polymer-Embedded Carbon Nanotube Ribbons for Stretchable Conductors. *Adv. Mater.*, 2010, **22**, 3027-3031.
40. Hu, N.; Karube, Y.; Arai, M.; Watanabe, T.; Yan, C.; Li, Y.; et al. Investigation on Sensitivity of a Polymer/Carbon Nanotube Composite Strain Sensor. *Carbon*, 2010, **48**, 680-687.
41. Hu, N.; Karube, Y.; Yan, C.; Masuda, Z.; Fukunaga, H. Tunneling Effect in a Polymer/Carbon Nanotube Nanocomposite Strain Sensor. *Acta Mater.*, 2008, **56**, 2929-2936.
42. Ogasawara, T.; Moon, S.; Inoue, Y.; Shimamura, Y. Mechanical Properties of Aligned Multiwalled Carbon Nanotube/Epoxy Composites Processed Using a Hot-melt Prepreg Method. *Composites Sci. Technol.*, 2011, **71**, 1826-33.
43. Cullinan, M. A.; Culpepper, M. L. Effects of Chirality and Impurities on the Performance of Carbon Nanotube-based Piezoresistive Sensors. *Carbon*, 2013, **51**, 59-63.
44. Zhao, H.; Zhang, Y.; Bradford, P. D.; Zhou, Q.; Jia, Q.; Yuan, F.-G.; Zhu, Y. Carbon Nanotube Yarn Strain Sensors. *Nanotechnology*, 2010, **21**, 305502.

## **CHAPTER 6. STRAIN SENSING OF COMPOSITE BONDED JOINTS WITH EMBEDDED CNT SHEETS**

Carbon nanotube (CNT) networks exhibit piezoresistive behavior which is attractive for strain and damage sensing in composite joints. Research presented in this chapter uses CNT drawn sheets (DS) and much thicker shear pressed sheets (SPS), manufacturing of which has been described in the previous chapters, for strain sensing in double-strap joints of composite adherends bonded by an adhesive layer. The CNT sensors are integrated within that adhesive layer. The electro-mechanical behavior of adhesive joints was first monitored during in-plane tensile loading with the use of embedded DS; the recorded resistance change with strain was significant. As a sensor, the CNT DS is mainly capturing the longitudinal in-plane strain averaged across the overlap area. The SPS was then cut into 1-2 mm wide strips and added to the DS at the overlap ends of the joint; much greater resistance change with strain under equivalent nominal strain level (measured from the grip displacement) was observed. This difference in the resistance response suggests an ability of CNT SPS to capture additional strain components (primarily, the transverse peel strain) which have high concentration factors near the joint overlap ends. Also importantly, as the obtained results show, the embedment of either DS or SPS did not cause any considerable change in the measured strength of the joints, which indicates that the developed strain sensing approach qualifies as a non-intrusive and thus can be further explored as a viable candidate for continuous health monitoring of composite structures, micro-systems and micro-devices.

### **6.1. Introduction**

It is well known that adhesively bonded joints offer many advantages for assembling composite structures due to their relative processing simplicity, reduced stress concentration and increased reliability, significant weight savings and cost effectiveness over conventional bolted joints and mechanical fasteners. However, there is one critical drawback of adhesively bonded joints, which is the difficulty of their regular inspections due to the inability to disassemble them during the service life [1]. Only some of the relatively complex non-destructive testing methods can be applied to the adhesively bonded composite structures for structural health monitoring, though infrequently and at high cost. Although there have been many advances in structural health monitoring of composites, actively monitoring the bonded region in adhesively joined composites has proven to be very challenging. This is mainly due to the high sensitivity of the adhesive layer to intrusive sensing materials which can significantly degrade the strength of the joint. One way around that is to embed “non-intrusive” (this term should be used with certain reservation) sensing elements that are small compared to the bondline thickness, relatively compliant for practical embedment and, at the same time, interact well with the surrounding adhesive and/or composite matrix material. While most traditional sensors do not meet this description, CNT-based strain sensing materials do.

Due to their intrinsic piezoresistive behavior and low percolation threshold, various types of CNT networks are often incorporated into composites for the purpose of strain sensing. Some research has been conducted to make CNT/polymer nanocomposites with self-sensing capability by incorporating different types of CNT assemblies, e.g. CNT buckypaper [2], vertically aligned CNT arrays [3] and dispersed CNT network [4, 5] into a polymer matrix. With a similar

motivation, some groups of researchers have also attempted to add CNTs into polymeric adhesives in order to simultaneously provide mechanical reinforcement and/or self-sensing capability to composite bonded joints. As literature shows, the effect of dispersed CNTs on the modified adhesive mechanical properties and/or joint strength is not straightforward and the trends are often contradictory. Yet most of the mechanical test data show a moderate strength increase at relatively low (e.g., less than 1 wt%) CNT content, but a sharp strength decrease was observed at higher CNT content values [6-13]. At the same time, the purpose of creating electrically conductive networks within originally insulating polymeric adhesives by dispersing short (typically, less than 10 micron length) CNTs has been successfully accomplished in many published works. Notably, several studies showed that as low as 0.05-0.1 wt% CNT content is sufficient for reaching the electrical conductivity percolation threshold and, therefore, using even so sparsely populated CNT networks for strain and damage sensing should be feasible. And, even without special mechanical testing, one can expect that mechanical properties of the CNT-modified adhesives or bonded joints made with them would not be considerably affected by the added CNTs.

Contrary to the purpose of mechanical reinforcement, the utilization of CNT networks in adhesively bonded composite joints for strain/damage sensing has been attempted only in a few works. Specifically, in [1] a dispersed CNT network was used to monitor crack initiation and propagation in the joints, and ultimately detecting the start of catastrophic joint failure. It was also shown there that different failure modes of adhesive joints can be distinguished according to the electrical resistance behaviors in response to strain. Damage sensing of dispersed CNT network in dynamic fatigue testing was attempted in order to predict the failure of the composite joint and estimate its service life [11]. Damage sensing in CNT reinforced joints was studied to attain a threshold shear strain for the alarm of potential joint fracture [14]. Notably, adhesive systems are typically of a relatively high viscosity, which makes it difficult to produce a uniformly dispersed homogenous mixture of CNTs and adhesive. Thus, CNT length, volume fraction, and alignment are sacrificed for a successful mixing. Adhesive mixtures with CNTs are typically produced from shear mixing or ball milling, the processes which typically require short nanotubes to minimize viscosity of the mixture (it is known that viscosity dramatically increases with increasing CNT volume content and their length). On the other hand, if longer nanotubes are used, both shear mixing and ball milling may significantly fracture them thus reducing a sensing capability of the network. Therefore, alternative approaches that avoid CNT mixing with adhesive, are of scientific and practical interest. The strain sensing approach explored in this work is based on the concept of incorporating two different kinds of self-sustained assemblies (“sheets”) of long aligned CNTs into adhesive layer of composite bonded joints and measuring their in-situ electrical resistance change during mechanical loading.

## **6.2. In-situ Strain Sensing Using CNT Sheets**

The strain sensing approach proposed here allows one to avoid mixing CNTs with adhesive. Instead, two different forms of very thin CNT assembly (called “drawn sheet” and “shear-pressed sheet”), which are self-sustained and can be manipulated by hand, are embedded within adhesive material and then integrated within the bonded joint. A CNT drawn sheet (DS) is continuously drawn from the chemical vapor deposition (CVD) grown CNT array and results in a self-sustained structure assembled from well aligned long CNTs. As shown in Chapter 5 and

our publication [17], CNT DS serves well as a strain sensing material when being attached to the exterior surface of a composite. In this chapter it is demonstrated that CNT DS can be also successively used as a non-intrusive sensing element embedded in composite adhesive joints.

It has to be pointed out that the strain sensing capability of this material is due to totally different electro-mechanical phenomena than in the aforementioned case of adhesives modified with very low content CNTs. The very high (measured in hundreds of thousands) aspect ratio values of CNTs used here, when combined with their relatively close packing in the drawn sheet, makes this material already highly conductive in its strain-free condition. It retains that high conductivity after being embedded in the adhesive, and also after the next step of being integrated into the adhesive layer of the bonded joint. Even in the strain-free state of the sheet, there are numerous CNT contact points along each CNT which create a continuous path of conduction throughout the sheet. Therefore, when this material is exposed to a mechanical loading, the expected transition would be from one highly conductive state to another, without nearly as dramatic change of electrical conductivity (many orders of magnitude) as in the case of dispersed CNT - adhesive mixtures near the percolation threshold. This factor alone makes the subject of this work very challenging. Also importantly, as shown in Chapter 5 and [17], the dominating alignment of the CNTs in the drawn sheet produces an anisotropic, nearly unidirectional, strain sensing element with relatively small contribution to the resistance change from the transverse strains (e.g., the strains perpendicular to the direction of CNT alignment, both the in-plane and out-of-plane strains). This nature of the DS allows one to utilize its maximum sensitivity of electrical resistance change with strain when the major strain direction coincides with the direction of CNT alignment in the DS. Therefore, it is also expected that this particular type of CNT assembly would serve as an improved sensing element in comparison to macroscopically isotropic CNT-adhesive mixtures.

Therefore, the above described DS sensor is extremely thin, plain, and anisotropic in its electro-mechanical response. As such, it is expected to have a relatively low sensitivity to transverse (a.k.a. “peel”) strain generated in the through thickness direction near the overlap ends in the joint. As well known, that strain component plays a crucial role in the failure initiation of adhesive joints; it arises near the overlap ends under loading of a joint and may reach magnitudes far above those of the in-plane strain in the loading direction. It is very difficult to directly measure such a highly localized peel strain in a bonded joint because the adherends are usually thin and the adhesive layer is even thinner. Measuring the peel strain at the overlap end of a bonded joint by orienting traditional strain sensor in the through thickness direction is problematic, and measuring the peel strain within adhesive layer by any traditional sensor means is hardly possible.

One feasible approach to overcome these difficulties is to integrate fiber optics sensors within adherends and/or adhesive layer during joint fabrication. Some examples of success achieved in this direction can be found in [18, 19], where extrinsic Fabry-Perot interferometric fiber optic sensors and multiplex Bragg grating fiber optic sensors have been integrated within 3D orthogonal woven preforms in different fiber directions, and most notably in the through-thickness reinforcement direction of the composite adherends. After composite bonded joints were fabricated with those sensor-instrumented adherends, the peel strain arising under loading was successfully measured very close to the overlap end. Therefore, in that case an advantage

has been taken of the through-thickness segments of continuous “Z-yarns” in a 3D woven preform serving as the sensor carriers. Specifically, several strings of integrated multiplex unidirectional Bragg grating sensors were used to measure the peel strain distributions near the overlap end and in a close proximity of the adhesive layer. That general concept can be also applied to the integration of appropriate assemblies of CNTs into adhesive bonded joints if the DS can be oriented in the through-thickness direction within adhesive layer. That would provide in-situ peel strain measurements. This approach is conceptually possible, but its practical feasibility has not been proven yet.

Alternatively, it may be attempted using a different, much thicker, and essentially a three-dimensional structure formed from aligned CNTs which could selectively sense electrical resistance change of adhesive layer in through thickness direction and thus provide the means for in-situ peel strain monitoring. If such approach shows feasible, it would enable for a valuable practical sensing means to measure the peel strain concentration in the critical regions near the overlap ends. One seemingly suitable CNT assembly type for this purpose is aligned shear pressed CNT sheet (SPS) originally introduced in [15] and described in the previous chapters of this report. Importantly, a CNT SPS is many times thicker than a CNT DS, although they both have an aligned CNT structure and showed similar electrical conductivity anisotropy.

In this experimental study, CNT DS, which is very thin, and CNT SPS, which is much thicker, were incorporated (separately and conjointly) into the mid-plane of an epoxy adhesive layer across entire overlap region of composite “double strap” joint (DSJ). The set goal was twofold: (1) to observe what an effect on the mechanical properties of the bonded joint each of these materials separately, and both together, can make; and (2) to verify if each of these materials and their combination respond to the mechanical loading by a measurable electrical resistance change. If there is no or minimal effect on the joint strength, then the DS and/or SPS can be categorized as non-intrusive sensing elements and may be further evaluated for a potential in-situ strain monitoring. The mechanical strength of the joints with integrated DS and SPS was evaluated in this work under monotonic in-plane tensile loading. Simultaneously with the mechanical loading, their sensing performance was examined by measuring the electro-mechanical interdependence.

Early on in this study it became apparent that “dry” (as-produced) SPS was not sufficiently impregnated with the chosen commercial high-viscosity epoxy adhesive paste; as a result, the SPS sheet was not able to efficiently transfer stresses throughout the joint structure. Not to a surprise then, when the joint with dry SPS extending through entire overlap area was tested, a dramatic decrease of the joint strength was observed as compared to the tested “baseline” joint, which did not incorporate any CNT sheet. The revealed SPS infusion problem can be solved by pre-infusing it with a different, preferably much lower viscosity resin (which should be compatible to the host adhesive of course). However, this path has not been further explored yet. Instead, it was attempted to solve the problem by strategically placing narrow strips of the SPS only in the overlap end regions. With such a localized SPS addition, the overall integrity of the joint was not compromised and, as the test data showed, the joint retained most of its load-bearing capacity. At the same time, with such a narrow strip of SPS added to the DS (recall that the latter one extends across entire overlap area), the conducting CNT network integrated in the joint gained additional, essentially three-dimensional, features regarding the electro-mechanical



response. It is believed that those features should enable to monitor not just the in-plane longitudinal strain (like in the case of the DS) but a more complete 3D strain field and, particularly, to capture the peel strain component.

Although establishing a quantitative correlation between the electrical resistance change of the joint on one side, and the increasing internal peel strain on the other, has not been attempted yet, our initial results presented here clearly indicate that such correlation exists. It is believed that the observed substantial difference in the resistance change between the DS-only case and the DS-plus-SPS strips case, can be directly attributed to a contribution of the through thickness peel strains arising near the overlap ends. Thus, combining the DS as a non-intrusive continuous conductive element with strategically placed narrow SPS strips looks most promising for the further development of this novel in-situ strain sensing method.

### 6.3. Joint Sample Fabrication

In this study, four groups of joint samples with different adhesive interlayers were fabricated: (1) epoxy adhesive only (baseline, “B”), (2) CNT DS embedded between two layers of adhesive and covering entire overlap area (drawn sheet, “D”), (3) DS with added 1-2 mm wide CNT SPS strips placed near the overlap edges (edge shear-pressed sheet, “E”), and (4) CNT SPS embedded between two layers of adhesive and covering entire overlap area (shear-pressed sheet, “S”).

Drawable multi-walled carbon nanotube (MWCNT) arrays were synthesized through a chlorine-assisted low pressure chemical vapor deposition method; the aligned CNTs within the arrays typically possess dimensions of 25 - 40 nm diameter and length of ~1 mm, as described in [16]. CNT sheets composed of aligned CNTs were directly drawn out from the MWCNT array and positioned carefully between two thin layers of uncured adhesive paste which were evenly spread on both overlapping regions of the adherends and straps, as shown in Figure 6.1.

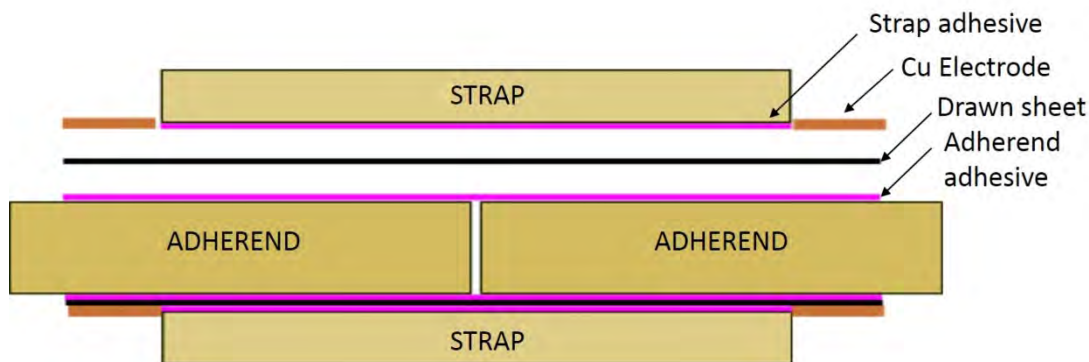


Figure 6.1. Cross section schematics of the bonded joint region for the DS specimens with an exploded view on top.

The thicker SPS was produced in the manner described in [15]. A narrow strip of SPS (1-2mm) which was composed of 1-2 mm long nanotubes was cut with a new razor blade. The cut was perpendicular to the CNT direction so that the alignment direction of the CNTs in the SPS strip matched that of the DS. The purpose of using a DS in this case is to provide a conductive

pathway between two separated SPSs. The adhesive chosen for the joint fabrication was an individually packaged two part aerospace grade epoxy adhesive, Hysol EA 9309.3N. G10/FR4 fiberglass laminate panel consisting of plain woven fiberglass and epoxy resin was purchased from American Epoxy and Metal Inc. and water jet cut into the dimensions of  $25.4 \times 203.2$  mm ( $1 \times 8$  inches) and  $25.4 \times 69.8$  mm ( $1 \times 2.75$  inches) to be used as adherends and straps, respectively. Bonding surfaces were prepped by abrading with 400 grit sandpaper and then cleaned with methyl alcohol.

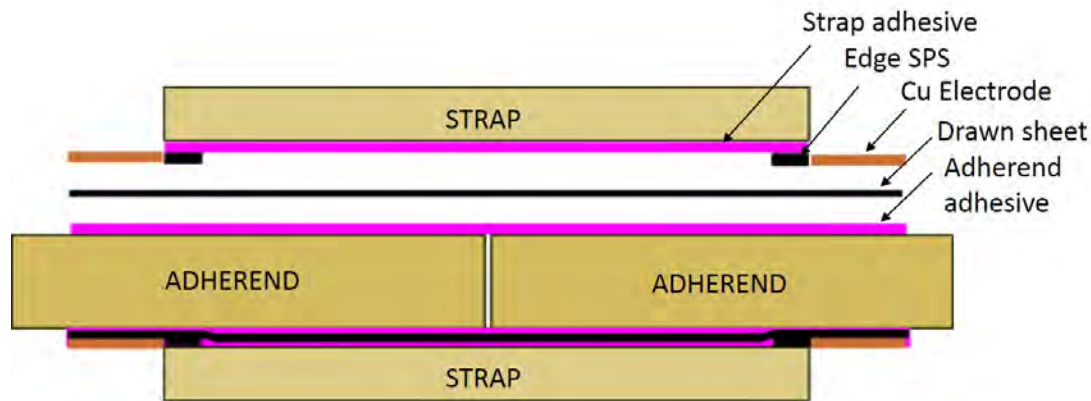


Figure 6.2. Cross section schematics of the bonded joint region with the edge SPS strips added with an exploded view on top.

Figures 6.1 and 6.2 depict the configurations of the double strap joints fabricated and tested. Thicknesses of each component are not to scale. In the figures, distinction is made for clarity between adhesive layer attached to the strap ("strap adhesive") and adhesive layer attached to the adherend ("adherend adhesive"). Another specimen with SPS embedded across entire bonded overlap region, in the same manner as shown in Figure 6.1, has been fabricated and tested. Inspection of that sample showed that dense CNT packing within the SPS did not allow for any significant penetration of the adhesive into the SPS. This resulted in a dramatic weakening of the joint as the test results showed.

The actual fabrication procedure for the "E" type sample is shown in Figure 6.3. This uses a custom fabricated aluminum jig that minimizes possible deviations between individual joint specimens. Initially, thin layers of adhesive paste were spread over the composite straps and overlap regions of the composite adherends. "Adherend adhesive" was spread slightly wider than the "strap adhesive" in order to allow for bonding to the copper electrodes. Once the straps and adherends were covered by adhesive paste, the first strap was placed in the jig with adhesive-covered side up and with copper electrodes placed at both edges of the strap on aluminum cross beams used to hold the joint in place. The DS was then pulled directly from the CNT array over the electrodes and strap, and stuck to the far side of the jig. The DS was held taught just above ( $\sim 1$  mm) the adhesive-covered surface of the strap. The adherend was then placed onto the DS as shown in Figure 6.3. This action had pressed the DS into the adhesive paste. At that point the DS was cut near to the CNT array, which was then set aside. After that the other adherend was added. Then the process was repeated in reverse order for the top half of the joint. First, the DS was pulled across the adhesive-covered surface of adherend, then the copper electrodes were

placed onto the DS and pressed in using the aluminum clamps that held the strap in place, and finally the top strap was added. Excess of DS material was wiped clean using ethanol after the joint has been cured.

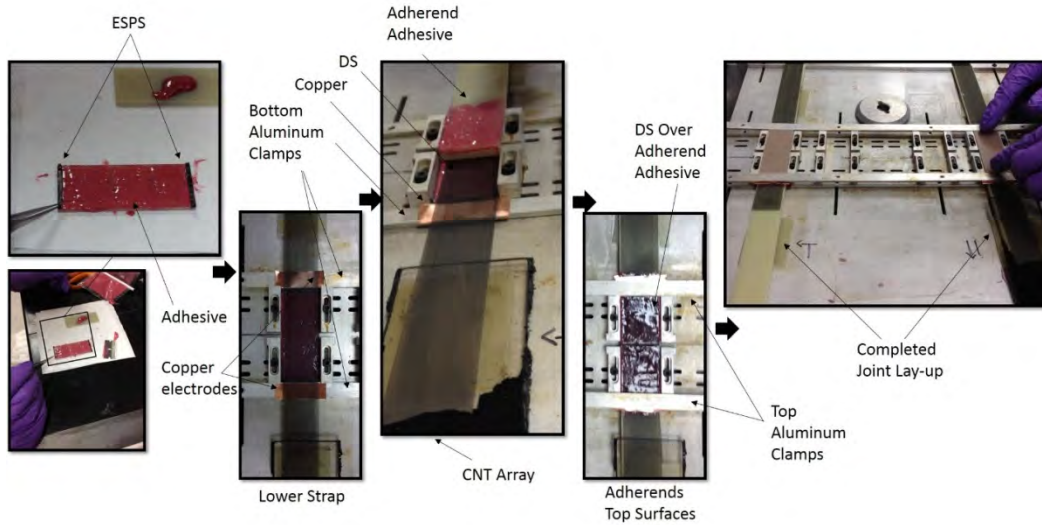


Figure 6.3. Step-by-step DSJ lay-up process, with CNT DS and edge SPS incorporated, using an aluminum jig.

Once the joint lay-up process was complete, a standard weight of 100 g was placed on the top of the upper strap to apply light pressure during curing. The assembly was then immediately placed in an oven and fully cured at 82°C for 60 min. Three commercial metal foil strain gauges were also mounted at different locations on both the adherend and strap surfaces, as shown in Figure 6.4, in order to monitor the strains in different locations during loading.

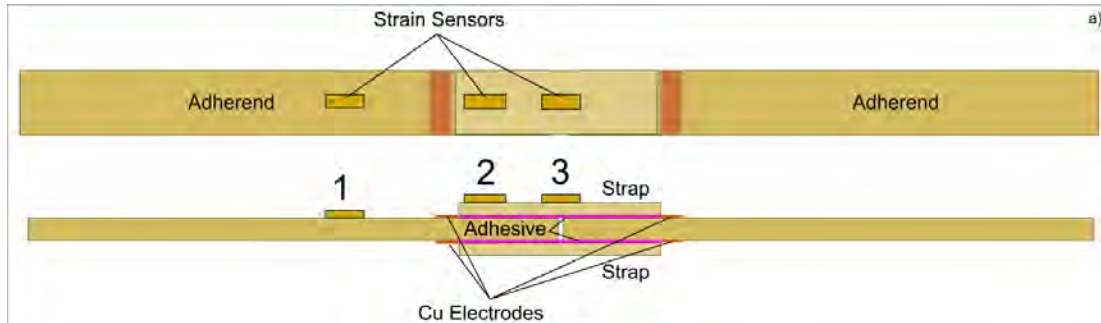


Figure 6.4. Schematics of DSJ and location of 3 strain sensors.

## 6.4. Joint Testing

In order to evaluate the electro-mechanical behavior of the fabricated DSJ samples, monotonic tensile tests were performed under in-plane loading in the joint length direction using a MTS Landmark servo hydraulic 250 kN test system. The load vs. grip displacement data were output directly from the MTS machine software. During the progress of the tests, the electrical

resistance variation of the specimen was simultaneously recorded with an Agilent 34420A multimeter at a frequency of 10 Hz. To obtain more accurate strain data in correspondence with the real time electrical resistance signals, the metal foil strain gauges were set to acquire strain responses at the same frequency. The resistance measurements were conducted using a two-probe method along the longitudinal direction of the composite joints. The tests were performed with a displacement-controlled loading rate of 1.5 mm/min. Three specimens per each joint group, “D” and “E”, were monotonically loaded to failure to ensure the repeatability of electro-mechanical behavior. The tests of group “S” specimens resulted in a very early joint failure which prevented the collection of a meaningful electro-mechanical behavior data. Group “B” specimens were only tested for mechanical performance due to the unmodified adhesive is non-conductive and yields no electro-mechanical data.

## 6.5. A Comparison of Joint Mechanical Performance With and Without CNT Sheets

To compare the mechanical performance of the joints, three specimens in each group of “B”, “D” and “E” were tested. Load vs. grip displacement curves of all nine specimens are presented in Figure 6.5a with the summary of a mean load and grip displacement data shown in Figure 6.5b. These results reveal that adding a DS to adhesive (e.g. “D” case) does not affect the load-to-failure value and only slightly reduces the displacement-to-failure value. Adding DS plus narrow SPS strips (e.g. “E” case) results in considerable increase of both the displacement-to-failure and load-to-failure values. The latter result is particularly important due to the following two reasons. First, because it removes the earlier concern raised by the mechanical test data for the “S”-type joint (not shown here), which failed at a much lower load level than the baseline joint “B”. Second, because it also shows that even poorly impregnated SPS can increase strength of the joint. The latter effect requires further thorough investigation, but at this point we believe it is owed to the CNT SPS reinforcing material being added in the zones of the highest peel strain concentration. In the context of this paper, these results justify the potential of using a combination of DS and narrow SPS strips for sensing strains in the zones of high strain concentration without sacrificing structural integrity and the joint strength.

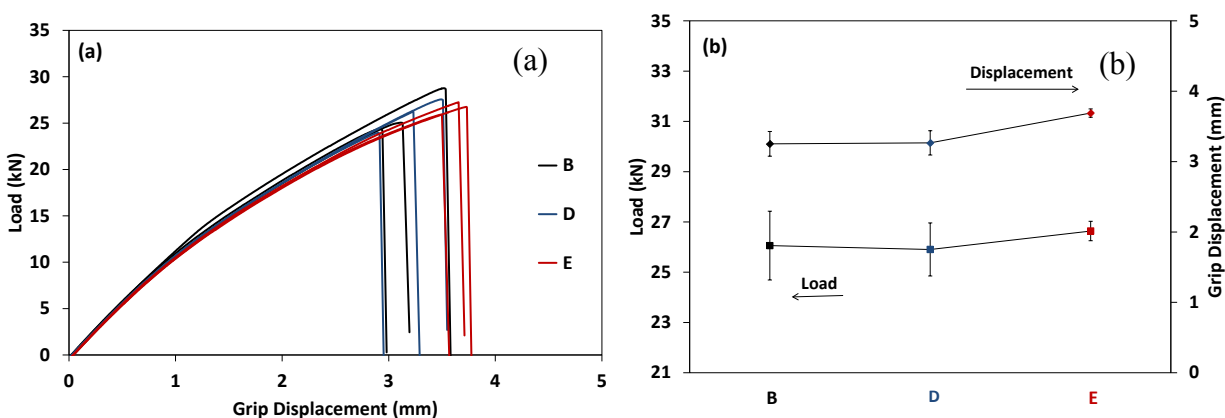


Figure 6.5. Typical load vs. displacement curves from MTS machine (a), and average peak load and displacement values at failure for “B”, “D” and “E” type joint specimens (b).



Some representative fracture surfaces of the “D” and “E” type joint specimens are shown in Figure 6.6. Similar failure modes are observed in both cases, and they are nearly identical to the ones observed in case “B”. Sufficient bonding was achieved by using the epoxy adhesive paste even with the DS added between the two adhesive layers. All of the joints exhibited a mixture of cohesive failure and quite unusual failure within the adherend by a surface ply delamination. One could have expected a consistent cohesive-type failure within adhesive layer if the CNTs had created significant defects at the mid-plane of the adhesive (where they were placed). However, we did not see this in the fracture surface images; this result confirms that the CNT DS was well integrated within the adhesive, and did not provide an easy path for the crack propagation. Therefore it did not weaken the joint.

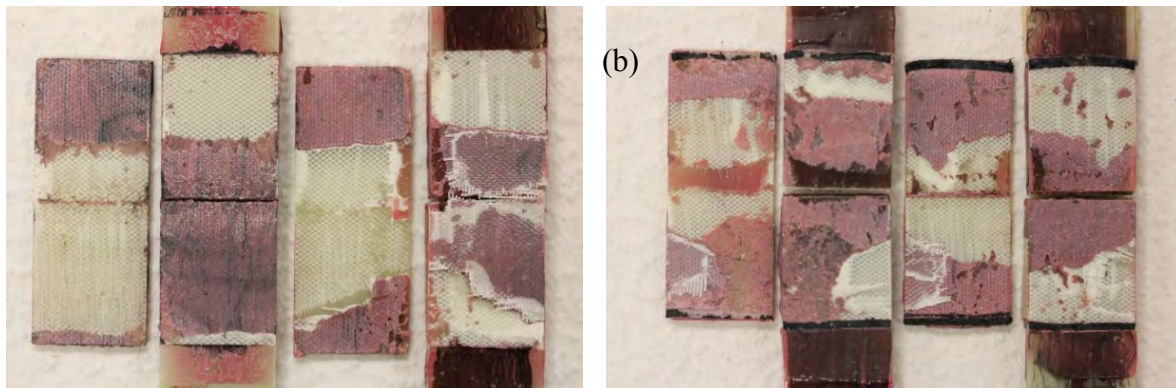


Figure 6.6. Fracture surfaces of “D” (a) and “E” (b) type joints specimens.

## 6.6. A Comparison of Electro-Mechanical Behavior

In order to evaluate the sensing capability of the CNT materials embedded in the tested DSJs, electrical resistance data were recorded and correlated to the real time strain data during the monotonic tensile tests. First, Figure 6.7 compares the resistance variation vs. longitudinal strain between a representative test coupon having a surface mounted DS and three “D” type joint specimens, all loaded to identical “nominal” strain levels (which were determined from respective grip displacement data using each specimen length). The composite sample with surface mounted DS sensor used the same fiberglass material as the adherand, the same Hysol adhesive and the DS processed from the same CNT array. Surface mounting with the use of identical conditions was important because it showed that the differences in electro-mechanical response for the two conditions were due to the placement of CNT sheets in the joint and not some other factors. While only one surface mounted sample was produced in this comparative study, it was observed that its electromechanical behavior was almost identical to that of the surface mounted samples studied in Chapter 5 and [17].

Many times higher resistance change was observed for the DS integrated within the joint than for the DS mounted on the surface. This is due to the fact that the joint geometry causes high localized concentration of the in-plane longitudinal strain near the overlap ends inside the joint, while there is no such longitudinal strain concentration in the flat tensile coupon case. Naturally, under identical nominal strain levels for the plain tensile coupon and for the joint (as is in the

case of Figure 6.7), local strain magnitudes within the joint overlap region reach much higher values. Accordingly, the “average” strain measured by the DS over entire overlap area should also be substantially higher than the nominal strain. Due to that, the cumulative electrical resistance change measured over entire overlap area should also be substantially higher than respective resistance change measured over the area covered by the DS on the plain coupon surface. This shows that the DS really works as a strain sensor – its electro-mechanical response depends on the location within the structure that experiences different strains in different locations. We hypothesize that the obtained DS resistance change data are mainly determined by the highest strain values within the overlap region (i.e., the values reached near the overlap ends). Yet, this hypothesis needs further validation by the use of appropriate theoretical models and also conducting further detailed experimental study.

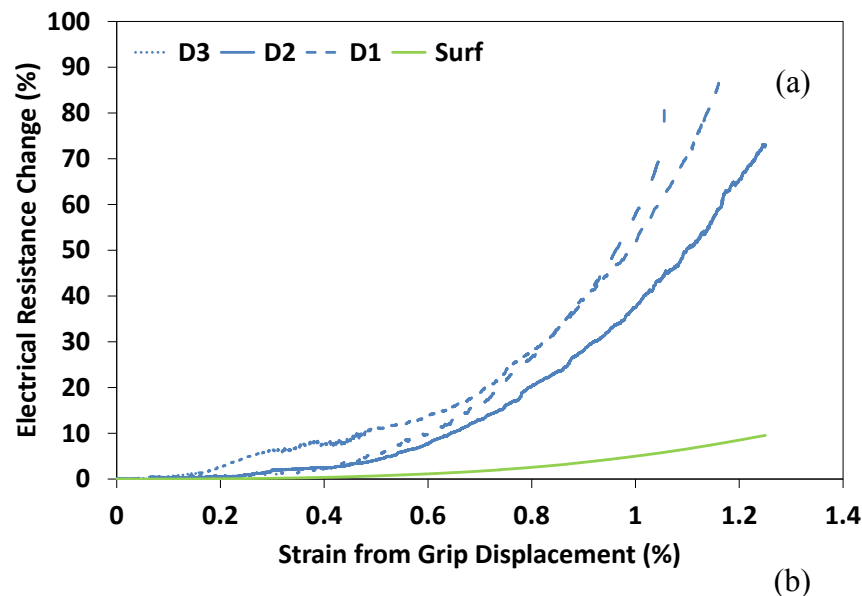


Figure 6.7. Electrical resistance vs. strain variations for a tensile coupon with surface mounted DS and for three specimens with analogous DS integrated in the DSJ samples.

Figure 6.8 shows the resistance variation vs. nominal strain curves plotted for the three “D” type and three “E” type joint specimens. Although the data scatter is rather large, the principal trend is clearly seen - the resistance change is consistently, several times, higher than in the case of “E” type specimens. This effect may be due to a combination of two main factors. First, it is possible that for the same nominal strain level (as plotted in Figure 6.8) the longitudinal strain over entire overlap area, as measured in both cases, is significantly different due to the addition of SPS end strips. One indirect indication of such a possibility is that, according to Figure 6.5b, the displacement-to-failure value in “E” case is higher. This effect can be interpreted in terms of the strain peaks near the overlap ends being reduced by the addition of CNT-reinforced SPS strips. Indeed, the joint failure initiation is delayed, and the grip displacement causing ultimate failure is increased accordingly. However, the difference between the displacement-to-failure values for the “E” and “D” cases seen in Figure 6.5b is not big, less than 20%; therefore, this factor makes probably only a minor contribution to what is seen in Figure 6.8.



The second factor is the difference between the sensing elements used in cases “D” and “E”. The “D” type joint has integrated very thin and generally uniform DS extending over entire overlap area which is essentially a 2D nanostructure. The “E” type joint has additional SPS strip at each end, but that strip is much thicker and more densely populated with the CNTs than respective DS. In fact, an SPS is more like a 3D nanostructure. As discussed earlier, the DS alone used in the “D” type joint is essentially a one-dimensional sensing element that responds primarily to the strain variation in its longitudinal direction, which is at the same time the joint loading direction. The DS-plus-SPS end strip sensing element used in the “E” type joint has much higher capability to also respond to the through-thickness strain variation. We assumed in the above considerations that the strain arising in the width direction of the joint is due to the Poisson’s effect; this is why that strain component is not only much smaller than the longitudinal strain but it does not have that high rise near the overlap ends which is characteristic for the peel strain. Hence, it is reasonable to attribute the difference between resistance change results in Figure 8 for the “D” and “E” cases mainly to the added high rise of peel strain detected by the SPS edge strips.

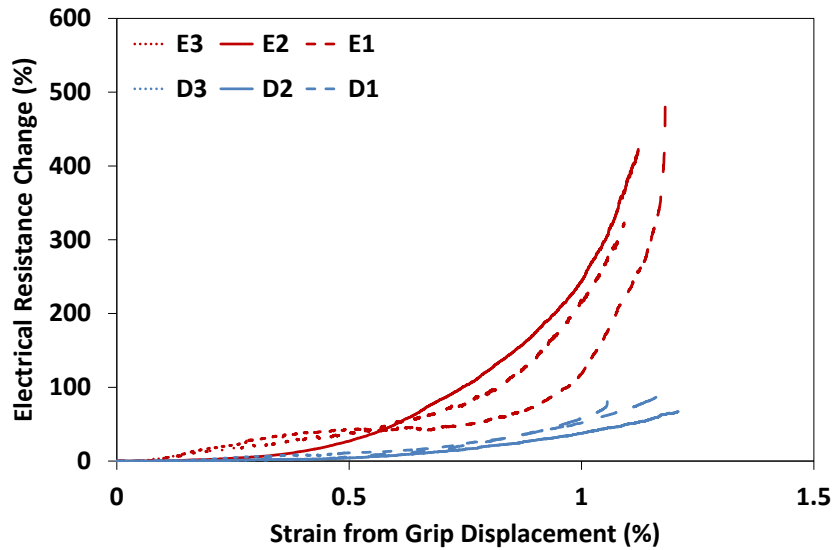


Figure 6.8. Electrical resistance change vs. grip displacement for “D” and “E” type joints.

## 6.7. Sensor Calibration and Strain Monitoring

Gauge factor (GF) is used to evaluate the sensor material sensitivity to strain. Its determination is straightforward in the case of one-dimensional uniform strain field, similarly to the case of conventional unidirectional strain gauges:

$$GF = (\Delta R/R_0)/\epsilon \quad (1)$$

where  $R_0$  is initial resistance,  $\Delta R$  is resistance change, and  $\epsilon$  is variable strain level. If  $\Delta R$  changes linearly with strain, it follows from Eq. (1) that GF is strain-independent and can be

treated as intrinsic sensor characteristic; this is not always applicable, of course, and is always limited to certain strain levels.

If the strain field is essentially multi-directional, the several unidirectional strain gauges, or a gauge rosette, have to be used. Further on, if the strain field is non-uniform, more than one unidirectional strain gauge or more than one gauge rosette have to be used at different locations of the structure. But even if same unidirectional strain gauges are used in such more complex situations, then each of them is still characterized by the same GF. For example, if a unidirectional strain gauge is embedded within adhesive joint overlap, it still has the same GF (assuming that the joint processing and environmental conditions do not affect its sensing characteristics, of course), but the strain to which the sensor is responding may be very different from the nominal strain determined from the end grip displacement or from the strains measured on the surfaces of the adherends.

If we invert Eq. (1), the following is obtained:

$$\varepsilon = (\Delta R/R_0)/GF \quad (2)$$

where GF is the same gauge factor characterizing given sensor,  $R_0$  is the measured “initial” resistance of the structure with no load applied and, accordingly, no strain generated, and  $\Delta R$  is the measured resistance change during loading. This simple equation would provide us with the sought strain monitoring result by continuously measuring electrical resistance change at some location within the structure during loading.

What needs to be done after that is determining the GF for a given sensor; that is commonly called the sensor calibration procedure. To accomplish this task in a conventional way, some already calibrated unidirectional sensor, such as a strain gauge, has to be exposed to exactly same strain level as the sensor with unknown GF. Then, the measured strain value has to be substituted into Eq. (1), together with the already measured  $R_0$  and  $\Delta R$  values, and the GF for a novel sensor would be determined. Accordingly with this scheme, the next step of the CNT DS sensor study should be a calibration. The simplest procedure has to follow the steps: (1) mount a strain gauge on one face of the tensile test coupon and the CNT SPS on the opposite face; (2) measure the initial resistance; (3) load the specimen and measure the strain variation by the strain gauge and, simultaneously, the resistance change by the CNT SPS. The results of such experiment should then be substituted into Eq. (1), and the GF would be determined.

After the above described task is accomplished, the now known GF is substituted into Eq. (2) together with the measured  $R_0$  and the  $\Delta R$  variation results, and the strain monitoring procedure for the joint is completed. This will probably work well in the case of using CNT DS sensor only (case “D”) because, as explained earlier in the chapter, a DS is essentially a unidirectional sensor. The case “E” is much more complicated because, as the results in Figure 8 show, that sensor type is not a unidirectional one, and the GF obtained for a CNT DS would not be applicable. Accordingly, even having the measured  $\Delta R$  values, Eq. (2) cannot be applied for an in-situ strain monitoring within the joint.

The above considerations are rather trivial of course, yet we see them instructional for developing the future practical procedures of continuous strain monitoring as applied to composite bonded joints with the use of different CNT sheet sensors. As specific results presented in this chapter reveal, the studied sensor materials possess excellent strain sensing capabilities, are easy to handle and embed and, also importantly, they do not make any negative effect on the joint strength.

## 6.8. Conclusions

Two methods of sensing adhesive joints and monitoring of the strains generated within adhesive layer are presented with the use of embedded CNT sheets and measuring their electrical resistance change under loading. These CNT materials show sufficiently sensitive to the high internal strains generated within adhesive layer of the joint; it is not easy to monitor those strains by other known sensing methods. The CNT sheets integrate well with the joint and do not affect negatively its strength, contrary to what is commonly observed with many other sensors.

Furthermore, a unique novel combination of an essentially two-dimensional CNT DS and an essentially three-dimensional CNT SPS is introduced. The latter material was integrated at the overlap ends only in the form of narrow strips and it shows many times higher electrical resistance change than the DS only under equivalent nominal strain level. This is attributed to the added capability of sensing the transverse peel strain, which has much higher values compared to the longitudinal in-plane strain near the overlap ends. The transverse peel strain is especially difficult to monitor in composite bonded joints, and a novel sensing method presented here offers new opportunities in this direction.

As experimental results presented of this chapter show, the studied novel CNT sensor materials possess excellent strain sensing capabilities, are easy to handle and embed. In order to complete their practicality studies, their calibration procedure has to be performed in the next step, and their gauge factors have to be determined accordingly.

## 6.9. References

1. Lim, A. S.; Melrose, Z. R.; Thostenson, E. T.; Chou, T.-W. Damage Sensing of Adhesively-Bonded Hybrid Composite/Steel Joints Using Carbon Nanotubes. *Compos. Sci. Technol.* 2011, **71**, 1183–1189.
2. Khan, S. U.; Kim, J. K. Improved Interlaminar Shear Properties of Multiscale Carbon Fiber Composites With Bucky Paper Interleaves Made From Carbon Nanofibers. *Carbon N. Y.* 2012, **50**, 5265–5277.
3. Abot, J. L.; Song, Y.; Vatsavaya, M. S.; Medikonda, S.; Kier, Z.; Jayasinghe, C.; Rooy, N.; Shanov, V. N.; Schulz, M. J. Delamination Detection With Carbon Nanotube Thread in Self-Sensing Composite Materials. *Compos. Sci. Technol.* 2010, **70**, 1113–1119.
4. Li, C.; Thostenson, E. T.; Chou, T.-W. Sensors and Actuators Based on Carbon Nanotubes and Their Composites: A Review. *Compos. Sci. Technol.* 2008, **68**, 1227–1249.
5. Fan, Z.; Santare, M. H.; Advani, S. G. Interlaminar Shear Strength of Glass Fiber Reinforced Composites. *Compos. Part A Appl. Sci. Manuf.* 2008, **39**, 543–554.

6. Hsiao, K.; Alms, J.; Advani, S. G. Use of Epoxy / Multiwalled Carbon Nanotubes as Adhesives to Join Graphite. *Nanotechnology* 2003, **14**, 791–793.
7. Meguid, S.; Sun, Y. On the Tensile and Shear Strength of Nano-Reinforced Composite Interfaces. *Mater. Des.* 2004, **25**, 289–296.
8. Vietri, U.; Guadagno, L.; Raimondo, M.; Vertuccio, L.; Lafdi, K. Nanofilled Epoxy Adhesive for Structural Aeronautic Materials. *Compos. Part B Eng.* 2014, **61**, 73–83.
9. Xu, L. R.; Li, L.; Lukehart, C. M.; Kuai, H. Mechanical Characterization of Nanofiber-Reinforced Composite Adhesives. *J. Nanosci. Nanotechnol.* 2007, **7**, 2546–2548.
10. Prolongo, S. G.; Gude, M. R.; Ureña, a. Rheological Behaviour of Nanoreinforced Epoxy Adhesives of Low Electrical Resistivity for Joining Carbon Fiber/Epoxy Laminates. *J. Adhes. Sci. Technol.* 2010, **24**, 1097–1112.
11. Mactabi, R.; Rosca, I. D.; Hoa, S. V. Monitoring the Integrity of Adhesive Joints During Fatigue Loading Using Carbon Nanotubes. *Compos. Sci. Technol.* 2013, **78**, 1–9.
12. Jakubinek, M. B.; Ashrafi, B.; Zhang, Y.; Martinez-Rubi, Y.; Kingston, C. T.; Johnston, A.; Simard, B. Single-Walled Carbon Nanotube–Epoxy Composites for Structural and Conductive Aerospace Adhesives. *Compos. Part B Eng.* 2015, **69**, 87–93.
13. Kang, M. H.; Choi, J. H.; Kweon, J. H. Fatigue Life Evaluation and Crack Detection of the Adhesive Joint With Carbon Nanotubes. *Compos. Struct.* 2014, **108**, 417–422.
14. Liu, Y.; Rajadas, A.; Chattopadhyay, A. A Biomimetic Structural Health Monitoring Approach Using Carbon Nanotubes. *Jom* 2012, **64**, 802–807.
15. Bradford, P. D.; Wang, X.; Zhao, H.; Maria, J.-P.; Jia, Q.; Zhu, Y. T. A Novel Approach to Fabricate High Volume Fraction Nanocomposites With Long Aligned Carbon Nanotubes. *Compos. Sci. Technol.* 2010, **70**, 1980–1985.
16. Yildiz, O.; Bradford, P. D. Aligned Carbon Nanotube Sheet High Efficiency Particulate Air Filters. *Carbon N. Y.* 2013, **64**, 295–304.
17. Li, A.; Bogdanovich, A. E.; Bradford, P. D. Aligned Carbon Nanotube Sheet Piezoresistive Strain Sensors. *Smart Mater. Struct.* 2015, **24**, 095004.
18. Bogdanovich, A. E.; Wigent, D. E. III; Whitney, T. J. Fabrication of 3-D Woven Preforms and Composites With Integrated Fiber Optic Sensors. *SAMPE J.* 2003, **39**, July-August, 6-15.
19. Wigent, D. E. III; Bogdanovich, A. E.; Whitney, T. J. Strain Monitoring of 3-D Woven Composites Using Integrated Bragg Grating Sensor Arrays. *CD Proc. of 49<sup>th</sup> Int. SAMPE Symp. and Exhibition*, May 16-20, 2004, Long Beach, CA.

1.

**1. Report Type**

Final Report

**Primary Contact E-mail****Contact email if there is a problem with the report.**

aebogdan@ncsu.edu

**Primary Contact Phone Number****Contact phone number if there is a problem with the report**

9195156566

**Organization / Institution name**

NC State University

**Grant/Contract Title****The full title of the funded effort.**

Multifunctional Shear Pressed CNT Sheets for Strain Sensing and Composite Joint Toughening

**Grant/Contract Number****AFOSR assigned control number. It must begin with "FA9550" or "F49620" or "FA2386".**

FA9550-12-1-0170

**Principal Investigator Name****The full name of the principal investigator on the grant or contract.**

Alexander Bogdanovich

**Program Manager****The AFOSR Program Manager currently assigned to the award**

Byung-Lip Lee

**Reporting Period Start Date**

04/01/2012

**Reporting Period End Date**

06/30/2015

**Abstract**

This research program investigated critical fabrication aspects, mechanical and electrical properties, and potential applications of a novel carbon nanotube material, named shear-pressed sheet. This material is fabricated from the chemical vapor deposition grown, tall aligned carbon nanotube arrays, with the use of automated shear-pressing device. It was shown that such sheets, having typically 50-200 micron thickness, are self-sustained and sufficiently stiff to be removed from the substrate, handled without the shape distortion and then used either in a dry form or as a resin-infused prepreg for interleaving laminated composites and their bonded joints. Extensive set of double-cantilever beam tests of composite laminates with integrated shear-pressed sheets showed substantial, up to two times, improvement in the Mode I interlaminar fracture toughness. Experimental single-lap and double-lap joints of composites with integrated shear-pressed sheet interleaves were manufactured and experimentally evaluated. Embedded carbon nanotube shear-pressed sheets and the added carbon nanotube drawn sheets showed excellent electrical resistance sensitivity and thus a potential for being used as in-situ strain and damage monitoring networks and devices which are practically non-intrusive and may simultaneously provide significant fracture toughness enhancements.

**Distribution Statement****This is block 12 on the SF298 form.**

DISTRIBUTION A: Distribution approved for public release.

Distribution A - Approved for Public Release

### Explanation for Distribution Statement

If this is not approved for public release, please provide a short explanation. E.g., contains proprietary information.

### SF298 Form

Please attach your [SF298](#) form. A blank SF298 can be found [here](#). Please do not password protect or secure the PDF. The maximum file size for an SF298 is 50MB.

[SF298\\_NCSU Bogdanovich Report Documentation Page.pdf](#)

**Upload the Report Document. File must be a PDF. Please do not password protect or secure the PDF. The maximum file size for the Report Document is 50MB.**

[NCSU Bogdanovich Final Report.pdf](#)

**Upload a Report Document, if any. The maximum file size for the Report Document is 50MB.**

### Archival Publications (published) during reporting period:

Ang Li, Alexander E. Bogdanovich and Philip D. Bradford, "Aligned carbon nanotube sheet piezoresistive strain sensors". Smart Materials and Structures, 2015, Vol. 24, 095004, 10 pp.; doi:10.1088/0964-1726/24/9/095004.

### Changes in research objectives (if any):

None.

### Change in AFOSR Program Manager, if any:

None.

### Extensions granted or milestones slipped, if any:

Extension granted from 04/01/2015 to 06/30/2015.

### AFOSR LRIR Number

### LRIR Title

### Reporting Period

### Laboratory Task Manager

### Program Officer

### Research Objectives

### Technical Summary

### Funding Summary by Cost Category (by FY, \$K)

	Starting FY	FY+1	FY+2
Salary			
Equipment/Facilities			
Supplies			
Total			

### Report Document

### Report Document - Text Analysis

### Report Document - Text Analysis

### Appendix Documents

## 2. Thank You

### E-mail user

Sep 27, 2015 16:38:47 Success: Email Sent to: aebogdan@ncsu.edu

DISTRIBUTION A: Distribution approved for public release.